

NOVEL MIXED METAL FERRITES FOR HYDROGEN PRODUCTION USING CHEMICAL
LOOPING

by

VICTORIA J. ASTON

B.S., New Mexico Institute of Mining and Technology, 2007

M.S., University of Colorado at Boulder, 2010

A thesis submitted to the

Faculty of the Graduate School of the

University of Colorado in partial fulfillment

of the requirement for the degree of

Doctor of Philosophy

Department of Chemical and Biological Engineering

2013

This thesis entitled:

Novel Mixed Metal Ferrites for Hydrogen Production Using Chemical Looping

written by Victoria J Aston

has been approved for the Department of Chemical and Biological Engineering

Alan Weimer (Chair)

Will Medlin

Date_____

The final copy of this thesis has been examined by the signatories, and we find that both the content and the form meet acceptable presentation standards of scholarly work in the above mentioned discipline.

Aston, Victoria J. (Ph.D., Chemical and Biological Engineering)

Novel Mixed Metal Ferrites for Hydrogen Production Using Chemical Looping

Thesis directed by Prof. Alan W. Weimer

The chemical looping hydrogen (CLH) process generates pure, separate streams of H₂ and CO₂ from synthesis gas without the use of expensive gas separation equipment. This technology is a potentially efficient method for future H₂ production from coal or biomass with integrated CO₂ capture. In the CLH process, a metal oxide material is reduced through contact with syngas at temperatures between 673 K and 1273 K, fully oxidizing the CO and H₂ in the syngas to H₂O and CO₂. The reduced metal oxide is then contacted with steam to regenerate the metal oxide and produce H₂. The mixed metal ferrites CoFe₂O₄ and NiFe₂O₄ are proposed as alternative metal oxides to the currently used Fe₂O₃. Thermodynamic analysis with the software package FactSageTM predicts high conversions of H₂ and CO to H₂ and CO₂ during the CLH reduction step and complete ferrite regeneration during the H₂O oxidation step. Laboratory experiments with mixed metal ferrites deposited on high surface area ZrO₂ support structures indicate cyclability under CLH conditions, and post-cycling analysis shows complete regeneration of the mixed metal spinel with no detected metal oxide-support interactions. In a packed bed reactor, CoFe₂O₄ and NiFe₂O₄ show superior performance to Fe₂O₃, with over 99% conversion of CO and H₂ to CO₂ and H₂O during reduction. Over 90% of the H₂/CO used to reduce the mixed metal ferrites was recovered as H₂ during H₂O oxidation. For Fe₂O₃, the recovery was only 20%. A kinetic analysis of the oxidation step indicated a dual oxidation mechanism for mixed metal ferrites that involved an order of reaction model followed by a diffusion limited model at higher conversions. Diffusion limitations are attributed to the effect of incorporation of Co²⁺ and Ni²⁺ cations into the spinel lattice. The reduction reaction in a

packed bed reactor is found to follow gas-solid equilibrium conversion values closely at low solid conversions. Analysis of the CLH system using an equilibrium limited model indicates these materials offer significant advantages in H₂ output over Fe₂O₃ at lower reaction temperatures and with high CO₂/CO and H₂O/H₂ syngas.

Table of Contents

Chapter 1: Introduction and Scope.....	1
1.1 Current and Future Hydrogen Consumption.....	1
1.2 Hydrogen Production Technologies.....	2
1.3 Hydrogen from Gasification	3
1.4 CO ₂ Sequestration	5
1.5 Chemical Looping for H ₂ /energy Generation with Integrated CO ₂ capture	6
1.6 Project Scope	6
1.7 References.....	9
Chapter 2: Literature Review.....	11
2.1 Chemical Looping Hydrogen (CLH) Process.....	11
2.2 Material Cyclability	13
2.3 Reaction Thermodynamics	15
2.4 Fe-based CLH System	17
2.5 CLH Reactor Design.....	19
2.6 Alternative CLH Metal Oxides.....	20
2.7 References.....	22
Chapter 3: Substrate Selection and Materials Analysis.....	27
3.1 Abstract.....	27
3.2 Introduction.....	27
3.3 Materials and Methods.....	28
3.3.1 Samples	28
3.3.2 Sample Characterization	29
3.3.3 Sample Cyclability.....	29
3.4 Experimental Results and Analysis.....	31
3.4.1 Sample Characterization	31
3.4.2 Phase Identification.....	32
3.3.3. Interaction with ZrO ₂	36
3.4.4 Material Cyclability	37
3.4.5 Characterization of Cycled Materials.....	40
3.3.6 Effect of H ₂ O Concentration and Temperature on Oxidation.....	41

3.4 Conclusions.....	42
3.5 References.....	43
Chapter 4: Novel Mixed Metal Ferrites for H₂ Production through Chemical Looping.....	46
4.1 Abstract.....	46
4.2 Introduction.....	47
4.3 Materials and Experimental Methods	51
4.3.1 Thermodynamic Analysis	51
4.3.2 Ferrite Sample Preparation.....	52
4.3.3 Material Characterization.....	53
4.3.4 Chemical Cycling.....	53
4.3.5 Gas Analysis	55
4.4 Results and Discussion	56
4.4.1 Thermodynamic modeling	56
4.4.2 Material Characterization.....	59
4.4.3 Reduction Step.....	60
4.4.4 XRD and Raman Analysis	63
4.4.5 Oxidation Step	68
4.4.6 Cyclability.....	71
4.4.7 Effect of Metal Oxide Choice on H ₂ Recovery	72
4.5 Conclusions.....	75
4.6 Acknowledgements.....	75
4.7 References.....	76
Chapter 5: Investigation of the H₂O Oxidation Kinetics of Reduced Fe₃O₄, CoFe₂O₄ and NiFe₂O₄ in a Stagnation Flow Reactor.....	80
5.1. Abstract.....	80
5.2. Introduction.....	80
5.3. Materials and Methods.....	82
5.3.1. Sample Preparation	82
5.3.2 Material Characterization.....	83
5.3.3. Kinetic Analysis in Stagnation Flow Reactor	84
5.3.4. Method of Kinetic Analysis	86
5.3.4.1 Mathematical Model of Reactor	86
5.3.4.2. Determination of τ and t_{shift}	90

5.4 Results and Discussion	91
5.4.1 Material Characterization.....	91
5.4.2 Material Cyclability	91
5.4.3 Kinetic Analysis.....	92
5.5 Conclusions.....	101
5.6 Acknowledgements.....	102
5.7 References.....	102
Chapter 6: A Thermodynamic Investigation of the Chemical Looping Hydrogen Process: Comparison of Novel Mixed Metal Oxides.....	105
6.1 Abstract.....	105
6.2 Introduction.....	105
6.3. Materials and Methods.....	110
6.3.1. Mathematical Model of the Chemical Looping Hydrogen Process	110
6.3.2 FactSage Calculations	112
6.3.2.1 Fe-O system	114
6.3.2.2 Fe-Co-O and Fe-Ni-O systems	117
6.3.3 Model Development.....	120
6.4 Sample Preparation and Reactor for Experimental Validation.....	122
6.4.1 Sample Preparation	122
6.4.2 Packed Bed Reactor	123
6.4.2 Gas Composition and Analysis.....	124
6.5 Results and Discussion	124
6.5.2. Model Results and Analysis.....	129
6.5.2.1. Solid Conversion.....	129
6.5.2.2. Complete Steam Oxidations.....	134
6.5.2.3. Hybrid steam/O ₂ Oxidations	136
6.6 Conclusions.....	140
6.7 References.....	141
Chapter 7: Conclusions and Future Work.....	143
7.1 Conclusions.....	143
7.2 Future Work.....	145
7.3 References.....	146
Bibliography	148

Appendix A: Diffusion in Metals and Spinel	160
A.1 Diffusion in metal and spinel lattices	160
A.2 Diffusion in Fe, Co and Ni Metals	161
A.3. Diffusion in Spinel	162
A.4 Diffusion Studies by Atomistic Computer Simulations	164
A.5 Computational Details	165
A.6. Calculation Results	166
A.7 References	169

List of Tables

Table 1.1: Current H ₂ production methods, adapted from Stiegel, <i>et.al.</i> , International Journal of Hydrogen Energy, 2006; 65 (Ref. [1]).	2
Table 1.2: Gaseous impurities in CO ₂ , and the concentration limits for sequestration. Adapted from Visser <i>et.al.</i> Greenhouse Gas Control; 2:478 (Ref. [12]).	6
Table 2.1: Equilibrium constants and H ₂ to H ₂ O conversion at 600°C for common chemical looping candidate metal oxides. [6, 7, 24]	16
Table 3.1: Sample mass percents and surface areas.	31
Table 3.2: Raman peaks for materials of interest.	34
Table 3.3: Comparison between initial sample surface area and ample surface area after cycling	40
Table 4.1: Compounds, gases and solution species considered in thermodynamic calculations using FactSage.	52
Table 4.2: Chemical equations for spinel reduction as predicted with FactSage. Mixed metal spinels (Eq.4.8, 9) reduce to form a Fe-rich spinel and ultimately a metallic phase. Each spinel composition is in equilibrium with a unique gas composition.	59
Table 5.1: Experimental rate-limiting mechanisms and activations energies for Fe oxidation.	82
Table 5.2: Common f(α) terms that express how the rate of reaction changes with reaction extent.	87
Table 5.3: Equations used in modeling the oxidation kinetics.	90
Table 5.4: Mass % metal oxide, cation ratio, and surface areas of ALD materials used in the kinetic study.	91
Table 5.5: Models and activation energies determined experimentally for the oxidation of Fe ₂ O ₃ CoFe ₂ O ₄ , and NiFe ₂ O ₄ materials.	96
Table 6.1: List of key assumptions made in development of MATLAB model	112
Table 6.2: Moles of H ₂ produced per mole of H ₂ O fed to the reactor and the HHV value of the H ₂ produced in comparison to the energy needed to generate steam for full H ₂ O oxidation of materials for reduction conditions and temperatures.	128
Table A.1: Defect migration and formation enthalpies found in the literature	155
Table A.2: Lattice structures and vacancy formation in metals	158
Table A.3: Migration enthalpies in metals calculated in this study and from literature	158
Table A.4: Migration barriers for octahedral-octahedral migration in Fe ₃ O ₄ , CoFe ₂ O ₄ and NiFe ₂ O ₄ .	159

List of Figures

Figure 2.1: Schematic for the ideal chemical looping H ₂ production process.	12
Figure 2.2: Reduction and oxidation cycles of bulk commercially available Fe ₂ O ₃ show systematic degradation over time, from Gupta <i>et al.</i> Energy & Fuels; 2007;21:2900 (Ref. [7]).....	14
Figure 2.3: The equilibrium phase diagram for the Fe-,FeO-, Fe ₃ O ₄ -,Fe ₂ O ₃ system with CO/CO ₂ (--) and H ₂ /H ₂ O (- -). The lines are the equilibrium constants at each temperature, and indicate the gas composition at which the phase transition will occur from Gupta <i>et al.</i> Energy & Fuels; 2007;21:2900 (Ref. [7])	18
Figure 2.4: The current state-of-the-art CLH process includes an O ₂ oxidation step, in which a portion of possible H ₂ production is not utilized.	19
Figure 3.1: Stagnation flow reactor. Gases flow through the center tube and onto the sample at the bottom of the closed end tube. Dimensions are such to minimize velocity gradients across the sample, from Scheffe <i>et al.</i> Chemistry of Materials.2010;23 (Ref. [4])......	30
Figure 3.2: (a) NiFe ₂ O ₄ deposited on ZrO ₂ (10X) (b) SEM image of NiFe ₂ O ₄ particle surface (c) TEM image of ZrO ₂ blank shows ~20 nm sintered particles (d) Annealed and crushed Fe ₂ O ₃ sample shows 100-200 nm metal oxide agglomerates.	32
Figure 3.3 Raman spectra of a) Fe ₃ O ₄ , b) NiFe ₂ O ₄ samples, and c) CoFe ₂ O ₄ . d) Position of each peak for comparison with Table 3.2.....	35
Figure 3.4: Raman spectra displaying m-ZrO ₂ signal. No peaks from c-ZrO ₂ are detected. The c-ZrO ₂ phase is expected in the event of cation diffusion into the substrate.	37
Figure 3.5: a) H ₂ production during H ₂ O oxidation of reduced Fe ₃ O ₄ sample. b) H ₂ production during H ₂ O oxidation cycles of reduced NiFe ₂ O ₄ . c) H ₂ production during H ₂ O oxidation cycles of reduced CoFe ₂ O ₄ . d) Comparison of Fe ₂ O ₃ , NiFe ₂ O ₄ , and CoFe ₂ O ₄ samples.....	39
Figure 3.6: Effect of H ₂ O concentration and temperature on the H ₂ production of CoFe ₂ O ₄ materials. ...	42
Figure 4.1: Reactor system used for chemical reduction and H ₂ O oxidation.	55
Figure 4.2: FactSage modeling results for the a) NiFe ₂ O ₄ system and b) CoFe ₂ O ₄ system. The total moles of spinel, MeO, and metallic phases, as well as the fraction of each cation in the spinel phase are shown as a function of pH ₂ /pH ₂ O and pCO/pCO ₂	57
Figure 4.3: TEM of crushed and annealed incipient wetness prepared sample, surface areas and mass percents for each sample tested.....	60
Figure 4.4: Fifteen minute syngas reductions of a) Fe ₂ O ₃ , b) Fe ₃ O ₄ , c) NiFe ₂ O ₄ , and d) CoFe ₂ O ₄	62
Figure 4.5: XRD data for a) NiFe ₂ O ₄ and b) CoFe ₂ O ₄ samples. The spinel phase is regenerated during H ₂ O oxidation for each sample, and a metallic phase forms during reduction.	64
Figure 4.6: Raman spectra of fully oxidized CoFe ₂ O ₄ and a CoFe ₂ O ₄ sample reduced for three minutes. The peak shift to the left indicates a change in octahedral divalent cation from Co ²⁺ to Fe ²⁺	68

Figure 4.7: H ₂ production comparison for Fe-only, NiFe ₂ O ₄ and CoFe ₂ O ₄ samples after 12 minutes of reduction. Each material proved to be reactive with H ₂ O, and NiFe ₂ O ₄ and CoFe ₂ O ₄ produce significantly more H ₂ than the Fe-only material under these conditions.	70
Figure 4.8: Cyclability of the a) NiFe ₂ O ₄ and b) CoFe ₂ O ₄ samples. Each was cycled over 20 times with stable H ₂ production totals and peak rates.	72
Figure 4.9: Conversion efficiency of Fe-based materials (- -) and mixed metal ferrites (-), and experimental results from laboratory packed bed reactor. Mixed metal ferrites approach the theoretical value of 100% conversion efficiency, while Fe-based materials approach their theoretical maximum of 25% conversion efficiency.	74
Figure 5.1: Stagnation flow reactor. Gases flow through the center tube and onto the sample at the bottom of the closed-end tube. Dimensions are such to minimize velocity gradients across the sample. From <i>Scheffe et al. Chemistry of Materials</i> 2011;23:2030 (Ref. [13]).....	85
Figure 5.2: Each component of the system introduces dispersion, which affects the measured peak shape and kinetic model if not accounted for in analysis.....	88
Figure 5.3: Cyclability of CoFe ₂ O ₄ sample.....	92
Figure 5.4: Fe data and best-fit kinetic model.....	93
Figure 5.5: a) An order of reaction model fits the reaction peak, while a diffusion model fits the long-term H ₂ production b) A combination of two kinetic models gives the best fit for the NiFe ₂ O ₄ material.	94
Figure 5.6: CoFe ₂ O ₄ kinetic plots.	95
Figure 5.7: a) SEM image of uncycled sample b) SEM image of sample after 20 cycles. 1 μm agglomerates of metal oxide form during cycling.	98
Figure 6.1: Process schematic for the model operating with only H ₂ O oxidation.	111
Figure 6.2: Process schematic for the model operating with both H ₂ O and O ₂ oxidation.	111
Figure 6.3: Composition of solid in the Fe-O binary system as a function of temperature and pO ₂	115
Figure 6.4: Equilibrium for the Fe-CO-CO ₂ and Fe-H ₂ -H ₂ O system. From Muller <i>et al. Chemical Engineering Journal</i> ; 2011:166 [17]	116
Figure 6.5: Phases present for the Fe-Co-O system under varying pO ₂	118
Figure 6.6: Model predictions for gas and solid conversions in the packed bed in comparison to FactSage predictions.....	127
Figure 6.7: Model H ₂ predictions and H ₂ production from laboratory packed bed reactor experiments. .	129
Figure 6.8: Conversion of solid materials at syngas breakthrough at 873 K for each metal oxide type under two different syngas compositions. X values are material conversion and R-values are the ratio of moles of solid in the bed to moles of syngas through the reactor at breakthrough.	131
Figure 6.9: Conversion of solid materials at breakthrough for each metal oxide type at 1073 K under different syngas compositions and temperatures. X values are material conversion and R values are the ratio of moles of solid in the bed to moles of syngas through the reactor at breakthrough.	133

Figure 6.10: CLH efficiency vs. the conversion efficiency of the materials at 873 K and 1073 K after reduction with two different syngas compositions 138

Chapter 1: Introduction and Scope

1.1 Current and Future Hydrogen Consumption

Hydrogen, the most abundant element in the universe, makes up about 18% of the atoms in our environment. Present mostly in compounds such as water and hydrocarbons, rather than as gaseous hydrogen (H_2), H_2 must be extracted and separated from other elements. [1] Currently, H_2 production technology is a mature field, and over 20 million tons of H_2 are generated per year, with 9 million tons generated in the United States (U.S.). [1] Half of the current H_2 produced globally is used for ammonia production for the fertilizer industry, and the rest is used in petroleum refining, methanol production, metallurgical processing, and for scientific purposes. [1] Additionally, the “hydrogen economy” has been proposed since the 1970’s as a solution to our nation’s fuel-related environmental and energy security problems. [2] Fuel cells utilizing H_2 are shown to be up to three times more efficient than an internal combustion engine for transportation, producing only H_2O as a product. [3] Hydrogen is hailed as an attractive replacement for gasoline, diesel, natural gas, and other fossil-based fuels that are finite in nature, volatile in price, and leave the U.S. dependent on foreign sources. Over half of the crude oil consumed in the U.S. is imported, leaving the nation vulnerable to price fluctuations resulting from decreased oil production or increased oil demand in other countries. [4, 5]

Shifting to a hydrogen economy for transportation and electricity generation would result in an increase in U.S hydrogen consumption of over 40 million tons per year. [1] Regardless of implementation of a hydrogen economy, the need for fertilizer and petroleum refining will result in a continued increase in the use of H_2 in future years. The expected world population increase of nearly three billion people by 2050 will significantly increase world food and energy

requirements. [6] The 2007 International Energy Outlook predicts a 250 quadrillion BTU increase in world energy demand between 2004 and 2030. [4]

1.2 Hydrogen Production Technologies

Current H₂ production technologies include steam-methane reforming and partial oxidation of hydrocarbons, and to a much lesser extent, gasification, pyrolysis and electrolysis.

These methods are summarized in Table 1.1. [1]

Method	Overall Efficiency (%)	H ₂ cost (US\$/GJ) (2006)	Total Capital Investment (US\$/GJ H ₂ capacity)	Pros	Cons
Steam Reforming	65-75 (LHV)	5-8	9-15	Well-established	Extensive infrastructure
Partial Oxidation	50 (LHV)	7-10	9-22	Minimal infrastructure, well est., variety of fuels	
Gasification	42-47 (HHV)	9-13	20-42	Minimal infrastructure, CO ₂ for sequestration, uses a variety of cheap fuels, could use solar	
Pyrolysis	48 (HHV)	9-13	15-19	Minimal infrastructure, CO ₂ for sequestration, uses a variety of cheap fuels	
Electrolysis	35-42 (HHV) (electricity source included), 70 (NG assisted)	20-25 (large) 11-42 (small)	3-30 (large) 32-486 (small)	Potential zero emissions with renewable electricity	Benefits depend on electricity supply, water supply often unreliable

Table 1.1: Current H₂ production methods, adapted from Stiegel, *et al.*, International Journal of Hydrogen Energy, 2006; 65 (Ref. [1]).

Approximately 80% of the H₂ produced worldwide comes from natural gas or oil through the steam methane reforming and partial oxidation of hydrocarbon processes. As a result, the price of H₂ is highly dependent on the price of petroleum. Gasification of coal accounts for nearly all of the remaining H₂ production, and a small fraction is produced using water

electrolysis technology. [1] Of these technologies, only gasification, pyrolysis, and electrolysis can be applied to renewable fuels and are consequently attractive as long-term H₂ sources. Gasification systems produce electricity, H₂, or other hydrocarbon fuels while utilizing any of a variety of carbon based fuels, including coal, biomass and organic waste material. As the prices of natural gas and oil increase and petroleum supplies eventually become scarcer, coal is projected to become a major source of H₂, especially in countries with an abundance of coal. [7] The known coal reserves in the U.S. are projected to last over 250 years at the current consumption rate. [8] Similar to oil and natural gas, coal is a finite fossil resource; however, it may be vital to aid in the transition between fossil and renewable fuels. The technologies developed for generating fuels from coal will greatly benefit the next generation of fuels from gasification of biomass and waste, while providing the significant volume of fuels necessary to sustain current energy consumption.

1.3 Hydrogen from Gasification

Though not common in the United States, gasification is a well-established technology used in regions where oil and natural gas are expensive, such as China and South Africa. [7] The gasification process, like all other primary H₂ production technologies except electrolysis, generates an intermediate of synthesis gas. Synthesis gas (syngas) is a mixture of CO, CO₂, H₂, and H₂O formed as the organic molecules break apart at the high temperatures and pressures encountered in the gasification process. Coal has a lower H₂/C ratio than natural gas, meaning more CO₂ is generated for each mole of H₂ produced from coal than per mole of H₂ produced from steam methane reforming. [7] Syngas undergoes the water-gas shift reaction (Eq. 1.1) to shift the composition to be high in H₂ and CO₂.



The H₂ and CO₂ must then be separated using pressure swing adsorption (PSA), chemical scrubbing (Monoethanolamine or Selexol), or membrane technologies.

Pressure swing adsorption (PSA) has been a state-of-the art gas separations technology for over 30 years. During the PSA process, CO₂ is adsorbed on physical sorbents, such as silica gel or activated carbon, leaving a purified H₂ stream. [8] The sorbent is regenerated through bed depressurization, which allows the CO₂ and other impurities to desorb. De-pressurization and re-pressurization is highly energy intensive and the process only recovers 70-90% of the H₂ in the feed gas. The remaining H₂ is lost in the waste stream. [9] Membrane separation technologies are attractive due to their simplicity of operation, and are the subject of much current research. However, the full potential of membrane CO₂/H₂ separation has not yet been realized commercially. [10] Membrane separation results in recovery of between 70-99% of the H₂ in the gas, and often requires highly pressurized syngas and large surface areas for adequate H₂ purity. [11]

The route to H₂ from coal via gasification is inherently more expensive than H₂ production from natural gas due, in part, to the greater capital costs of the gasification reactor and gas cleaning technologies necessary to remove sulfur and other contaminants from coal-derived syngas. [10] Improvements in gasifier technology, gas cleaning technology, and H₂/CO₂ separation and sequestration technology will decrease the cost of H₂ from coal and make it competitive with current H₂ production methods and affordable for the U.S. consumer. A 60% efficiency for fuels production from coal gasification, with carbon capture, would make these technologies economical. [10]

1.4 CO₂ Sequestration

Carbon capture and storage (CCS) is the separation and capture of CO₂ produced at stationary sources, followed by transport and storage in geological reservoirs to prevent its release into the atmosphere. [11] The cost of CCS is high, but future carbon taxes and fees are proposed to provide incentive to curb the release of large amounts of CO₂ into the atmosphere.

Carbon dioxide prepared for sequestration does contain gaseous impurities that negatively affect the gas transport, injection and storage properties, and ultimately the cost of underground containment. Non-condensable species such as H₂ and N₂ decrease CO₂ storage capacity while increasing the energy required for injection and the volume necessary to store the CO₂. Due to the decreased storage capacity, a CO₂ stream with high impurity (> 15% non-condensable gasses) is estimated to increase the cost of CCS by up to 26%, with an average increase of 6%. [12] The current recommendations for CO₂ purity for CCS are shown in Table 1.2. [12] Conventional CO₂ removal processes are typically focused on the purity of the H₂ rather than the purity of the CO₂ and thus leave significant fractions of impurities in the CO₂. Future separations processes designed to generate CO₂ for sequestration must optimize the purity of the CO₂ in addition to the purity of the H₂.

Component	Concentration	Notes
CO ₂	> 95.5 vol%	
CO	2000 ppm	Safety factor of 5 applied due to toxicity, design and operation limit is higher
H ₂ S	200 ppm	Safety factor of 5 applied due to toxicity
CH ₄	< 4 vol%	Energy consumption during compression
H ₂ O	500 ppm	Below solubility of H ₂ O in CO ₂ to prevent corrosion
N ₂	< 4 vol%	Energy consumption during compression
Ar	< 4 vol%	Energy consumption during compression
H ₂	< 4 vol%	Energy content of H ₂ , Energy consumption during compression
SO _x	200 ppm	Prevent dissolution of rocks
NO _x	200 ppm	Prevent dissolution of rocks

Table 1.2: Gaseous impurities in CO₂, and the concentration limits for sequestration. Adapted from Visser *et al.* Greenhouse Gas Control; 2:478 (Ref. [12]).

1.5 Chemical Looping for H₂/energy Generation with Integrated CO₂ capture

Chemical looping H₂ production (also known as “syngas chemical looping”, or “chemical looping reforming”, and will be referred to as the CLH process for this thesis) produces H₂, electricity, or both from syngas using cyclic reduction and oxidation of metal oxides. [13-15] The main advantage of the CLH process over conventional water gas shift technologies is the production of pure and separate streams of H₂ and CO₂ from syngas with any composition without the use of complex separations technologies. The overall efficiency of this process is estimated to be 64% with 100% CO₂ capture. A maximum efficiency of 57% for conventional coal-to-hydrogen processes is calculated in the same study. [16]

1.6 Project Scope

Chemical looping hydrogen technology has the potential to bring the H₂ and energy production cost via gasification lower, thus increasing its competitiveness in the current H₂ market and aiding the transition from dependence on foreign fossil fuel to a native fuel supply, and ultimately a renewable fuel supply. The objective of this research is to investigate novel

materials that allow the CLH process to produce H_2 more efficiently with complete carbon capture. Specifically, the effect of doping conventional ferrite materials used in the CLH process with additional transition metal oxides will be investigated. These materials have the potential to increase the flexibility of the CLH process, allowing greater H_2 recovery at lower material conversions.

This thesis focuses primarily on the mixed metal ferrites $CoFe_2O_4$ and $NiFe_2O_4$, and their performance in the reduction and oxidation cycles of the CLH process. Due to the lack of demonstrated cyclability properties in the literature under these conditions, $NiFe_2O_4$ and $CoFe_2O_4$ were synthesized and tested in the laboratory to establish their suitability for the CLH process. Specifically, their ability to regenerate the mixed-metal spinel structure during H_2O oxidations was investigated. Samples were analyzed with Raman spectroscopy to determine the solid phases present, and interactions between the inert support and metal oxide material were investigated. Additionally, the cyclability of the metal oxides was established through quantifying the total H_2 production of each cycle.

Cyclability and reactivity with H_2O alone are not sufficient to make $NiFe_2O_4$ and $CoFe_2O_4$ candidates for the CLH process. An examination of thermodynamic equilibrium between the CO/CO_2 and H_2/H_2O systems with the mixed metal ferrites, combined with experimental results in a packed bed reactor, were used to show the benefits of the mixed metal oxides over conventional ferrite materials. Thermodynamic analyses were performed using the Gibbs Free Energy Minimization software package, FactSageTM, and its associated thermodynamic property databases. The reactions in the solid phase were investigated through material analysis with X-ray diffraction and Raman spectroscopy.

In order to understand the rate-limiting mechanisms of the slow reactions involving the mixed metal ferrites, a stagnation flow reactor at Sandia National Laboratories was used to investigate the kinetics of the H_2O oxidation of reduced ferrites. This instrument has many advantages over the packed bed reactor used in the previous step, as it allows one-dimensional homogeneous flow over the sample to sweep away product gasses that inhibit the material forward reaction. Data from this reactor were used to establish the fundamental mechanism controlling the rate of sample reaction, and to calculate the kinetic parameters necessary to model the oxidation reaction over the temperature range of material cyclability. A model that accounts for the dispersion and mixing in the reactor was used to calculate the kinetic parameters that describe the global minimum error, and thus the best fit to considering all the data points. An understanding of the fundamental oxidation mechanisms allows identification of techniques to enhance the reaction rate. Due to the lack of current literature regarding cation diffusion in spinels, the density functional theory (DFT) technique was used to investigate the difference in migration barriers between metallic Fe, Co and Ni, and the spinels Fe_3O_4 , CoFe_2O_4 , and NiFe_2O_4 .

Finally, a model of the system was developed to explore a hybrid $\text{H}_2\text{O}/\text{O}_2$ oxidation of the mixed metal spinels for the production of H_2 /heat, with the goal of optimizing the H_2 and energy output of the CLH process using CoFe_2O_4 and NiFe_2O_4 . This model, developed in MATLAB, compared the performance of the novel mixed metal materials with that of the conventional Fe_2O_3 CLH process. The effects of syngas composition and reaction temperature on the material reduction extent, and H_2 and heat generated during $\text{H}_2\text{O}/\text{O}_2$ oxidation were investigated.

1.7 References

- [1] Stiegel GJ, Ramezan M. Hydrogen from coal gasification: An economical pathway to a sustainable energy future. *International Journal of Coal Geology*. 2006;65:173-90.
- [2] Bockris JOM. The origin of ideas on a hydrogen economy and its solution to the decay of the environment. *International Journal of Hydrogen Energy*. 2002;27:731-40.
- [3] Elkins P, Hughes N. The prospects for a hydrogen economy (1): hydrogen futures. *Technology Analysis & Strategic Management*. 2009;21:781.
- [4] (EIA) EIA. *Annual Energy Outlook 2007*. Washington, D.C.: U.S. Department of Energy; 2007.
- [5] EIA. *Annual Energy Review 2008*. United States Department of Energy; 2008.
- [6] Division UNDoEaSAP. *World Population to 2300*. New York United Nations; 2004.
- [7] Shoko E, McLellan B, Dicks AL, Diniz da Costa JC. Hydrogen from coal: Production and utilisation technologies. *International Journal of Coal Geology*. 2006;65:213-22.
- [8] Fan L. *Chemical Looping Systems for Fossil Energy Conversion*. Hoboken, NJ: John Wiley & Sons, Inc.; 2010.
- [9] Sircar S, Golden TC. Purification of Hydrogen by Pressure Swing Adsorption. *Separation Science and Technology*. 2006;35:667-87.
- [10] Damen K, Troost Mv, Faaij A, Turkenburg W. A comparison of electricity and hydrogen production systems with CO₂ capture and storage. Part A: Review and selection of promising conversion and capture technologies. *Progress in Energy and Combustion Science*. 2006;32:215-45.
- [11] Inc. JEC. *Integration of H₂ Separation Membranes with CO₂ Capture and Compression*. National Energy Technology Laboratory; 2009.
- [12] Visser Ed, Hendriks C, Barrio M, Mølnvik MJ, Koeijer Gd, Liljemark S, et al. Dynamis CO₂ quality recommendations. *Greenhouse Gas Control*. 2008;2:478-84.

[13] Solunke R, Vesper G. Hydrogen Production via Chemical Looping Steam Reforming in a Periodically Operated Fixed-Bed Reactor. *Ind Eng Chem Res*. 2010;49:11037-44.

[14] Bohn CD, Muller CR, Cleeton JP, Hayhurst AN, Davidson JF, Scott SA, et al. Production of Very Pure Hydrogen with Simultaneous Capture of Carbon Dioxide using the Redox Reactions of Iron Oxides in Packed Beds. *Ind Eng Chem Res* 2008;47:7623-30.

[15] Gupta P, Velazquez-Vargas L, Fan L. Syngas Redox (SGR) Process to Produce Hydrogen from Coal Derived Syngas. *Energy Fuels*. 2007;21:2900-8.

[16] Fan L, Li F, Ramkumar S. Utilization of a chemical looping strategy in coal gasification processes. *Particuology*. 2008;6:131-42.

Chapter 2: Literature Review

2.1 Chemical Looping Hydrogen (CLH) Process

In addition to being a possible future energy source for electricity and vehicle transportation, H₂ is necessary for the ammonia production and oil refining industries, which nationally use nine million tons of H₂ every year. [1] Current methods of H₂ production, including steam methane reforming, partial oxidation of hydrocarbons and coal gasification, require the use of the water-gas shift reaction (Eq. 2.1) to produce a mixture of H₂ and CO₂ from the synthesis gas (syngas) that they generate.



The reaction in Eq. 2.1 is thermodynamically limited at high temperatures and kinetically limited at low temperatures. Consequently, a two-stage process is required to maximize the amount of H₂ in the syngas. Supplementary purification is then necessary to decrease the amount of CO in the gas stream to the desired level. [2, 3] Additionally, the CO₂ must be separated from the H₂ in the product stream using processes such as Pressure Swing Adsorption (PSA) or Monoethanolamine (MEA) scrubbing, which carry high energy penalties and results in the loss of up to 30% of the produced H₂. [4, 5] Future H₂ generation techniques will need to be capable of efficiently generating a relatively pure and easily-sequestered CO₂ waste stream as monetary penalties for the release of CO₂ take effect.

The Chemical Looping Hydrogen (CLH) production process is an effective alternative method for generation of pure H₂ from any syngas with integrated CO₂ capture. (Figure 2.1) [2, 6, 7] In the CLH process, syngas leaving a gasifier reduces a metal oxide material at moderate to high temperatures (773 K to 1273 K) (Eq. 2.2-3). The reduced metal oxide is then oxidized

using steam to produce H_2 , a process that regenerates the metal oxide to its original state. (Eq. 2.4).



By splitting the water-gas shift reaction into two separate steps, the CLH process takes advantage of fast kinetics at high temperatures without the associated thermodynamic limitations. [2] Furthermore, pure and separate H_2 and CO_2 are produced without complicated and expensive multistep separation processes.

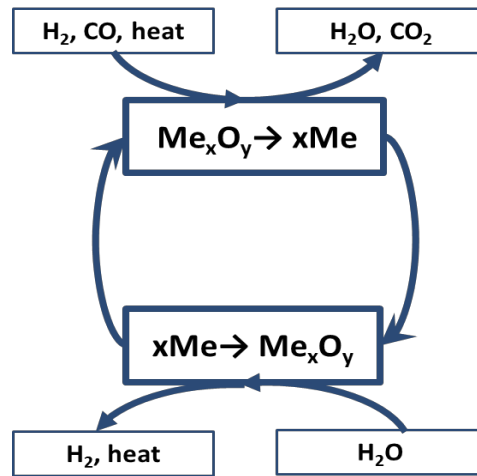


Figure 2.1: Schematic for the ideal chemical looping H_2 production process.

In order to be a viable material for the CLH process, a metal oxide must meet the following criteria: [7]

- 1) The material must demonstrate fast and stable kinetics over a large number of redox cycles.
- 2) The reduced form of the metal oxide must be readily oxidized using steam.

- 3) Thermodynamically, the reaction of the metal oxide with the syngas must be able to convert virtually all of the CO and H₂ in the syngas to CO₂ and H₂O.

2.2 Material Cyclability

Criterion 1, material cyclability and reactivity, is often a property of the material synthesis method and has been studied and demonstrated at length. Consistent cyclability results are difficult to obtain for any one method of sample synthesis, most likely due to differences in preparation method and treatment of the sample before cycling. [4] Commercially available powders categorically have been shown to degrade with cycling as a consequence of sintering of the oxide and subsequent surface area loss. [7-10] Data from bulk commercial Fe₂O₃ powder cycling in a thermogravimetric analyzer (TGA) are shown in Figure 2.2, demonstrating the diminished reduction and oxidation capacity of the material in each subsequent cycle. [7] Use of such materials results in the need for frequent replacement in an industrial setting, increasing the system cost.

Techniques to stabilize bulk metal oxides for cycling, such as sintering powders into pellets and synthesizing sol-gels, show mixed results. Agglomerated and sieved Fe₂O₃ powder, stabilized by sintering at 1173 K, shows improved cycle stability for up to six redox cycles at temperatures below 1173 K. [6, 11] However, sintered pellets of Fe₂O₃ show deactivation in only four cycles at 1023 K. [9] Sol-gel derived Fe₂O₃ materials show consistent degradation over seven cycles at temperatures between 623 K and 723 K. [12]

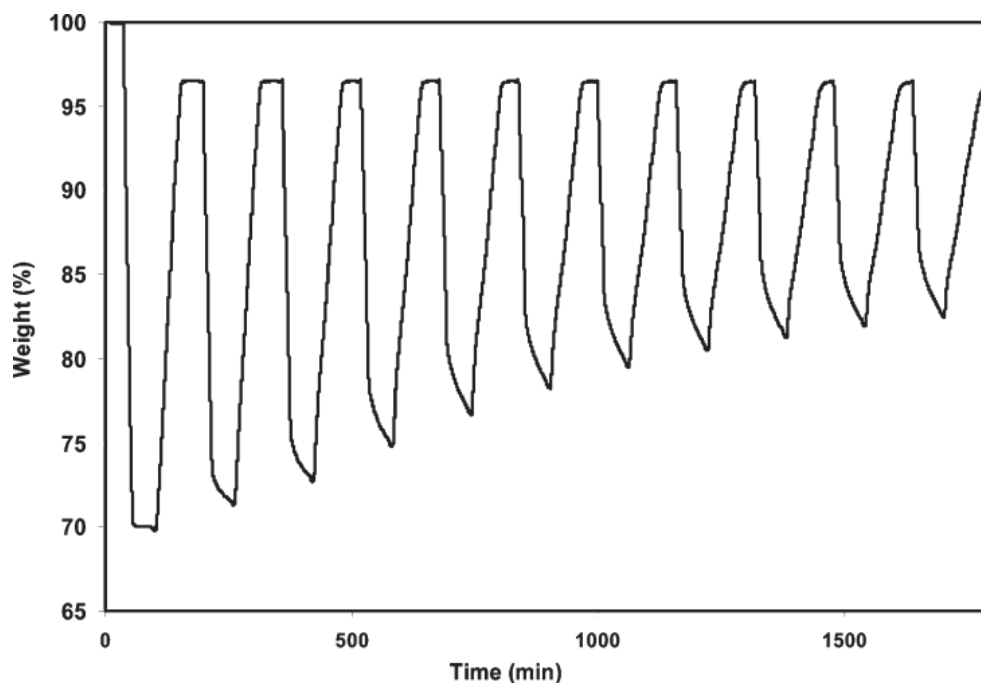


Figure 2.2: Reduction and oxidation cycles of bulk commercially available Fe_2O_3 show systematic degradation over time, from Gupta *et al.* Energy & Fuels; 2007;21:2900 (Ref. [7]).

To further stabilize the metal oxides, secondary materials are added as binders to serve as supports to maintain metal oxide distribution and pore volume to sustain gas/metal oxide contact, and to increase particle integrity. This approach is implemented in materials synthesis for the chemical looping combustion (CLC) process, which uses O_2 rather than H_2O as an oxidizing agent to produce heat for electricity generation. [13] Binders can be co-precipitated with the metal oxide, included in the sol-gel preparation method, physically mixed with the metal oxide and sintered, or used as a porous substrate onto which the metal oxide is deposited. Two types of binders are considered: inert binders and binders that react chemically with the metal oxide.

The most common inert binder is ZrO_2 or yttria-stabilized ZrO_2 (YSZ). Due to the phase transformation from monoclinic ZrO_2 to tetragonal ZrO_2 near 1273 K, and the associated pore-destroying volume change, yttria is often added to stabilize the zirconia in the tetragonal phase over a wider temperature range. [4] Samples of NiO physically mixed with ZrO_2 and YSZ,

shaped into 2 mm particles and calcined, show significantly improved reduction extent over bulk NiO particles when cycled at 1273 K. [14] Samples of 80% by mass Fe₂O₃ mixed with ZrO₂ made using freeze granulation, a method of forming physically mixed particles of uniform size, show high reduction and oxidation rates at 1223 K. [15] Mixtures of Fe₂O₃ and YSZ cycle over 100 times with excellent repeatability, attributed to the oxygen ion conduction capacity of YSZ. [4] Common binders Al₂O₃ and TiO₂ often react with the metal oxides used in chemical looping processes. Regardless, particles made with reactive binders usually show superior cycling properties to bulk samples. When Al₂O₃ is used as a binder, FeAl₂O₄, MnAl₂O₄, NiAl₂O₄, and CoAl₂O₄ form during reduction, but the reduction extent and cyclability are superior to those of bulk metal oxide materials. These improvements are attributed to the increased stability of pore and particle structures. [14, 16-21] Samples prepared with TiO₂ form FeTiO₂, but still prove highly cyclable, and produce consistent H₂ amounts for five cycles; a result attributed to the enhanced oxygen anion conduction through the TiO₂ phase. [21, 22]

Literature regarding the cyclability and properties of various metal oxide-binder combinations is vast, and more comprehensive summaries are available elsewhere. [4, 23] Regardless of the method of sample production, cyclability is key in the investigation of any new chemistry or material kinetics for the CLH process and should be a major study parameter.

2.3 Reaction Thermodynamics

Criteria 2 and 3 are properties of the CO/CO₂ and H₂/H₂O equilibrium with the oxidized and reduced states of a metal oxide, assuming a system with rapid kinetics. The equilibrium constant of Eq. 2.2, $K_{\text{Eq,H}_2} = p_{\text{H}_2\text{O}}/p_{\text{H}_2}$, and that of Eq. 2.3, $K_{\text{Eq,CO}} = p_{\text{CO}_2}/p_{\text{CO}}$ (where p = partial pressure), determine the limiting amount of H₂ and CO remaining in the syngas after the reduction step. [4, 6, 7, 24] Table 2.1 shows the starting oxide stoichiometry, the final reduced

material stoichiometry, and the equilibrium constant at 873 K for the CO and H₂ reduction of metal oxides considered as candidates for chemical looping processes. A large equilibrium constant indicates high conversion of H₂ to H₂O or CO to CO₂ during the reduction reaction, while a small equilibrium constant indicates a lower conversion. This results in a loss of syngas energy content as H₂ and CO are present in the gas exiting the reactor. [24] Equilibrium constants for oxides of Fe, Ni, Co, Cu, and Mn predict nearly 100% conversion of CO and H₂ to CO₂ and H₂O during the reduction step, which would result in a nearly pure CO₂ stream after H₂O condensation. [7]

Metal Oxide	Reduction Product	pH₂O/pH₂ (K_{Eq,H2})	pCO₂/pCO (K_{Eq,CO})	Conversion of H₂ to H₂O (%)
NiO	Ni	250	800	0.4
Cu ₂ O	Cu	1.5x10 ⁹	1.5x10 ¹⁰	0
CoO	Co	44	100	2.3
Mn ₃ O ₄	MnO	1.0x10 ⁵	1.5x10 ⁴	0
Fe ₃ O ₄	Fe	1.3	1	75
Fe ₂ O ₃	Fe ₃ O ₄	5.0x10 ⁵	8.0x10 ⁵	0
SnO ₂	Sn	2.5	5	40

Table 2.1: Equilibrium constants and H₂ to H₂O conversion at 873 K for common chemical looping candidate metal oxides. [6, 7, 24]

For conventional CLC processes, high conversion of H₂ to H₂O and CO to CO₂ during the reduction step is optimal because the re-oxidation is performed with O₂. For the CLH process, re-oxidation is performed using H₂O, and while high conversion of H₂ to H₂O is desired in the reduction step, the corollary is low conversion of H₂O to H₂ during oxidation. [7] The inverse of Eq. 2.2's equilibrium constant expresses the equilibrium for the H₂O oxidation of the reduced metal oxide, Eq. 2.3. Low H₂O conversion to H₂ makes regeneration of NiO and CoO difficult, and the regeneration of Cu₂O, Mn₃O₄ and Fe₂O₃ unlikely under reaction conditions. [4] Although the Sn system has reasonable conversion of H₂O to H₂ during oxidation, the amounts

of CO and H₂ that would exit the reactor would be nearly 8%. Additionally, the melting point of Sn is 505 K, significantly below the operating temperature of a CLH reactor. [7]

2.4 Fe-based CLH System

The Fe-based oxide system is unique because of the formation of Fe₃O₄, an intermediate oxide, between the reduced state, Fe, and the fully oxidized state, Fe₂O₃. Furthermore, the oxidation of Fe to Fe₃O₄ is predicted to have a high conversion of H₂O to H₂: nearly 75%. [7, 25, 26] An O₂ oxidation is necessary to generate Fe₂O₃ due to the large equilibrium constant for the H₂O oxidation of Fe₃O₄ to Fe₂O₃. Conversely, the large oxidation equilibrium constant for oxidation of Fe₃O₄ to Fe₂O₃ allows high conversions of H₂ and CO during the reduction of Fe₂O₃. This intermediate phase allows H₂ production with high H₂O to H₂ conversion from the reduced metal oxide to form Fe₃O₄, and a subsequent O₂ oxidation regenerates a phase able to convert nearly all of the H₂ and CO to H₂O and CO₂ during the reduction step. The phases present in the Fe-based oxide system and the pH₂O/pH₂ and pCO₂/pCO ranges in which they are stable are shown in Figure 2.3. The lines represent the equilibrium constants for phase transitions at each temperature. For example, at 673 K (400°C), Fe metal would oxidize to Fe₃O₄ in a gas with pCO₂/pCO ~ 1.

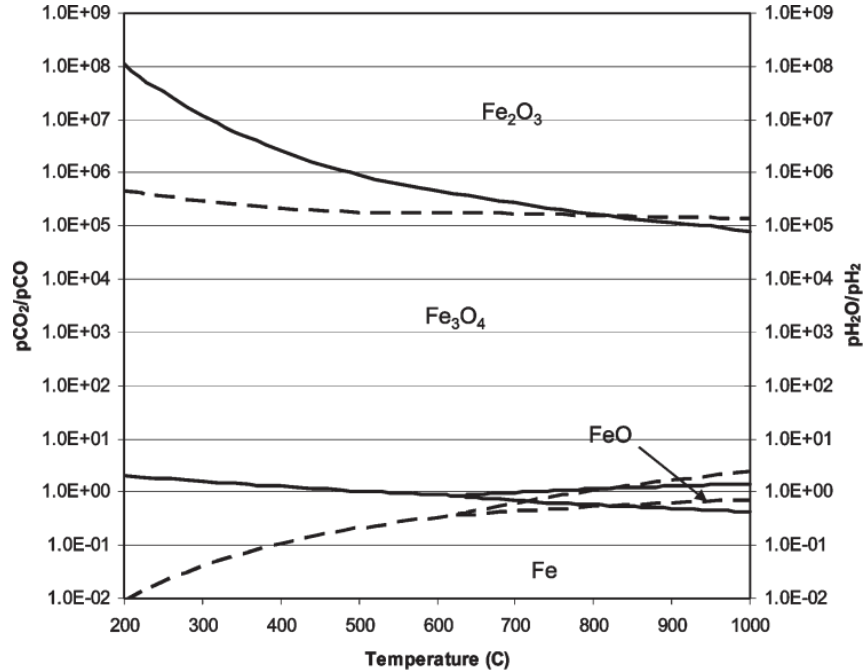
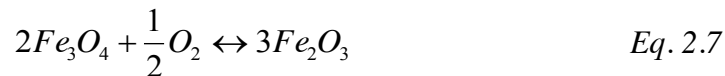
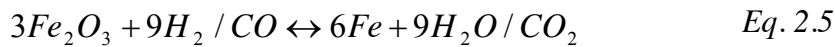


Figure 2.3: The equilibrium phase diagram for the Fe-,FeO-, Fe₃O₄-,Fe₂O₃ system with CO/CO₂ (--) and H₂/H₂O (- -). The lines are the equilibrium constants at each temperature, and indicate the gas composition at which the phase transition will occur from Gupta *et al.* Energy & Fuels; 2007;21:2900 (Ref. [7])

Due to these unique equilibrium phases, and its abundance, low cost, and low toxicity, iron (Fe) remains the most studied metal oxide for the CLH process. [2, 7, 12] Consequently, the most common CLH process to date (shown in Figure 2.4) is expressed by the following reactions:



The O₂ regeneration step does add complexity to the CLH system and results in a loss of at least 11% of the potential H₂ production, since the H₂ and CO used to reduce the Fe₂O₃ to Fe₃O₄ cannot be recovered as H₂. Despite the loss of potential H₂ recovery, the O₂ oxidation of Fe₃O₄

has a large reaction enthalpy, allowing the generation of heat, and subsequently electricity, during the cycle. [4, 27]

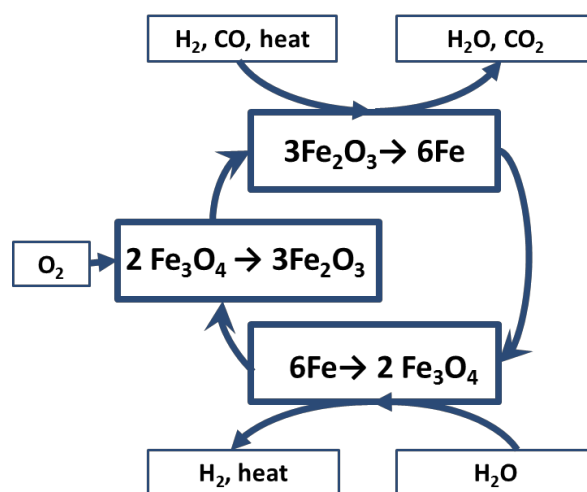


Figure 2.4: The current state-of-the-art CLH process includes an O_2 oxidation step, in which a portion of possible H_2 production is not utilized.

2.5 CLH Reactor Design

The equilibrium conditions between the solid Fe-based oxide and the gas phase necessitate contact with the Fe_2O_3 phase during the reduction step in order for the H_2 and CO to be completely converted to CO_2 and H_2O . [6] Although a high conversion of the metal oxide is desired, more important is maximizing the conversion of H_2 and CO to H_2O and CO_2 during the reduction step. For CO_2 to be sequesterable, the impurity levels must be less than 5%. [28] Additionally, any CO or H_2 that remains unconverted to CO_2 or H_2O becomes unutilized chemical energy.

Typically, a fluidized bed, packed bed, or a moving bed reactor is used for bench-scale chemical looping experiments. [2, 6, 11, 29] During the reduction step, syngas is introduced into the reactor until all the Fe_2O_3 is consumed and breakthrough of H_2 and CO is observed. The reactor is purged, and then steam is introduced to generate H_2 . When H_2O oxidation is complete,

O₂ is introduced to regenerate Fe₂O₃, then the reactor is purged of oxidizing gasses and the process is repeated. In a fluidized bed reactor, gas and solid phases are well mixed axially and radially. Gasses entering the reactor are mixed with reacted gasses in the reactor volume, and particles throughout the bed are of uniform conversion due to their exposure to gasses of similar composition. In this configuration, conversion of the Fe₂O₃ beyond Fe₃O₄ before breakthrough of H₂ and CO is difficult to obtain because H₂O/H₂ and CO/CO₂ ratios are high in well-mixed gas. [29] This reaction is sufficient for a CLC process because the desired product is the heat generated during O₂ oxidation of the reduced material. [24] Since Fe₃O₄ cannot be oxidized to produce H₂, the conversion of Fe₂O₃ must be greater for the CLH process, making the fluidized bed a poor choice as a reactor. [29]

Greater conversion is achieved in a packed bed reactor because, ideally, gasses behave as plug flow rather than exhibiting axial mixing. The H₂/H₂O and CO/CO₂ ratios in syngas entering a reactor are often large enough to produce FeO or Fe metal in the first portion of the reactor before all Fe₂O₃ is consumed through the entire bed. [6] A countercurrent moving bed reactor has been shown to have the greatest solid conversion while maximizing the H₂ and CO conversion. [29] Conversion of the solid material is nearly 50% without H₂ or CO breakthrough. An additional benefit to the countercurrent moving bed reactor is that the flows of syngas and steam are continuous, and no high-temperature valves are required to switch gasses entering the reactors.

2.6 Alternative CLH Metal Oxides

Few studies to date comprehensively investigate alternative metal oxides to Fe₂O₃ for the CLH process. A kinetic investigation of the H₂O oxidation of a reduced Cu-Fe -Al₂O₃ co-precipitated material between 550°C and 850°C shows significant H₂ production, but the reduced

and oxidized phases remain unverified, and the conversion of H₂ and CO during the reduction step is unknown, which makes an assessment of the applicability to the CLH process difficult. [30] Similarly, a kinetic investigation of Mn- and Zn- Fe₃O₄ materials, synthesized from physically mixed powders, shows an increase in the oxidation rate and a decrease in the activation energy of the H₂O oxidation between 777 K and 1173 K. However, reduced and re-oxidized products were not identified, and the material equilibrium with the H₂/H₂O and CO/CO₂ systems was not discussed. [31] A study of the reduction and subsequent water oxidation of CoFe₂O₄ and Fe₃O₄ films deposited on high surface area ZrO₂ using atomic layer deposition (ALD) shows excellent cyclability for the CoFe₂O₄ material, which produces twice the amount of H₂ as the Fe₃O₄ under the same cycling conditions. [32] This investigation did not confirm CoFe₂O₄ as the product of the H₂O oxidation, and does not discuss equilibrium with the CO/CO₂ or H₂/H₂O systems, but does identify a CoFe alloy as the reduction product. Unlike the Cu-Fe-Al₂O₃, ZnFe₂O₄, and MnFe₂O₄ systems, the mixed metal spinels CoFe₂O₄ and NiFe₂O₄ have been examined thermodynamically in a study that concluded the systems have promising thermodynamic properties for a CLH process. [33]

Spinels have the structure AB₂O₄, where A is an M²⁺ ion and B is an M³⁺ ion. [34] The spinel Fe₃O₄ contains one Fe²⁺ ion for every two Fe³⁺ ions. In the mixed metal spinels CoFe₂O₄ and NiFe₂O₄, the Co and Ni possess a 2+ charge while all the Fe ions exist in the 3+ oxidation state. Substitution of Co²⁺ or Ni²⁺ into Fe₃O₄ is known to destabilize the spinel phase, making it easier to reduce, while still being capable of mixed metal spinel regeneration through water oxidation. [35] In high temperature redox cycles, addition of Co²⁺ or Ni²⁺ decreases the temperature necessary to reduce the metal oxide to FeO and CoO, or FeO and NiO from 1760 K

to 1700 K, and mixed metal spinel materials have been investigated several times for these processes. [36-39]

For the lower temperature CLH system, the effect of the Co^{2+} or Ni^{2+} is not as well established. Syngas reduction has the potential to leave the material in a more reduced state than thermal reduction can. Calculations between 300 K and 1000 K predict the reduction of mixed metal spinels containing Fe, Co, and Ni to their metallic states will have higher conversions of H_2 to H_2O and CO to CO_2 than are attainable with Fe_3O_4 , while also having lower H_2 to H_2O conversions than NiO and CoO . [33] The authors attribute this to a reduced NiO and CoO activity when mixed with a Fe^{3+} material. Similar to the thermal reduction of mixed metal ferrites, this analysis predicts mixed metal ferrite regeneration during H_2O oxidation. The referenced study [32] considers stable cycling of these mixed metal spinels to be dubious in the CLH system due to the possibility of preferential oxidation and subsequent phase segregation of the metal oxides Fe_3O_4 , CoO , and NiO . Forming these products rather than the mixed metal spinels would change the equilibrium conversion of gasses during reduction and would decrease the H_2 yield of the system. Additional H_2 production comes from further oxidation of Fe^{2+} ions to Fe^{3+} ions in the mixed metal spinel. No experimental investigation accompanied these calculations and only the equilibria shown in Eq. 2.8 and Eq. 2.9 are considered. Intermediate equilibrium compositions are not investigated.



2.7 References

- [1] Farmer R. 2009 DOE Hydrogen Program & Vehicle Technologies Program. 2009. p. http://www.hydrogen.energy.gov/pdfs/review09/pd_0_farmer.pdf.

- [2] Solunke R, Vesper G. Hydrogen Production via Chemical Looping Steam Reforming in a Periodically Operated Fixed-Bed Reactor. *Ind Eng Chem Res.* 2010;49:11037-44.
- [3] Smith B, Loganathan M, Shantha M. A Review of the Water Gas Shift Reaction Kinetics. *Int J Chem React Eng.* 2010;8.
- [4] Fan L. *Chemical Looping Systems for Fossil Energy Conversion.* Hoboken, NJ: John Wiley & Sons, Inc.; 2010.
- [5] Sircar S, Golden TC. Purification of Hydrogen by Pressure Swing Adsorption. 2000;35:667-87.
- [6] Bohn CD, Muller CR, Cleeton JP, Hayhurst AN, Davidson JF, Scott SA, et al. Production of Very Pure Hydrogen with Simultaneous Capture of Carbon Dioxide using the Redox Reactions of Iron Oxides in Packed Beds. *Ind Eng Chem Res* 2008;47:7623-30.
- [7] Gupta P, Velazquez-Vargas L, Fan L. Syngas Redox (SGR) Process to Produce Hydrogen from Coal Derived Syngas. *Energy Fuels.* 2007;21:2900-8.
- [8] Li F, Kim H, Wang D, Zeng L, Chen J, Fan L. Syngas Chemical Looping Gasification Process: Oxygen Carrier Particle Selection and Performance. *Energy Fuels.* 2009;23:4182-9.
- [9] Bleeker MF, Veringa HJ, Kersten SRA. Pure Hydrogen Production from Pyrolysis Oil Using the Steam-Iron Process: Effects of Temperature and Iron Oxide Conversion in the Reduction. *Ind Eng Chem Res.* 2010;49:53-64.
- [10] Bleeker MF, Veringa HJ, Kersten SRA. Deactivation of iron oxide used in the steam-iron process to produce hydrogen. *Appl Catal, A.* 2009;357:5-17.
- [11] Muller C, Bohn C, Song Q, Scott S, Dennis J. The production of separate streams of pure hydrogen and carbon dioxide from coal via an iron-oxide redox cycle. *Chem Eng J* 2011;166:1052-60.
- [12] Lorente E, Pena JA, Herguido J. Kinetic study of the redox process for separation and storing hydrogen: Oxidation stage and ageing of solid. *Int J Hydrogen Energy.* 2008;33:615-26.
- [13] Fang H, Halbin L, Zengli Z. Advancements in Development of Chemical-Looping Combustion: A Review. *International Journal of Chemical Engineering.* 2009:710515.

[14] Lee J-B, Park C-S, Choi S-I, Song Y-W, Kim Y-H, Yang H-S. Redox Characteristics of Various Kinds of Oxygen Carriers for Hydrogen Fueled Chemical-Looping Combustion. *Journal of Industrial and Engineering Chemistry*. 2005;11:96-102.

[15] Mattisson T, Johansson M, Lyngfelt A. Multicycle Reduction and Oxidation of Different Types of Iron Oxide Particles - Application to Chemical-Looping Combustion. *Energy & Fuels*. 2004;18.

[16] Mattisson T, Jardnas A, Lyngfelt A. Reactivity of Some Metal Oxides Supported on Alumina with Alternating Methane and Oxygen Application for Chemical-Looping Combustion. *Energy Fuels*. 2003; 17:643-51.

[17] Ishida M, Jin H, Okamoto T. Kinetic Behavior of Solid Particle in Chemical-Looping Combustion: Suppressing Carbon Deposition in Reduction. *Energy & Fuels*. 1998;12:223-9.

[18] Ishida M, Takeshita K, Suzuki K, Ohba T. Application of Fe₂O₃-Al₂O₃ Composite Particles as Solid Looping Material of the Chemical-Loop Combustor. *Energy & Fuels*. 2005;19:2514-8.

[19] Abad A, Garcia-Labiano F, Diego LF, Gayan P, Adanez J. Reduction Kinetics of Cu-, Ni-, and Fe-Based Oxygen Carriers Using Syngas (CO + H₂) for Chemical-Looping Combustion. *Energy & Fuels*. 2007;21:1843-53.

[20] Cho P, Mattisson T, Lyngfelt A. Comparison of iron-, nickel-, copper- and manganese-based oxygen carriers for chemical-looping combustion. *Fuel*. 2004;83:1215.

[21] Chen S, Shi Q, Xue Z, Sun X, Xiang W. Experimental investigation of chemical-looping hydrogen generation using Al₂O₃ or TiO₂-supported iron oxides in a batch fluidized bed. *International Journal of Hydrogen Energy*. 2011;36:8915-26.

[22] Li F, Sun Z, Luo S, Fan L-S. Ionic diffusion in the oxidation of iron-effect of support and its implications to chemical looping applications. *Energy & Environmental Science*. 2011;4:876-80.

[23] Lyngfelt A, Johansson M, Mattisson T. Chemical Looping Combustion - Status of Development. 9th International Conference on Circulating Fluidized Beds. Hamburg, Germany 2008.

[24] Jerndal E, Mattisson T, Lyngfelt A. Thermal Analysis of Chemical-Looping Combustion. *Chemical Engineering Research and Design*. 2006;84:795-806.

[25] Svoboda K, Siewiorek A, Baxter D, Rogut J, Pohorely M. Thermodynamic possibilities and constraints for pure hydrogen production by a nickel and cobalt-based chemical looping process at lower temperatures. *Energy Convers Manag.* 2008;49:221-31.

[26] Svoboda K, Slowinski G, Rogut J, Baxter D. Thermodynamic possibilities and constraints for pure hydrogen production by iron based chemical looping process at lower temperatures. *Energy Convers Manag.* 2007;48:3063-73.

[27] Fan L, Li F, Ramkumar S. Utilization of a chemical looping strategy in coal gasification processes. *Particuology.* 2008;6:131-42.

[28] Visser Ed, Hendriks C, Barrio M, Mølnvik MJ, Koeijer Gd, Liljemark S, et al. Dynamic CO₂ quality recommendations. *Greenhouse Gas Control.* 2008;2:478-84.

[29] Li F, Zeng L, Velazquez-Vargas L, Yoscovitis Z, Fan L. Syngas Chemical Looping Gasification Process: Bench-scale Studies and Reactor Simulations. *AIChE J.* 2010;56:2186-99.

[30] Chiron F-X, Patience GS. Kinetics of mixed copper–iron based oxygen carriers for hydrogen production by chemical looping water splitting. *International Journal of Hydrogen Energy.* 2012;37:10526-38.

[31] Go KS, Son SR, Kim SD. Reaction kinetics of reduction and oxidation of metal oxides for hydrogen production. *Int J Hydrogen Energy.* 2008;33:5986-95.

[32] Scheffe JR, Allendorf MD, Coker EN, Jacobs BW, McDaniel AH, Weimer AW. Hydrogen Production via Chemical Looping Redox Cycles Using Atomic Layer Deposition-Synthesized Iron Oxide and Cobalt Ferrites. *Chem Mater.* 2011;23:2030-8.

[33] Svoboda K, Siewiorek A, Baxter D, Rogut J, Pohorely M. Thermodynamic possibilities and constraints for pure hydrogen production by a nickel and cobalt-based chemical looping process at lower temperatures. *Energy Convers Manage.* 2008;49:221-31.

[34] Graves P, Johnston C, Campaniello J. Raman Scattering in Spinel Structure Ferrites. *Mater Res Bull.* 1988;23:1651-60.

[35] Allendorf M, Diver R, Siegel N, Miller J. Two-Step Water Splitting Using Mixed-Metal Ferrites: Thermodynamic Analysis and Characterization of Synthesized Materials. *Energy Fuels.* 2008;4115-24.

- [36] Kodama T, Gokon N, Yamamoto R. Thermochemical two-step water splitting by ZrO₂-supported Ni_xFe_{3-x}O₄ for solar hydrogen production. *Solar Energy*. 2008;82:73.
- [37] Kodama T, Kondoh Y, Yamamoto R, Andou H, Satou N. Thermochemical hydrogen production by a redox system of ZrO₂-supported Co(II)-ferrite. *Solar Energy*. 2005;78:623.
- [38] Kodama T, Nakamuro Y, Mizuno T. A two-step thermochemical water splitting by iron-oxide on stabilized zirconia. *Journal of Solar Energy Engineering-Transactions of the Asme*. 2006;128:3.
- [39] Tamaura Y, Stienfeld A, Kuhn P, Ehrensberger K. PRODUCTION OF SOLAR HYDROGEN BY A NOVEL, 2-STEP, WATER-SPLITTING THERMOCHEMICAL CYCLE. *Energy*. 1995;20:325.

Chapter 3: Substrate Selection and Materials Analysis

3.1 Abstract

To establish CoFe_2O_4 and NiFe_2O_4 as candidate materials for the chemical looping hydrogen (CLH) process, the mixed metal oxides were deposited on ZrO_2 substrates and cycled. The CoFe_2O_4 and NiFe_2O_4 phases were identified using Raman spectroscopy before and after cycling, confirming regeneration with H_2O oxidation. The absence of a c- ZrO_2 phase indicated minimal interaction between the metal oxide and ZrO_2 support. Materials proved to be cycleable at 873 K, and oxidation rates were shown to have a clear dependence on H_2O concentration and temperature. Post-cycling analysis showed a decrease in material surface area, but the metal cations on the ZrO_2 showed no sign of phase segregation.

3.2 Introduction

The chemical looping hydrogen (CLH) process generates pure and separated streams of H_2 and CO_2 from syngas from any source, and it is proposed as a method of H_2 production with integrated CO_2 capture for future gasification systems.[1] The process involves a metal oxide material that is first reduced simultaneously with H_2 and CO , then oxidized in H_2O to generate H_2 and regenerate the original metal oxide.[2] Iron is the current state-of-the art material for the CLH process due to its favorable thermodynamics, low toxicity, and low cost. [1] The mixed metal spinels NiFe_2O_4 and CoFe_2O_4 are possible metal oxides for the CLH process; however, the investigation of these materials to date includes only preliminary thermodynamic results and limited cycling data. One concern with these materials is the preferential re-oxidation of the respective metals, which could inhibit regeneration of the mixed metal spinel. [3] Success at cycling CoFe_2O_4 is reported, though regeneration of the mixed metal spinel after cycling was not confirmed. [4] No investigation into NiFe_2O_4 is reported in literature to date. A comprehensive

study, including cyclability analysis and phase identification, is necessary to confirm the candidacy of these mixed metal ferrites for the CHL process and to justify further investigation of the materials.

The specific goals of this study were to investigate the cyclability characteristics of CoFe_2O_4 and NiFe_2O_4 , to determine if the H_2O oxidation regenerates the mixed metal spinels CoFe_2O_4 and NiFe_2O_4 , and to perform preliminary investigations into the effects of H_2O concentration, temperature, and metal oxide composition on the oxidation process. The H_2 production was used as a metric to determine the material cyclability; a material with consistent H_2 production peak values and total H_2 production per cycle was considered to be cycle stable. In accordance with the overall goal of H_2 production, material performance was assessed based on H_2 production capacity, cyclability, and ability to regenerate the mixed metal oxide phase. Based on previous literature suggesting successful material cycling with metal oxides supported on ZrO_2 , an inert binder was chosen to minimize the binder-metal oxide interaction and to allow unhindered investigation into the nature of CoFe_2O_4 and NiFe_2O_4 reduction and oxidation cycles.

3.3 Materials and Methods

3.3.1 Samples

Metal oxide samples were prepared in the laboratory using the incipient wetness method. [5, 6] Iron nitrate ($\text{Fe}(\text{NO}_3)_3 \cdot 9\text{H}_2\text{O}$, Sigma Aldrich, 98%), nickel nitrate ($\text{Ni}(\text{NO}_3)_2 \cdot 6\text{H}_2\text{O}$, Alfa Aesar, 98%), and cobalt nitrate ($\text{Co}(\text{NO}_3)_2 \cdot 6\text{H}_2\text{O}$, Alfa Aesar, 98%) were dissolved in de-ionized water to form 2 molar aqueous solutions of metal cations. Catalyst pellets made of approximately 20 nm sintered ZrO_2 spheres (Alfa Aesar, 99%, 0.31 cc/g, 50 m²/g), were crushed and sieved to 110 – 175 μm diameter particle size and subsequently mixed with the aqueous metal nitrate solutions of the desired stoichiometry. Solution volumes equal to the calculated

pore volume of the ZrO_2 samples were added using a calibrated pipette. Samples were dried at $333 \pm 5 \text{ K}$ in a vacuum oven for eight hours after each addition of the nitrate solution. When the desired mass percent of metal oxide (20%) was reached, the samples were calcined at $873 \pm 10 \text{ K}$ in air for eight hours.

3.3.2 Sample Characterization

The metal oxide mass percents and cation ratios were confirmed via inductively coupled plasma-atomic emission spectroscopy (ICP-AES). Phase identification before and after cycling was performed with a Raman spectrometer using a 532 nm Nd:YAG laser with a 1 μm spot size. Calibrations were performed with a with a neon lamp. Multiple sites on each material were sampled to ensure sample conformity. Surface areas were measured using Brunauer-Emmett-Teller (BET) surface area analysis, and crushed samples were examined visually using a Philips CM 100 Transmission Electron Microscope. Samples were also examined with a JSM-7401F field emission scanning electron microscope (FESEM) equipped with an energy dispersive X-ray spectrometer (EDS) for surface elemental analysis and mapping.

3.3.3 Sample Cyclability

Cyclability analysis was performed in a stagnation flow reactor, shown in Figure 3.1.[4] Reactant gas flow, controlled using calibrated mass flow controllers, proceeded through an insulated and heated stainless steel manifold to the reactor tube. A shallow, loosely packed bed of ferrite sample was placed on a flat ZrO_2 sample holder positioned at the bottom of the vertically oriented, closed-end Al_2O_3 reactor tube. Reactant gases entered the reactor and impinged on the sample through an Al_2O_3 tube situated concentrically inside an outer closed-end tube. After contact with the sample, the gases exited the reactor by flowing up between the tubes and out the top of the reactor. Exiting gas concentrations were measured with a differentially

pumped, modulated effusive beam mass spectrometer (Extrell C50, 500 amu), which was designed to increase detection sensitivity in the presence of background gases. The mass spectrometer was calibrated daily using analytical standard gases, with 4-point calibrations in the H_2 , CO, and CO_2 partial pressure ranges observed during reduction and oxidation reactions. To prevent H_2O from entering the mass spectrometer during oxidation, steam was cryogenically removed from the gas stream in a liquid nitrogen cooled trap prior to gas sampling. A vacuum pump and pressure controller were used to maintain a constant 1 kPa pressure in the system during the reaction.

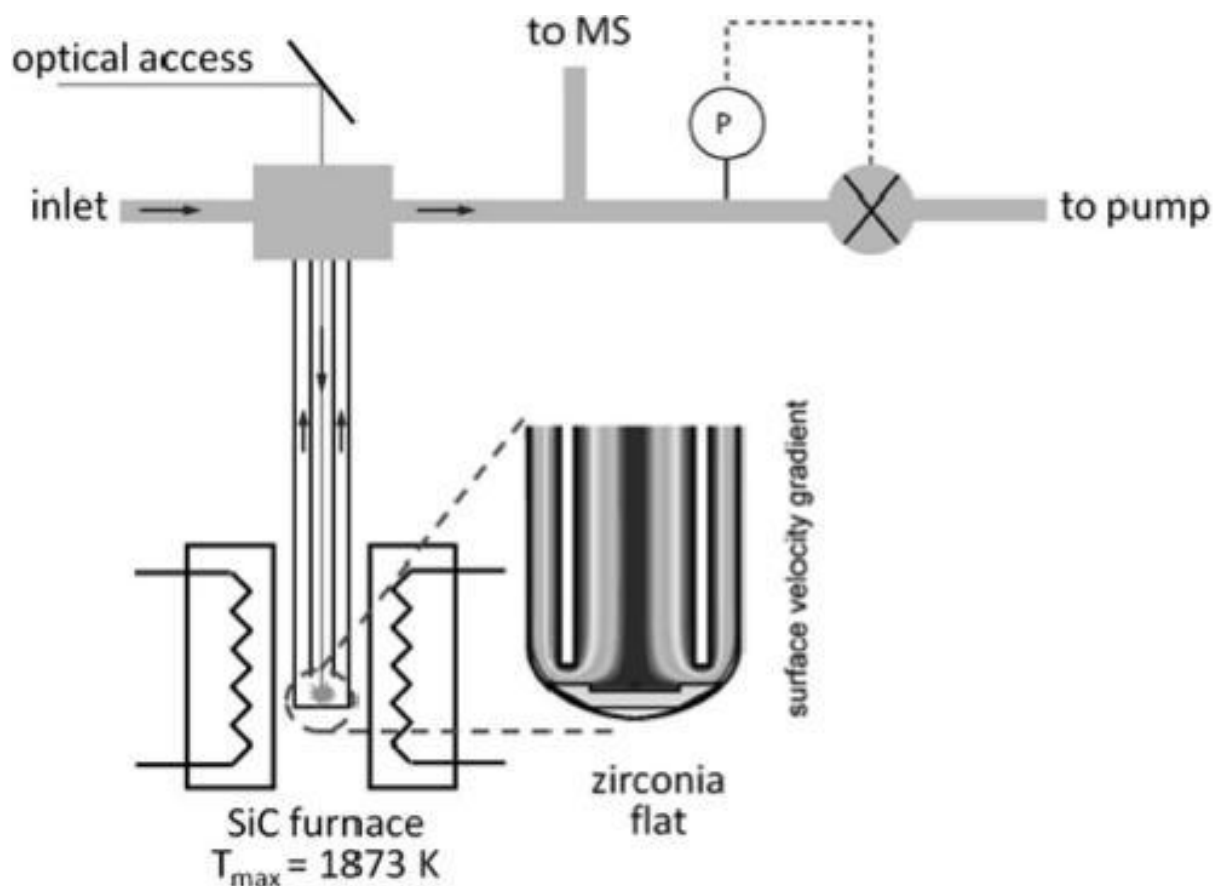


Figure 3.1: Stagnation flow reactor. Gases flow through the center tube and onto the sample at the bottom of the closed end tube. Dimensions are such to minimize velocity gradients across the sample, from *Scheffe et al. Chemistry of Materials.2010;23* (Ref. [4]).

In accordance with chemical looping conditions, samples were reduced for ten minutes at 873 K using a syngas mixture containing 2% CO₂/ 2% H₂/2% CO/Balance He to simulate reduction conditions during the CLH process. Oxidations under 10% H₂O/balance He followed and continued until the H₂ levels returned to baseline as observed before cycling. Steam was generated at 348 K using a RASIRC steam generation unit incorporating a humidity sensor that allowed accurate water flow rate control and recording during the reaction.

3.4 Experimental Results and Analysis

3.4.1 Sample Characterization

Sample surface areas and mass percents are listed in Table 3.1. The surface area of the ZrO₂ substrate was 49.1 m²/g prior to deposition. Surface areas decreased with the addition of the metal oxide due to both the addition of mass and to pore blocking in the substrate. Mass percents of metal oxide and cation ratios, measured with ICP-AES, were verified to be similar to the values calculated from the volumes of nitrate solution used in synthesis. Samples at 10X magnification show 100-200 μm particles, which are uniform in color. (Figure 3.2 a) Visual examination of crushed particles revealed consistent coloring throughout, confirming dispersion of the metal oxide into the interior of the particle. Analysis of the crushed particle with EDS confirmed uniform distribution of cations throughout the particle. Inspection of the particle exterior and interior using SEM revealed a rough, porous surface. (Figure 3.2 b) Visual TEM

Material	Mass Percent metal oxide	Cation Ratio	Surface Area (m²/g)
Blank ZrO ₂	none	none	49.1
Fe ₂ O ₃	20.7	All Fe	35
CoFe ₂ O ₄	18.7	2.1:1 Fe:Co	33.3
NiFe ₂ O ₄	21.6	2:1 Fe:Ni	38.9

Table 3.1: Sample mass percents and surface areas.

inspection of a blank ZrO_2 sample confirmed the morphology of the ZrO_2 substrate material as sintered ~ 20 nm particles. (Figure 3.2 c) Similar images of an annealed and crushed Fe_2O_3 sample showed metal oxide materials exist as 100-200 nm agglomerates. (Figure 3.2 d) Nitrogen Leco analysis confirmed complete removal of nitrogen from the samples during annealing.

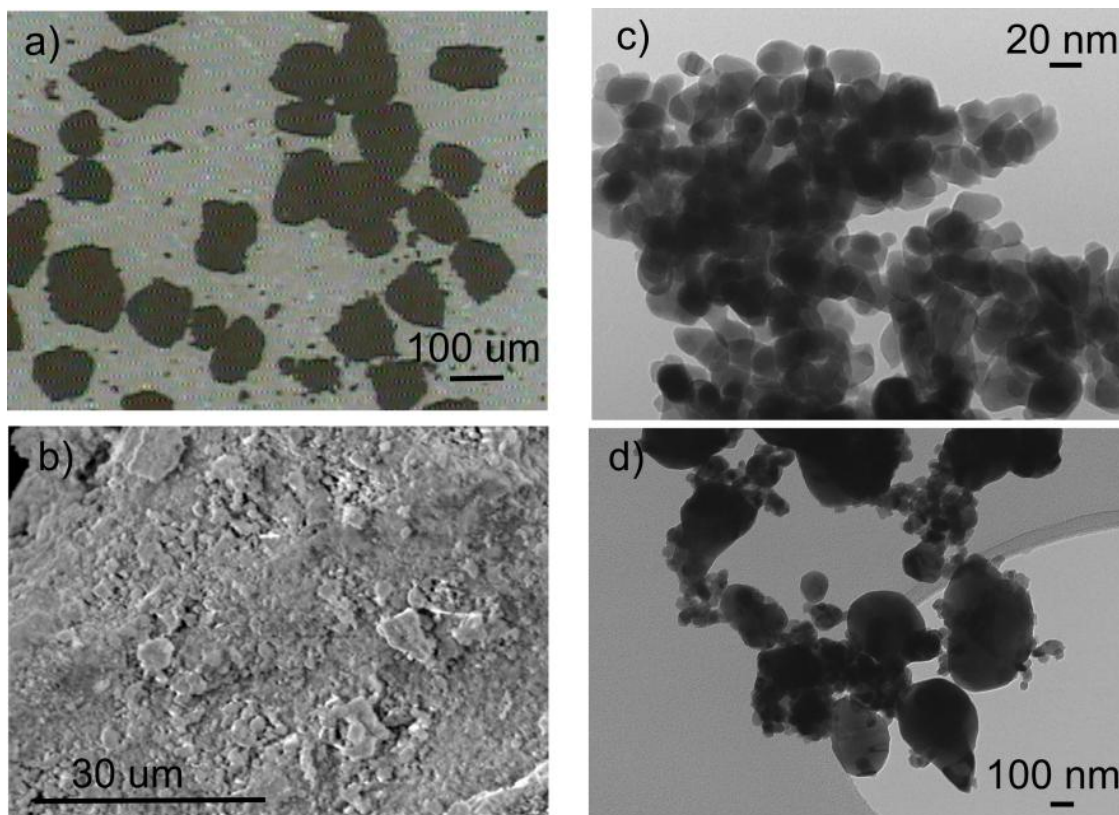


Figure 3.2: (a) NiFe_2O_4 deposited on ZrO_2 (10X) (b) SEM image of NiFe_2O_4 particle surface (c) TEM image of ZrO_2 blank shows ~ 20 nm sintered particles (d) Annealed and crushed Fe_2O_3 sample shows 100-200 nm metal oxide agglomerates.

3.4.2 Phase Identification

Spinel has the composition AB_2O_4 , where A is an M^{2+} ion and B is an M^{3+} ion. [7] The spinel Fe_3O_4 contains one Fe^{2+} ion for every two Fe^{3+} ions, while in the mixed metal spinels NiFe_2O_4 and CoFe_2O_4 , the Ni and Co possess a 2+ charge and all the Fe ions exist in the 3+

oxidation state. In a normal spinel material, all 2+ cations occupy tetrahedral sites, where the neighboring atoms are four oxygen anions and all the 3+ atoms occupy octahedral sites, where the neighboring atoms are six oxygen anions. The ferrites Fe_3O_4 , NiFe_2O_4 , and CoFe_2O_4 are all inverse spinels, meaning that all of the 2+ cations occupy octahedral sites with half of the 3+ cations, while half of the 3+ cations occupy tetrahedral sites. [8]

Each crystal structure has unique vibrational properties that depend on the structure and composition of the material. Raman spectroscopy uses inelastic light scattering caused by the excitation or de-excitation of vibrational modes in crystals to produce a spectrum that is used to identify the metal oxide phase present in a material. [9] Group theory classifies spinels as the cubic space group $\text{Fd}\bar{3}\text{m}$, and predicts spinel materials will have five Raman active vibrational modes ($\text{F}_{2\text{g}}(1), \text{E}_{\text{g}}, \text{F}_{2\text{g}}(2), \text{F}_{2\text{g}}(3)$, and $\text{A}_{1\text{g}}$). [10, 11] In a spinel, the $\text{A}_{1\text{g}}$, $\text{F}_{2\text{g}}$, and E_{g} peaks are often attributed solely to bonds between tetrahedral cations and their corresponding oxygen anions; however, much experimental evidence indicates that the octahedral cation affects peak placement as well. [9, 11, 12] A comparison of the wavenumber of the $\text{A}_{1\text{g}}$ peak between multiple inverse spinels should show no shift due to Fe^{3+} in the tetrahedral sites for each if the position is solely dependent on the tetrahedral cation, yet the peak shifts by as much as 40 cm^{-1} . Because of this, the $\text{A}_{1\text{g}}$ peak position is thought to depend on the divalent octahedral cation in the inverse spinel structure. [13] A shoulder on the CoFe_2O_4 and NiFe_2O_4 $\text{A}_{1\text{g}}$ peak is often seen, and attributed to the trivalent cation in the octahedral site. [14] Due to fast electron hopping between the Fe^{2+} and Fe^{3+} , a shoulder is not seen on the $\text{A}_{1\text{g}}$ peak of Fe_3O_4 even though it is also an inverse spinel. [9] Additionally, peaks other than the $\text{A}_{1\text{g}}$ peak are often weak in the Fe_3O_4 spectra and not observed above the experimental noise.

The potential compositions of the mixed metal ferrites include α -Fe₂O₃, γ -Fe₂O₃, Fe₃O₄, NiFe₂O₄, CoFe₂O₄, Co₃O₄, CoO, and NiO. Peak positions from literature sources for each of these materials used to identify the composition of these samples are shown in Table 3.2.

Spinels						
Material	F_{2g}(1)	E_g	F_{2g}(2)	F_{2g}(3)	A_{1g}	Ref.
Fe ₃ O ₄	193	306		538	668	[10]
	193	308		540	670	[15]
CoFe ₂ O ₄	259	302	452	576	699	[11]
		312	477		687	[16]
NiFe ₂ O ₄			460sh, 492	574sh, 595	654sh, 702	[17]
		339	490	579	700	[18]
Co ₃ O ₄			481	521	689	[12]
Non-spinel metal oxides						
α -Fe ₂ O ₃	292.5	299.3	410.9	497	611.9	[19]
γ -Fe ₂ O ₃	350	500	700			[20]
NiO		475-550			700-725	[21]
CoO	192	477	683			[22]

Table 3.2: Raman peaks for materials of interest.

Due to the known difference in composition between an O₂ oxidized Fe-only sample (Fe₂O₃) and an H₂O oxidized Fe-only sample (Fe₃O₄), the Fe-only samples were analyzed with Raman after H₂O oxidation to ensure formation of the Fe₃O₄ phase. The observed A_{1g} peak located at ~670 cm⁻¹, and the F_{2g} located at 542 cm⁻¹, correspond with literature values for Fe₃O₄, confirming the presence of the spinel material. (Figure 3.3 a)

Raman spectra of the NiFe₂O₄ sample taken before and after cycling showed the same peaks and peak positions present in each sample. Peaks at 500 cm⁻¹ and 698 cm⁻¹ correspond with literature values for the locations of the NiFe₂O₄ F_{2g} and A_{1g} peaks, respectively. (Figure 2b) Similarly, Raman data taken before and after cycling the CoFe₂O₄ samples showed unchanged peak positions (Figure 2c). The A_{1g} and F_{2g} peaks appear where expected from literature values, at 698 cm⁻¹ and 487 cm⁻¹. These spectra indicate that the NiFe₂O₄ and CoFe₂O₄

phases were regenerated, after reduction, with only H₂O oxidation. This is an important finding in light of the concern that preferential oxidation hinders the formation of the mixed metal spinel. [3] Phase segregation resulting from preferential oxidation would result in the phases Fe₃O₄ and CoO or NiO after oxidation. The peaks identified do not correspond to peaks from these metal oxide phases, but rather solely to the mixed metal spinel phases.

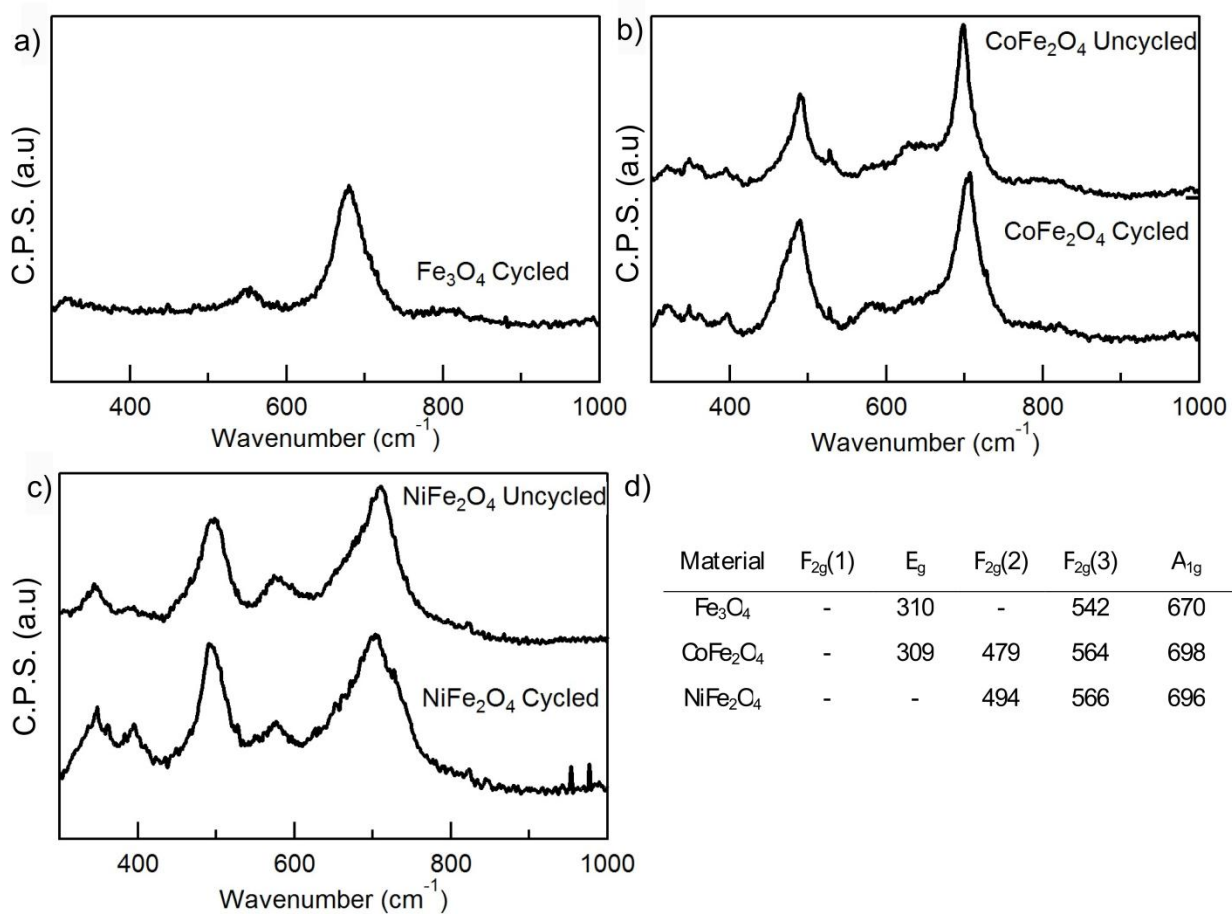


Figure 3.3 Raman spectra of a) Fe₃O₄, b) NiFe₂O₄ samples, and c) CoFe₂O₄. d) Position of each peak for comparison with Table 3.2.

3.3.3. Interaction with ZrO_2

Although ZrO_2 is considered an inert support material, Fe, Ni, and Co cations are soluble in ZrO_2 and require higher temperatures to reduce once they are dissolved in ZrO_2 . The solubility limits of Fe and Co in ZrO_2 are 25% and 15%, respectively. [23, 24] Dissolved cations are easily be detected through conventional materials analysis, as even 1% dissolved cations in the ZrO_2 matrix stabilizes the cubic ZrO_2 phase, which has distinctively different XRD spectra and Raman spectra from the monoclinic phase of ZrO_2 . [25]

Due to the non-uniform nature of the metal oxide deposition on the ZrO_2 support, and the large diameter of the laser used in Raman analysis in comparison to the size of the metal oxide particles, a signal from the ZrO_2 substrate was observed in addition to the metal oxide spectra in many spectra collected from the samples. All materials examined showed evidence of only an m- ZrO_2 phase, characterized by two peaks near 200 cm^{-1} . (Figure 3.4) A large c- ZrO_2 peak at 500 cm^{-1} is obscured by the $F_{2g}(2)$ spinel peak. Formation of c- ZrO_2 exhibits broad peaks at 250 cm^{-1} and 350 cm^{-1} . The surface is the most likely region of the sample for c- ZrO_2 to form, due to the immediate contact with the metal cations. The absence of the c- ZrO_2 phase near the surface allows us to assume that the amount of cations dissolved in the ZrO_2 is not significant. Phase analysis of the material bulk using XRD also failed to detect a c- ZrO_2 phase.

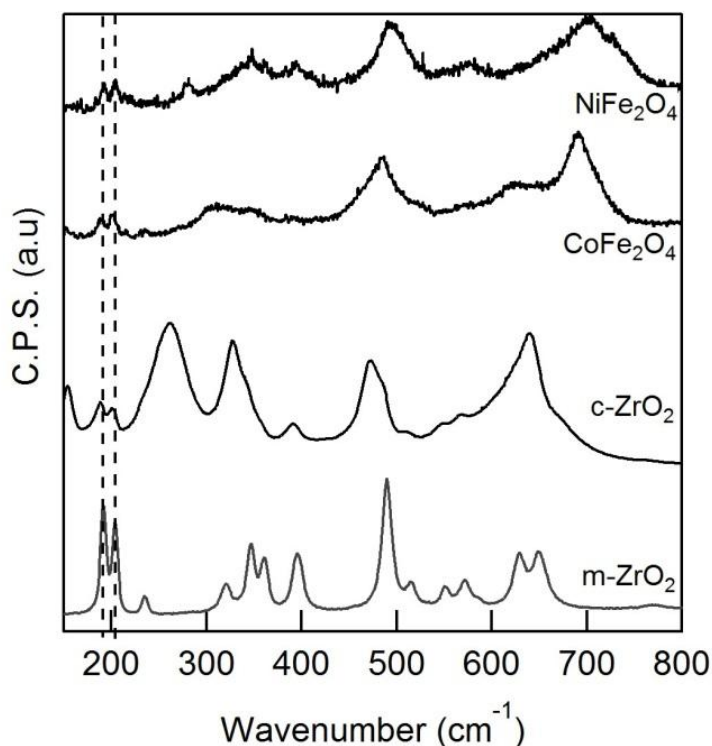


Figure 3.4: Raman spectra displaying m-ZrO₂ signal. No peaks from c-ZrO₂ are detected. The c-ZrO₂ phase is expected in the event of cation diffusion into the substrate.

3.4.4 Material Cyclability

Cyclability was established before investigating the effects of steam concentration and temperature on the oxidation, since material degradation masks the effects of changes in cycle conditions. Being the current state-of-the-art material, samples of Fe₃O₄ were cycled as a baseline material with which to compare total H₂ production and oxidation characteristics. (Figure 3.5 a) These samples showed an initial sharp decrease in total H₂ production and peak H₂ production between the first and second cycles. Subsequent cycles showed a stabilization of total H₂ production and peak H₂ production. The total amount of H₂ produced was approximately 1 mmol H₂ per gram metal oxide in the sample. Transient H₂ production behavior showed rapid oxidation that was complete in less than 100 sec. This behavior was similar to the

behavior observed using samples of Fe_3O_4 films deposited using ALD, which had total H_2 production amounts near 1 mmol/g, but with lower peak rates. [4]

Cycling of the NiFe_2O_4 samples (Figure 3.5 b) showed an initial decrease in total H_2 production and peak H_2 production, similar to the Fe-only material. After the third cycle, the material appears to stabilize, producing consistent total H_2 amounts and H_2 peak production values. The amount of H_2 produced was five times greater than the amount produced from the Fe_3O_4 sample, nearly 6 mmol/g metal oxide, though oxidation took longer to complete. Complete oxidation is not shown in Figure 3.5 b, as the H_2 levels do not return to baseline until after 800 s.

Cycling of the CoFe_2O_4 materials (Figure 3.5 c) showed that the incipient wetness CoFe_2O_4 samples were highly cycleable, with little change detected in eight cycles and consistent peak heights and total H_2 production. The amount of H_2 produced was nearly eight times greater than from the Fe_3O_4 sample, at 8 mmol/g metal oxide, though the production took nearly 500 s to reach completion.

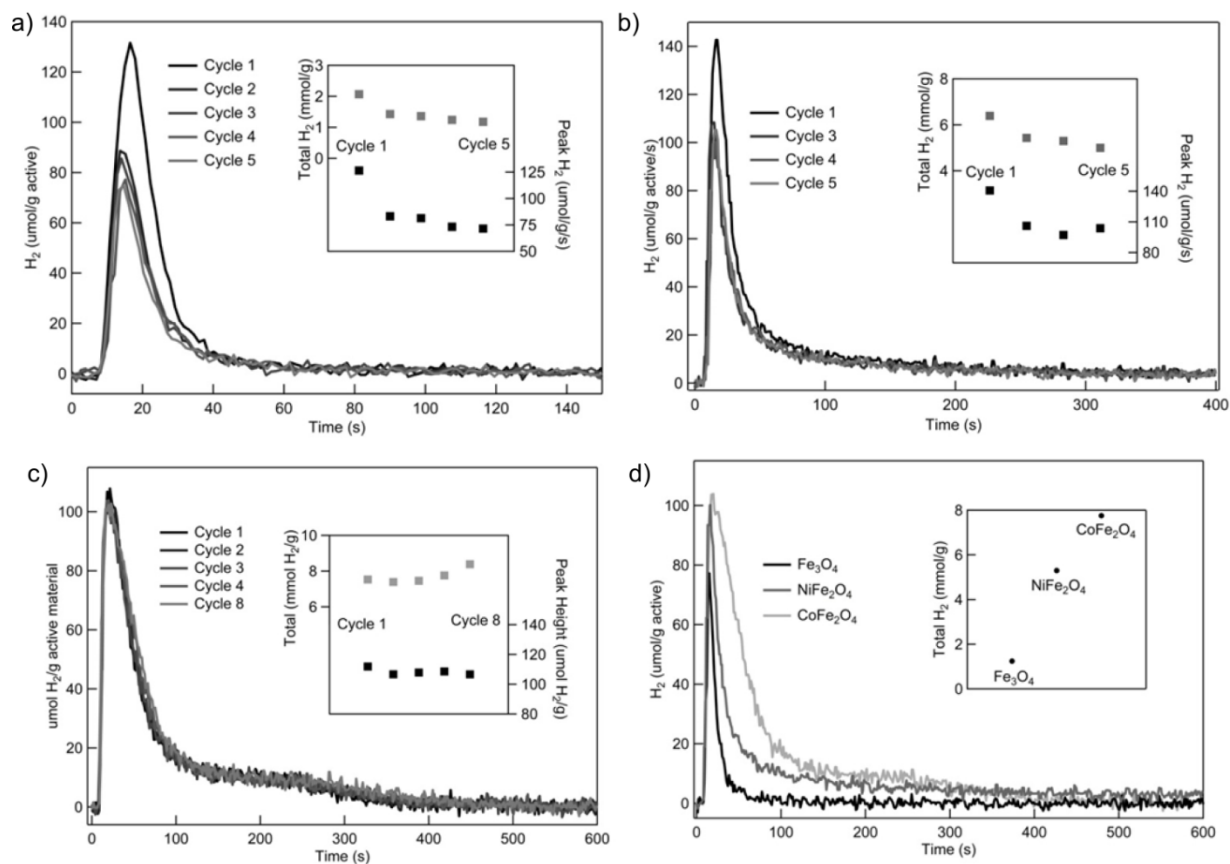


Figure 3.5: a) H₂ production during H₂O oxidation of reduced Fe₃O₄ sample. b) H₂ production during H₂O oxidation cycles of reduced NiFe₂O₄. c) H₂ production during H₂O oxidation cycles of reduced CoFe₂O₄. d) Comparison of Fe₂O₃, NiFe₂O₄, and CoFe₂O₄ samples.

A direct comparison of all the materials (Figure 4 d) shows that both NiFe₂O₄ and CoFe₂O₄ offer significant improvements over conventional Fe₃O₄ in total H₂ production and peak rate of H₂ production. Greater H₂ production from CoFe₂O₄ in comparison to Fe₃O₄ was attributed to the ability of the Co²⁺ ion to reduce to a metallic state under conditions where the Fe³⁺ ion reduced no further than Fe²⁺. [4] Metallic Co and Fe are generated from CoFe₂O₄ during reduction conditions that form FeO from a Fe₃O₄ sample, as identified using in-situ XRD. The cycling conditions in the present study use the same gas composition as the previously mentioned study, thus the reduction products are assumed analogous to those seen by Scheffe, et

al. Reduction to a metallic state, rather than to the FeO state, accounts for the increased H₂ production of both mixed metal spinels in comparison to the Fe-only sample.

3.4.5 Characterization of Cycled Materials

Surface areas after cycling, shown in Table 3.3, indicate surface area loss for each sample. To distinguish between the effects of the surface area loss of the substrate and the surface area loss of the metal oxide, blank ZrO₂ substrate was cycled at 873 K and subsequently analyzed. The surface area of the substrate was unchanged; therefore, surface area loss during cycling was attributed to the metal oxide, most likely due to sintering and agglomeration of the metal oxide particles. Visual examination of the sample with TEM after reduction showed an increase in the metal oxide agglomerate size to a few hundred nm.

Sample	Surface area before cycling (m ² /g)	Surface Area after cycling (m ² /g)	Change in surface area (m ² /g)
m-ZrO ₂	49 ± 2	49 ± 2	-
Fe ₂ O ₃	35 ± 2	24 ± 2	-11
CoFe ₂ O ₄	33 ± 2	23 ± 2	-10
NiFe ₂ O ₄	39 ± 2	17 ± 2	-22

Table 3.3: Comparison between initial sample surface area and ample surface area after cycling

Examination of the material surface with SEM analysis showed no observable difference between cycled and uncycled materials, and EDS analysis of cycled materials showed homogeneous dispersion of the Co, Ni, and Fe, as was seen in the initial EDS analysis. The absence of distinct zones of ZrO₂ and metal cations, combined with the Raman data showing the presence of the CoFe₂O₄ and NiFe₂O₄ phases, was evidence that phase segregation did not occur during reduction and oxidation cycling.

3.3.6 Effect of H₂O Concentration and Temperature on Oxidation

To establish the limits of cyclability for these CoFe₂O₄ and NiFe₂O₄, samples were cycled under different H₂O concentrations and at different temperatures. As shown in Figure 3.5, data show a clear relationship between H₂O concentration and the peak rate of H₂ production, indicating that the process limiting the kinetic rate of oxidation for these materials has a dependence on H₂O concentration. Oxidation data at different temperatures indicate a clear relationship between reaction temperature and oxidation rate, as expected in any solid-gas reaction due to the increased rate at which solid state processes occur at higher temperatures. [26] These two factors will be investigated in more detail in Chapter 6. The reaction temperature also affected the total H₂ production. This total difference in H₂ was hypothesized to be due to a combination of two factors: different reduction extents resulting from reduction at different temperatures, and incomplete oxidation due to slower kinetic processes at lower temperatures. Materials proved to be cycleable between the temperatures of 773 K and 873 K; however, at temperatures above 873 K material degradation was observed for all samples. Blank ZrO₂ supports cycled at 1073 K showed a decrease in surface area from 49 m²/g to 37 m²/g, indicating substrate instability at high temperatures. The remainder of studies in this thesis were conducted between 773 K and 873 K to preserve the cyclability of the metal oxides.

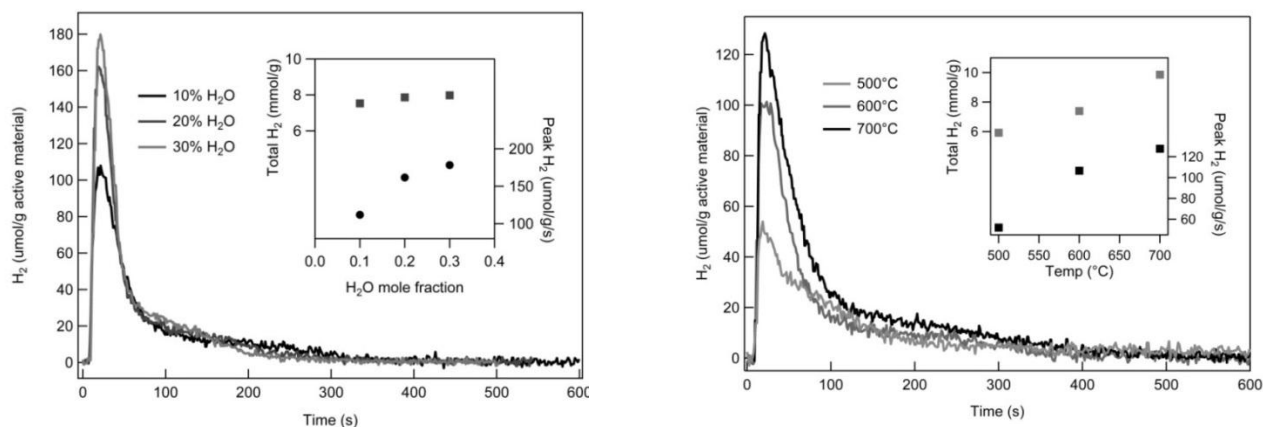


Figure 3.6: Effect of H₂O concentration and temperature on CoFe₂O₄ H₂ production.

3.4 Conclusions

This investigation showed the regeneration of CoFe₂O₄ and NiFe₂O₄ from reduced material solely through H₂O oxidation. Additionally, the reduced material was highly reactive with H₂O, producing H₂ with peak rates near or greater than that of Fe-only materials. The mixed metal spinels showed cycle stability, and the regeneration of the mixed metal spinel was confirmed after several cycles. The substrate m-ZrO₂ was identified as a non-reactive and stable platform for deposition of the mixed metal ferrites. Materials prepared using incipient wetness showed no interactions with the ZrO₂ substrate as only m-ZrO₂ was detected at the surface and in the material bulk. Sample surface areas decrease with cycling, most likely due to the observed sintering and agglomeration of the metal oxide. No metal cation segregation was detected with SEM EDS analysis, though the resolution of this technique is on the order of 1 μm. The detection of the mixed metal spinel phase with Raman analysis after cycling supports the conclusion that no significant phase segregation was occurring in the materials. Based on the results from this analysis, a comprehensive kinetic study investigating the oxidation of these materials should incorporate their response to both temperature and H₂O concentration.

3.5 References

- [1] Gupta P, Velazquez-Vargas L, Fan L. Syngas Redox (SGR) Process to Produce Hydrogen from Coal Derived Syngas. *Energy Fuels*. 2007;21:2900-8.
- [2] Solunke R, Vesper G. Hydrogen Production via Chemical Looping Steam Reforming in a Periodically Operated Fixed-Bed Reactor. *Ind Eng Chem Res*. 2010;49:11037-44.
- [3] Svoboda K, Siewiorek A, Baxter D, Rogut J, Pohorely M. Thermodynamic possibilities and constraints for pure hydrogen production by a nickel and cobalt-based chemical looping process at lower temperatures. *Energy Convers Manage*. 2008;49:221-31.
- [4] Scheffe JR, Allendorf MD, Coker EN, Jacobs BW, McDaniel AH, Weimer AW. Hydrogen Production via Chemical Looping Redox Cycles Using Atomic Layer Deposition-Synthesized Iron Oxide and Cobalt Ferrites. *Chem Mater* 2011;23:2030-8.
- [5] Fan L. *Chemical Looping Systems for Fossil Energy Conversion*. Hoboken, NJ: John Wiley & Sons, Inc.; 2010.
- [6] Mattisson T, Johansson M, Lyngfelt A. Multicycle Reduction and Oxidation of Different Types of Iron Oxide Particles - Application to Chemical-Looping Combustion. *Energy & Fuels*. 2004;18.
- [7] Graves P, Johnston C, Campaniello J. Raman Scattering in Spinel Structure Ferrites. *Mater Res Bull*. 1988;23:1651-60.
- [8] Sickafus KE, Wills JM, Grimes NW. Structure of Spinel. *Journal of the American Ceramic Society*. 1999;82:3279-92.
- [9] Hosterman BD. *Raman Spectroscopic Study of Solid Solution Spinel Oxides*. Las Vegas: University of Nevada; 2011.
- [10] Shebanova ON, Lazor P. Raman spectroscopic study of magnetite (Fe₃O₄): a new assignment for the vibrational spectrum. *Journal of Solid State Chemistry*. 2003;174:424-30.
- [11] Liao YY, Li YW, Hu XG, Chu JH. Temperature dependent phonon Raman scattering of highly a-axis oriented CoFe₂O₄ inverse spinel ferromagnetic films grown by pulsed laser deposition *Applied Physics Letters*. 2012;100:071905.

- [12] Bahlawane N, Ngamou PHT, Vannier V, Kottke T, Heberle J, Kohse-Hoinghaus K. Tailoring the properties and the reactivity of the spinel cobalt oxide. *Physical Chemistry Chemical Physics*. 2009;11:9224-32.
- [13] Laguna-Bercero MA, Sanjuán ML, Merino RI. Raman spectroscopic study of cation disorder in poly- and single crystals of the nickel aluminate spinel *Journal of Physics: Condensed Matter*. 2007;19:186217.
- [14] Chandramohan P, Srinivasan MP, Velmurugan S, Narasimhan SV. Cation distribution and particle size effect on Raman spectrum of CoFe_2O_4 . *Journal of Solid State Chemistry*. 2011;184:89-96.
- [15] Gasparov LV, Tanner DB, Romero DB, Berger H, Margaritondo G, Forró L. Infrared and Raman studies of the Verwey transition in magnetite. *Physical Review B*. 62: 7939-44.
- [16] Ayyappan S, Mahadevan S, Chandramohan P, Srinivasan MP, Philip J, Raj B. Influence of Co^{2+} Ion Concentration on the Size, Magnetic Properties, and Purity of CoFe_2O_4 Spinel Ferrite Nanoparticles. *The Journal of Physical Chemistry C*. 2010;114:6334-41.
- [17] Kim JH, Hwang IS. Development of an in situ Raman spectroscopic system for surface oxide films on metals and alloys in high temperature water. *Nuclear Engineering and Design*. 2005;235:1029-40.
- [18] Graves PR, Johnston C, Campaniello JJ. Raman scattering in spinel structure ferrites. *Materials Research Bulletin*. 1988;23:1651-60.
- [19] Faria DLAd, Silva SV, Oliveira MTd. Raman Microspectroscopy of Some Iron Oxides and Oxyhydroxides. *Journal of Raman Spectroscopy*. 1997;28:873-8.
- [20] Chamritski I, Burns G. Infrared- and Raman-Active Phonons of Magnetite, Maghemite, and Hematite: A Computer Simulation and Spectroscopic Study. *The Journal of Physical Chemistry B*. 2005;109:4965-8.
- [21] Nkosi SS, Yalisi B, Motaung DE, Kwartland J, Sideras-Haddad E, Forbes A, et al. Antiferromagnetic-paramagnetic state transition of NiO synthesized by pulsed laser deposition. *Applied Surface Science*. 2013;265:860-4.

- [22] Li Z, Little R, Dervishi E, Saini V, Xu Y, Biris AR, et al. Micro-Raman spectroscopy analysis of catalyst morphology for carbon nanotubes synthesis. *Chemical Physics*. 2008;353:25-31.
- [23] Davison S, Kershaw R, Dwight K, Wold A. Preparation and characterization of cubic ZrO₂ stabilized by Fe(III) and Fe(II). *Journal of Solid State Chemistry*. 1988;73:47-51.
- [24] Wu P, Kershaw R, Dwight K, Wold A. PREPARATION AND CHARACTERIZATION OF Co(II)/ZrO₂ SOLID SOLUTION. *Mat Res Bull*. 198;23:475-80.
- [25] Stefanic G, Music S, Popovic S, Nomurac K. A study of the ZrO₂-Fe₂O₃ system by XRD, ⁵⁷Fe Mossbauer and vibrational spectroscopies. *Journal of Molecular Structure*. 1999;480-481:627-31.
- [26] Galwey AK. Is the science of thermal analysis kinetics based on solid foundations?: A literature appraisal. *Thermochimica Acta*. 2004;413:139-83.

Chapter 4: Novel Mixed Metal Ferrites for H₂ Production through Chemical Looping

4.1 Abstract

The mixed metal ferrites NiFe₂O₄ and CoFe₂O₄ are candidate materials for the Chemical Looping Hydrogen (CLH) process, which produces pure and separate streams of H₂ and CO₂ without the use of complicated and expensive separation equipment. In the CLH process, syngas reduces a metal oxide, oxidizing the H₂ and CO in the syngas to H₂O and CO₂, and stores the chemical energy of the syngas in the reduced metal oxide. The reduced metal oxide is then oxidized in steam to regenerate the original metal oxide and produce H₂. In this study, we report thermodynamic modeling and experimental results regarding the syngas reduction and H₂O oxidation of NiFe₂O₄ and CoFe₂O₄ to determine the feasibility of their use in the CLH process. Modeling predicts the oxidation of nearly all the CO and H₂ in syngas to H₂O and CO₂ during the reduction step for both materials, and regeneration of the mixed metal spinel phase during oxidation with excess H₂O. Laboratory tests in a packed bed reactor confirmed over 99% conversion of H₂ and CO to H₂O and CO₂ during reduction of NiFe₂O₄ and CoFe₂O₄. Powder XRD analysis of the reduced materials showed, in accordance with thermodynamic predictions, the presence of a spinel phase and a metallic phase. High reactivity of the reduced NiFe₂O₄ and CoFe₂O₄ with H₂O was observed, and XRD analysis confirmed re-oxidation to NiFe₂O₄ and CoFe₂O₄ under the conditions tested. When compared with a conventional Fe-based CLH material, the mixed metal spinels showed a higher extent of reduction under the same conditions, and produced at least four times the H₂ per mass of active material than the Fe-based material. Analysis of the H₂ and CO consumed in the reduction, and the H₂ produced during the oxidation, showed over 90% conversion of the H₂ and CO in syngas back to H₂ during oxidation.

4.2 Introduction

In addition to being a possible future energy source for electricity and vehicle transportation, hydrogen (H_2) is necessary for ammonia production and oil refining, which nationally use nine million tons of H_2 every year. [1] Current methods of H_2 production, including steam methane reforming, partial oxidation of hydrocarbons, and coal gasification, require use of the water-gas shift reaction (Eq. 4.1) to produce a mixture of H_2 and CO_2 from the synthesis gas (syngas) that they generate.



The reaction in Eq. 1 is thermodynamically limited at high temperatures and kinetically limited at low temperatures. Consequently, a two stage process is required to maximize the amount of H_2 in the syngas. Supplementary purification is then necessary to decrease the amount of CO in the gas stream to the desired level. [2, 3] Additionally, the CO_2 must be separated from the H_2 in the product stream using processes such as Pressure Swing Adsorption (PSA) or Monoethanolamine (MEA) scrubbing, which carry high energy penalties and can result in the loss of up to 30% of the produced H_2 . [4, 5] Generation of a pure and easily sequestered CO_2 waste stream is important, as pressure is increasing on industries to curtail the release of CO_2 into the atmosphere.

The Chemical Looping Hydrogen (CLH) production process is an effective alternative method for generation of pure H_2 and a separate stream of pure and easily sequestered CO_2 from any syngas.[2, 6, 7] In the CLH process, syngas reduces a metal oxide material at moderate to high temperatures (500°C to 800°C) as it leaves a gasifier (Eq. 4.2-3). The reduced metal oxide can then be oxidized using steam to produce H_2 and regenerate its original oxide form (Eq. 4.4).



Pure and separate H₂ and CO₂ are produced without complicated or expensive multistep separation processes.

In order to be a viable material for the CLH process, a metal oxide must meet the following criteria:

- 1) Thermodynamically, the reaction of the metal oxide with the syngas must be able to convert almost all of the CO and H₂ in the syngas to CO₂ and H₂O.
- 2) The reduced form of the metal oxide must be readily oxidized using steam.
- 3) The material must demonstrate fast and stable kinetics over a large number of redox cycles.

[7] The first two criteria are intrinsic properties of the metal oxide, and can be altered by changing or doping the metal oxide in use with additional metallic constituents. The third criterion, often a property of the material synthesis method, has been studied and demonstrated at length. [7-9]

Of the potential CLH metal oxide candidates, iron (Fe) remains the most studied due to its abundance, low cost, low toxicity, and overall favorable thermodynamics. [2, 7, 9] When compared thermodynamically to specific oxides of Ni, Cd, Cu, Co, Cr, Mn, and Sn, Fe₂O₃ showed the most promising theoretical maximum conversion of CO and H₂ to CO₂ and H₂O.

Furthermore, the oxidation of FeO and Fe to Fe₃O₄ has a high conversion of H₂O to H₂. [7, 10, 11] Consequently, the most common CLH process to date is expressed by the following reactions:



The O₂ oxidation (Eq. 7) is necessary because Fe₃O₄ is unable to split water to regenerate Fe₂O₃. Unlike Fe₂O₃, Fe₃O₄ is thermodynamically unable to oxidize much of the CO and H₂ in syngas to CO₂ and H₂O, which leaves a significant portion of un-reacted CO and H₂ in the syngas exiting the reactor. Experimentally, this is observed as immediate CO and H₂ breakthrough when testing a packed bed of Fe₃O₄ particles. [2] Therefore, the Fe₂O₃ phase must be regenerated with O₂ before the reduction step. [7, 11, 12] The H₂ and CO used to reduce the Fe₂O₃ to Fe₃O₄ is not recovered as H₂, which results in a loss of potential H₂ production. Regardless of the associated H₂ loss, the O₂ oxidation is exothermic and produces a significant amount of heat, which is used to generate electricity and heat process streams. [7]

In addition to Fe₂O₃/Fe₃O₄, the mixed metal spinels NiFe₂O₄ and CoFe₂O₄ have been suggested as possible CLH materials. [10] These spinels have the composition AB₂O₄, where A is an M²⁺ ion and B is an M³⁺ ion. [13] The spinel Fe₃O₄ contains one Fe²⁺ ion for every two Fe³⁺ ions. In the mixed metal spinels NiFe₂O₄ and CoFe₂O₄, the Ni and Co possess a 2+ charge while all the Fe ions exist in the 3+ oxidation state. Thermodynamic studies conducted between 127°C and 727°C predict a higher conversion of H₂ to H₂O and CO to CO₂ during the reduction

of mixed metal spinels containing Fe and Ni or Fe and Co than are attainable with Fe_3O_4 . Predictions show the mixed metal ferrite will regenerate during H_2O oxidation, unlike Fe_2O_3 . [10] The referenced study [10] regards the mixed metal spinels with caution due to the hypothesis that the metal oxides Fe_3O_4 , CoO , and NiO would segregate upon cycling rather than regenerate the mixed metal spinel phase. Oxidation to NiFe_2O_4 or CoFe_2O_4 , rather than $\text{NiO}/\text{Fe}_3\text{O}_4$ or $\text{CoO}/\text{Fe}_3\text{O}_4$, increases the oxidation H_2 yield by 8% if the starting composition is a stoichiometric mixture of 2:1 Fe:Ni or 2:1 Fe:Co in their metal states. This additional H_2 production comes from the further oxidation of Fe^{2+} ions to Fe^{3+} ions in the mixed metal spinel.

In a recent study of the reduction and subsequent water oxidation of CoFe_2O_4 and Fe_3O_4 films deposited on high surface area substrates using atomic layer deposition (ALD), CoFe_2O_4 produced twice the amount of H_2 as the Fe_3O_4 under the same cycling conditions, and maintained excellent cyclability for up to the seven cycles tested. [14] Additional H_2 production was attributed to the ability of the Co^{2+} to cycle between the metallic state and the +2 oxidation state under the conditions tested. Though successfully demonstrating that the mixed metal ferrites can have beneficial cycling properties, this investigation did not confirm CoFe_2O_4 as the product of the oxidation and did not consider the limits of H_2 and CO conversion during the reduction step of the cycle. No such data have been reported for NiFe_2O_4 .

The present study seeks to investigate the feasibility of utilizing mixed metal spinels, specifically NiFe_2O_4 and CoFe_2O_4 , in the CLH process. The ability of these materials to convert CO and H_2 to CO_2 and H_2O during the reduction step and the reactivity of the reduced materials with water to produce H_2 were examined using thermodynamic databases in the FactSage program, then experimentally investigated and compared with the properties of Fe-based materials. While conventional CLH processes are focused on Fe_2O_3 to produce H_2 , CO_2 , and

heat, this mixed metal ferrite-based process is focused on maximizing the amount of H₂ produced, with H₂ production demonstrated at four times that of the conventional Fe₂O₃ processes under operating conditions.

4.3 Materials and Experimental Methods

4.3.1 Thermodynamic Analysis

Thermodynamic calculations were performed using the FactSage™ program (Version 6.2), which uses Gibbs free energy minimization calculations and extensive thermodynamic property databases for thermodynamic modeling. Multiple studies show the FactSage program correctly models the phase and composition of mixed metal spinels during thermal reduction and H₂O oxidation. [15, 16] Including solution phases from the FactSage oxide solution database (version 5.3) in thermodynamic calculations, rather than only stoichiometric line compounds, significantly affects the accuracy of the thermodynamic calculations. [15] FactSage is able to reproduce thermodynamic properties, activities, M²⁺/M³⁺ ratios, solution sublattice cation distributions, and partial pressures of equilibrium gases from compiled experimental data using these databases. [17]

In addition to pure solids and gases from the Fact 5.3 database, spinel and metal oxide solution phases were included for this study and are shown in Table 1. The FactSage spinel solution phase uses the compound energy formalism model to describe the distribution of cations over spinel tetrahedral and octahedral sites. Vacancies in the octahedral sublattice allow oxygen non-stoichiometry and deviations from the ideal 2+/3+ cation ratio in the spinel phase model (Fe²⁺, Fe³⁺, M²⁺, M³⁺)_T[Fe²⁺, Fe³⁺, M²⁺, M³⁺, Va]₂O₄. [18] The metal oxide solution phase is modeled as a random solution of M⁺², Fe⁺², and Fe⁺³ ions on cation sites. Vacancies associated with Fe⁺³ ions on cation sites allow for excess Fe cations in the wustite (Fe_{1-x}O) phase. [15, 19]

These models have been optimized over the temperatures and compositions examined in this chapter. [17, 20]

<u>Solution Species</u>		
Spinel		
[Co(II),Co(III),Fe(II),Fe(III)]		
[Co(II),Co(III),Fe(II),Fe(III),Vacancy] ₂ O ₄ /		
[Ni(II), Fe(II),Fe(III)]		
[Ni(II), Fe(II),Fe(III),Vacancy] ₂ O ₄		
MeO (Me=Co/Ni)		
Fe _x O, MeO		
Fe ₂ O ₃		
<u>Gases</u>		<u>Compounds</u>
H ₂ O	CO ₂	Ni/Co
H ₂	CO	Fe
O ₂	Fe	Fe ₂ O ₃
O	Ni/Co	

Table 4.1: Compounds, gases and solution species considered in thermodynamic calculations using FactSage.

As in previous literature, the H₂/H₂O and CO/CO₂ systems were considered independently in calculations. [7, 21-23] The activity of the reducing gas, held constant, defined the activity of the oxidizing gas. These model conditions simulate the continuous flow of a constant composition syngas over the metal oxide, such that the gaseous reaction products do not inhibit forward reactions. This allowed the calculation of predicted solid products in the limiting case of excess gaseous reactants. Gases involved behave as ideal gases at both the reference temperature and the evaluated temperature, so gas pressures are reported instead of gas activities. [7, 11, 24, 25]

4.3.2 Ferrite Sample Preparation

Samples of Fe₂O₃, NiFe₂O₄, and CoFe₂O₄ were prepared via the incipient wetness method. [26, 27] Iron nitrate (Fe(NO₃)₃ · 9H₂O, Sigma Aldrich, 98%), nickel nitrate (Ni(NO₃)₂ · 6H₂O, Alfa Aesar, 98%), and cobalt nitrate (Co(NO₃)₂ · 6H₂O, Alfa Aesar, 98%) were

dissolved in de-ionized water to form 2 molar aqueous solutions of metal cations. Catalyst pellets made of approximately 20 nm sintered ZrO₂ spheres (Alfa Aesar, 99%, 0.31 cc/g, 50 m²/g), were crushed and sieved to 110 – 175 μm diameter particle size and subsequently mixed with the aqueous metal nitrate solutions of the desired stoichiometry. Solution volumes equal to the calculated pore volume of the ZrO₂ samples were added using a calibrated pipette. Samples were dried at 60°C in a vacuum oven for eight hours after each addition of the nitrate solution. When the desired mass percent of metal oxide (30%) was reached, the samples were calcined at 600°C in air for eight hours.

4.3.3 Material Characterization

Sample mass loadings and deposited cation ratios were confirmed via inductively coupled plasma-atomic emission spectroscopy (ICP-AES). Phase identification was performed using X-Ray diffraction (XRD, Scintag PAD5 Powder Diffractometer, CuKα1 radiation, λ=1.5406 Å, scan rate 0.5°/min, step size 0.02°). Surface areas were measured using Brunauer-Emmett-Teller (BET) surface area analysis, and crushed samples were examined visually using a Philips CM 100 Transmission Electron Microscope.

4.3.4 Chemical Cycling

Selected test samples were used to form a packed bed in a 0.64 cm OD/0.32 cm ID (0.25” OD/0.125” ID) Al₂O₃ tube, as shown in Figure 4.1. A metal filter gasket in a 0.32 cm (0.25”) ID ultra-torr fitting was secured at one end of the tube, which was subsequently filled to the center with 0.16 cm (0.0625”) diameter ZrO₂ spheres. Approximately 600 mg of sample material was placed in the tube on top of the ZrO₂ spheres to form a bed of active material. A small piece of

ZrO₂ felt (Zircar Zirconia) between the spheres and the sample ensured the sample placement at the center of the bed. A second piece of ZrO₂ felt at the opposite end of the sample ensured sample packing. The tube was placed in a horizontal furnace constructed using a 1.27 cm OD/0.95 cm ID (0.5" OD/0.375" ID) Al₂O₃ tube wrapped in nichrome wire secured using a high temperature ceramic epoxy and wrapped in insulation. An Omega CNi16 process controller module was used to control the temperature of the reactor, which was monitored using a thermocouple placed between the furnace tube and the Al₂O₃ reactor tube.

Calibrated MKS 1179A mass flow controllers delivered gases to the system. A New Era NE-1000 syringe pump delivered water to heated coils and a stream of Ar carrier gas to generate steam for the oxidation step. A constant stream of Ar purged the reactor before and after delivery of reactant gases. The reducing syngas mixture and oxidizing steam mixture equilibrated on a separate pressure controlled reactor bypass line for fifteen minutes prior to introduction contact with the sample. Upon completion of each reaction step, the Ar purge immediately resumed. A column of drierite removed H₂O from the gas stream before the mass spectrometer. Pressure controllers and a vacuum pump maintained a constant pressure on the bypass and reactor lines, and the bypass line pressure controller monitored the upstream pressure during the reactions.

A downstream absolute pressure of 81.3 ± 0.03 kPa (610 ± 0.2 Torr set point) was maintained during reduction and oxidation of the sample. A flowrate of 24 sccm of syngas and steam in Ar created a 13 - 20 kPa (100 - 150 Torr) pressure drop across the reactor. Syngas was composed of 8.7% H₂, 8.7% CO, 13% CO₂, in Ar, a composition appropriate for reducing Fe₂O₃ to FeO. [14] Reduction to FeO rather than to Fe metal mitigates the degradation of the material cyclability and the deposition of carbon. [6] Reduction and oxidation reactions were performed

at a furnace temperature of 873 ± 1.5 K. Steam production occurred at 110°C by injecting 0.002 mL/min or 0.006 mL/min of H_2O into 20 sccm of Ar in heated coils. The resulting mixture was estimated to be 10% and 30% steam in Ar, respectively. All gas lines were maintained at a temperature of 993 K to avoid condensation of H_2O before the drierite column. Oxidations continued until H_2 levels returned to their baseline as measured before reaction.

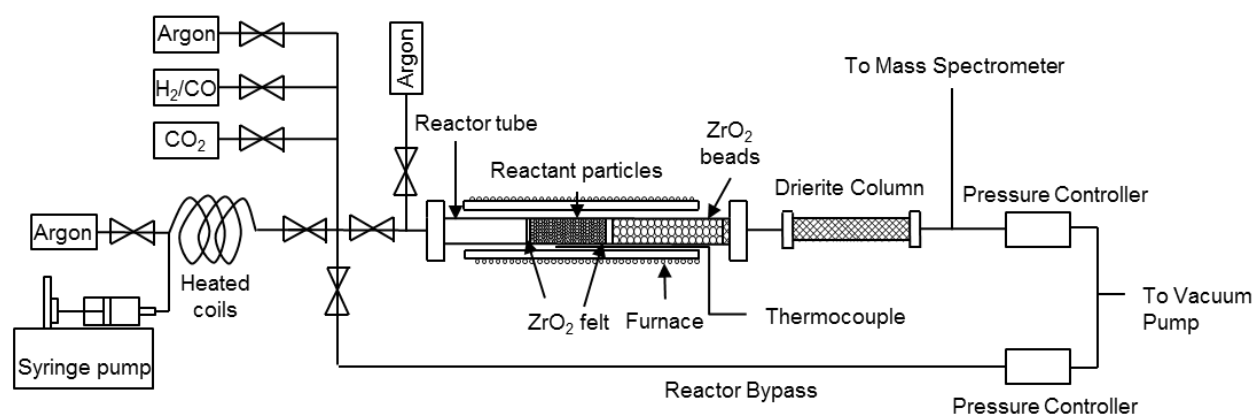


Figure 4.1: Reactor system used for chemical reduction and H_2O oxidation.

4.3.5 Gas Analysis

A Stanford Research Systems QMS 200 mass spectrometer monitored reaction products in each experiment. In some experiments a California Analytic Instruments non-dispersive infrared detector (NDIR) obtained secondary data for the CO and CO_2 concentrations during reaction. For NDIR analysis, 475 sccm of Ar diluted the reaction product stream after the drierite column and mass spectrometer capillary port to meet the flow minimum of 500 sccm required for instrument operation. Five point calibrations, performed each day for H_2 , CO, and CO_2 with each instrument used, covered the gas parts-per-million (ppm) ranges observed in reactor operation. The mass spectrometer had a detection limit of 3000 ppm for CO and CO_2 , and 500 ppm for H_2 . The NDIR had a detection limit of 600 ppm for both CO and CO_2 .

4.4 Results and Discussion

4.4.1 Thermodynamic modeling

Figure 4.2 a) and b) show the results of the FactSage equilibrium calculations. Plotted are the equilibrium moles of spinel and metal oxide solution phases and the metallic phase as a function of gas compositions, $p_{\text{CO}}/p_{\text{CO}_2}$ and $p_{\text{H}_2}/p_{\text{H}_2\text{O}}$ for NiFe_2O_4 and CoFe_2O_4 . Additionally, the predicted equilibrium cation fractions in the spinel are plotted as a function of gas composition.

Calculations show that NiFe_2O_4 in contact with gases containing $p_{\text{CO}}/p_{\text{CO}_2}$ ratios less than 0.002 and $p_{\text{H}_2}/p_{\text{H}_2\text{O}}$ ratios less than 0.005 show the formation of a small amount of NiO. The amount of Ni in the NiO phase at equilibrium increases with increasing $p_{\text{H}_2}/p_{\text{H}_2\text{O}}$ and $p_{\text{CO}}/p_{\text{CO}_2}$, and reaches a maximum of about 7% of the total Ni content at $p_{\text{CO}}/p_{\text{CO}_2} = 0.0019$ and $p_{\text{H}_2}/p_{\text{H}_2\text{O}} = 0.0049$. At these gas compositions, the Fe cations are predicted to remain in the spinel phase to form an Fe-rich spinel with stoichiometry between NiFe_2O_4 and $\text{Ni}_{0.93}\text{Fe}_{2.07}\text{O}_4$. At $p_{\text{CO}}/p_{\text{CO}_2}$ ratios greater than 0.002, and $p_{\text{H}_2}/p_{\text{H}_2\text{O}}$ ratios greater than 0.005, FactSage calculations show the disappearance of the NiO phase and the formation of a Ni metal phase with the Fe-rich spinel phase. The amount of Ni in the metallic phase increases with increasing $p_{\text{H}_2}/p_{\text{H}_2\text{O}}$ and $p_{\text{CO}}/p_{\text{CO}_2}$ ratios until the Ni in the spinel is exhausted near a $p_{\text{CO}}/p_{\text{CO}_2}$ ratio of 0.8 or a $p_{\text{H}_2}/p_{\text{H}_2\text{O}}$ ratio of 1.5.

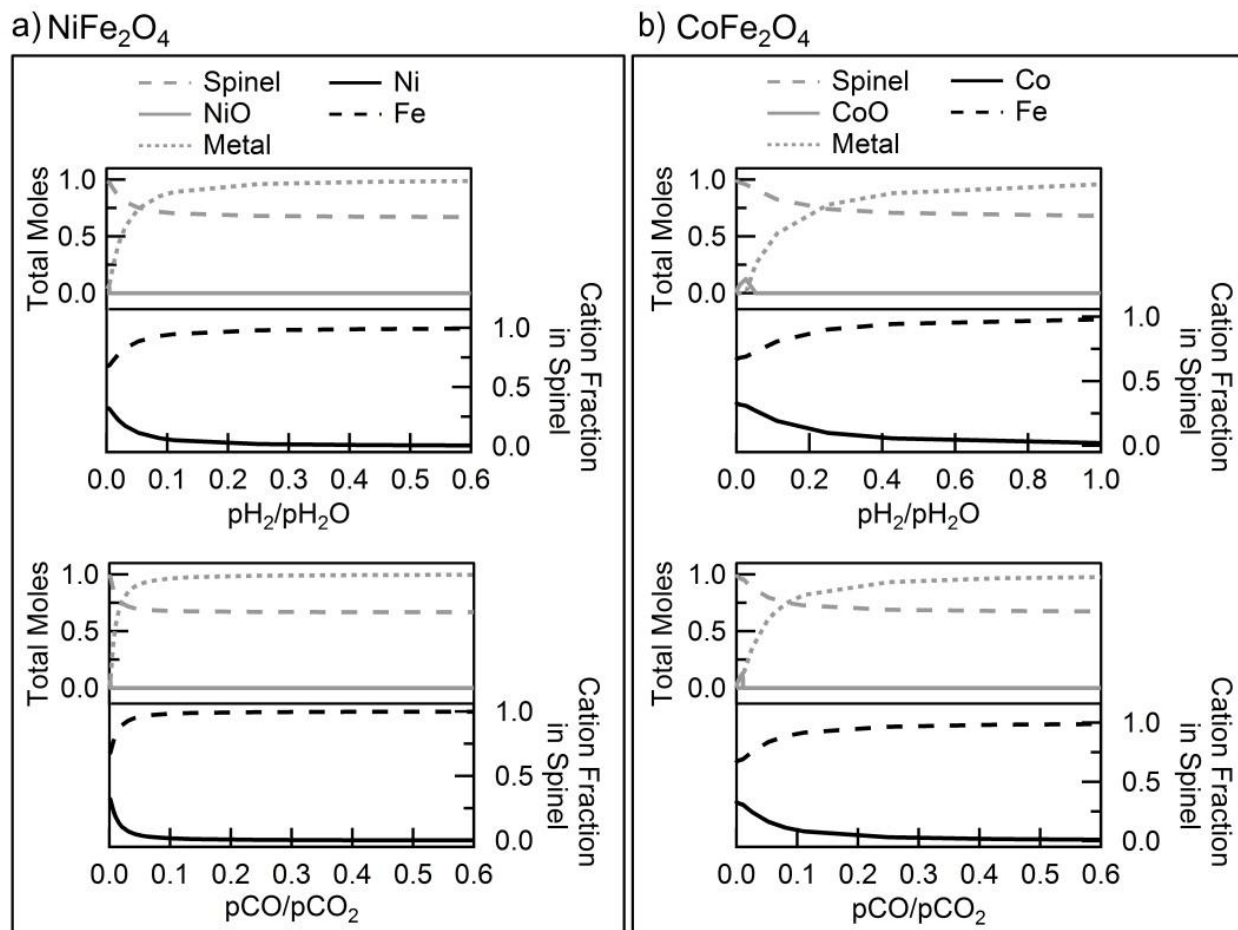


Figure 4.2: FactSage modeling results for the a) NiFe_2O_4 system and b) CoFe_2O_4 system. The total moles of spinel, MeO, and metallic phases, as well as the fraction of each cation in the spinel phase are shown as a function of $p\text{H}_2/p\text{H}_2\text{O}$ and $p\text{CO}/p\text{CO}_2$.

Similarly, CoFe_2O_4 in contact with gases containing $p\text{CO}/p\text{CO}_2$ ratios less than 0.01, and $p\text{H}_2/p\text{H}_2\text{O}$ ratios less than 0.03, forms a CoO phase in equilibrium with an Fe-rich spinel phase. The amount of Co in the CoO phase reaches a maximum of 12% of the total Co, forming a spinel with a composition $\text{Co}_{0.87}\text{Fe}_{2.13}\text{O}_4$. At $p\text{CO}/p\text{CO}_2$ ratios greater than 0.01 and $p\text{H}_2/p\text{H}_2\text{O}$ ratios greater than 0.03, the CoO phase disappears and a Co metal phase appears. The amount of Co in the metal phase increases, but the Fe cations are predicted to remain in the spinel phase until $p\text{CO}/p\text{CO}_2 = 1$ or $p\text{H}_2/p\text{H}_2\text{O} = 1.5$, forming an increasingly Fe-rich spinel.

These calculations show that in both the Co/Fe system and the Ni/Fe system, each composition of spinel is in equilibrium with a unique $p\text{CO}/p\text{CO}_2$ or $p\text{H}_2/p\text{H}_2\text{O}$ ratio, as expressed in Equations 4.8 and 4.9. In a reactor system with sufficiently high kinetic rates, the ratios of $p\text{CO}/p\text{CO}_2$ and $p\text{H}_2/p\text{H}_2\text{O}$ in the syngas exiting a reactor containing fully oxidized NiFe_2O_4 or CoFe_2O_4 could be quite low: less than 0.002. In accord with the equilibrium constants between the gas and solid for each intermediate spinel composition of each material, gradual breakthrough of CO and H_2 would be observed, along with a gradual decrease in produced CO_2 and H_2O . Under the same conditions, CoFe_2O_4 is expected to show H_2 and CO breakthrough at lower material conversions than NiFe_2O_4 due to the higher overall $p\text{H}_2/p\text{H}_2\text{O}$ and $p\text{CO}/p\text{CO}_2$ values at the same $\text{M}_{1-0.75\delta}\text{Fe}_2\text{O}_{4-\delta}$ composition.

In contrast to the mixed metal spinels, equilibrium constants predict that reduction of Fe_3O_4 to FeO occurs when the ratio of $p\text{H}_2/p\text{H}_2\text{O}$ is 2.3 and the ratio of $p\text{CO}/p\text{CO}_2$ is 0.85 (Eq. 4.10a). In a system with sufficiently fast kinetics, syngas in equilibrium with the reduction of Fe_3O_4 to FeO will maintain this composition until complete conversion of Fe_3O_4 to FeO and then change abruptly. Similarly, no intermediates exist between Fe_2O_3 and Fe_3O_4 ; therefore, a sharp change in gas composition is expected at the reactor exit when Fe_2O_3 is exhausted (Eq. 4.10b).

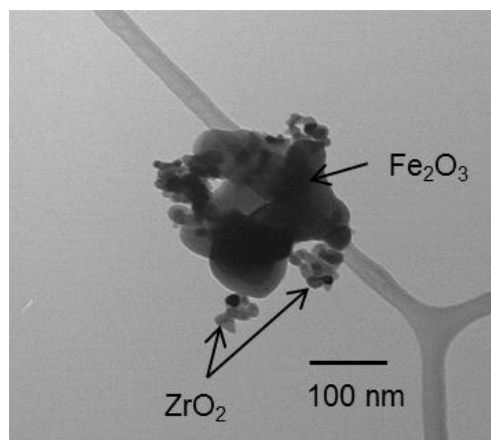
As the spinel compositions shown in Figure 4.2 imply, FactSage predictions show regeneration of NiFe_2O_4 and CoFe_2O_4 with H_2O oxidation; however, an excess of H_2O is necessary. The $\text{H}_2/\text{H}_2\text{O}$ equilibrium constants for Equations 8 and 9 govern the amount of H_2O excess necessary for full oxidation.

<u>Equation:</u>	<u>Conditions:</u>
4.8a $\text{NiFe}_2\text{O}_4 + \text{H}_2 / \text{CO} \leftrightarrow (0.75\delta)\text{NiO} + \text{Ni}_{1-0.75\delta}\text{Fe}_2\text{O}_{4-\delta} + \text{H}_2\text{O} / \text{CO}_2$ $0 \leq \delta \leq 0.093$	$\frac{p\text{CO}}{p\text{CO}_2} = \frac{1}{K_{\text{eq,CO}}} < 0.002, \frac{p\text{H}_2}{p\text{H}_2\text{O}} = \frac{1}{K_{\text{eq,H}_2}} < 0.005$
4.8b $\text{NiFe}_2\text{O}_4 + \text{H}_2 / \text{CO} \leftrightarrow (0.75\delta)\text{Ni} + \text{Ni}_{1-0.75\delta}\text{Fe}_2\text{O}_{4-\delta} + \text{H}_2\text{O} / \text{CO}_2$ $0.093 \leq \delta \leq 1.33$	$0.002 < \frac{p\text{CO}}{p\text{CO}_2} = \frac{1}{K_{\text{eq,CO}}} < 0.8, 0.005 < \frac{p\text{H}_2}{p\text{H}_2\text{O}} = \frac{1}{K_{\text{eq,H}_2}} < 1.5$
4.9a $\text{CoFe}_2\text{O}_4 + \text{H}_2 / \text{CO} \leftrightarrow (0.75\delta)\text{CoO} + \text{Co}_{1-0.75\delta}\text{Fe}_2\text{O}_{4-\delta} + \text{H}_2\text{O} / \text{CO}_2$ $0 \leq \delta \leq 0.16$	$\frac{p\text{CO}}{p\text{CO}_2} = \frac{1}{K_{\text{eq,CO}}} < 0.01, \frac{p\text{H}_2}{p\text{H}_2\text{O}} = \frac{1}{K_{\text{eq,H}_2}} < 0.03$
4.9b $\text{CoFe}_2\text{O}_4 + \text{H}_2 / \text{CO} \leftrightarrow (0.75\delta)\text{Co} + \text{Co}_{1-0.75\delta}\text{Fe}_2\text{O}_{4-\delta} + \text{H}_2\text{O} / \text{CO}_2$ $0.16 \leq \delta \leq 1.33$	$0.01 < \frac{p\text{CO}}{p\text{CO}_2} = \frac{1}{K_{\text{eq,CO}}} < 1, 0.03 < \frac{p\text{H}_2}{p\text{H}_2\text{O}} = \frac{1}{K_{\text{eq,H}_2}} < 1.5$
4.10a $\text{Fe}_3\text{O}_4 + \text{H}_2 / \text{CO} \leftrightarrow 3\text{FeO} + \text{H}_2\text{O} / \text{CO}_2$	$\frac{p\text{CO}}{p\text{CO}_2} = \frac{1}{K_{\text{eq,CO}}} = 0.85, \frac{p\text{H}_2}{p\text{H}_2\text{O}} = \frac{1}{K_{\text{eq,H}_2}} = 2.3$
4.10b $3\text{Fe}_2\text{O}_3 + \text{H}_2 / \text{CO} \leftrightarrow 2\text{Fe}_3\text{O}_4 + \text{H}_2\text{O} / \text{CO}_2$	$\frac{p\text{CO}}{p\text{CO}_2} = \frac{1}{K_{\text{eq,CO}}} = 0.00001, \frac{p\text{H}_2}{p\text{H}_2\text{O}} = \frac{1}{K_{\text{eq,H}_2}} = 0.00003$

Table 4.2: Chemical equations for spinel reduction as predicted with FactSage. Mixed metal spinels (Eq.4.8, 9) reduce to form a Fe-rich spinel and ultimately a metallic phase. Each spinel composition is in equilibrium with a unique gas composition.

4.4.2 Material Characterization

Sample surface areas and mass percents are listed in Figure 4.3. The surface area of the ZrO_2 substrate was $49 \pm 2 \text{ m}^2/\text{g}$ prior to deposition. Surface areas decreased with the addition of the metal oxide due to both the addition of mass and to pore blocking in the substrate. Mass percents of metal oxide and cation ratios, measured with ICP-AES, were verified to be as calculated from the volumes of nitrate solution used in synthesis. Powder XRD analysis confirmed only the spinel phase and the m- ZrO_2 phase after annealing. Visual inspection of annealed and crushed samples with a TEM, displayed in Figure 3, show 100-200 nm metal oxide agglomerates. Nitrogen Leco analysis confirmed complete removal of nitrogen from the samples during annealing.



<u>Sample</u>	<u>Mass percent of metal oxide</u>	<u>Cation composition</u>	<u>Surface area (m²/g)</u>
Fe ₂ O ₃	30.6%	Only Fe	29
CoFe ₂ O ₄	28.0%	Fe:Co=2.1:1	26
NiFe ₂ O ₄	31.1%	Fe:Ni=1.9:1	36

Figure 4.3: TEM of crushed and annealed incipient wetness prepared sample, surface areas and mass percents for each sample tested.

4.4.3 Reduction Step

Initial experiments using Fe₂O₃ and Fe₃O₄ validated the previously mentioned apparatus and procedures by confirming equivalent results with previous literature, and provided a comparison for the NiFe₂O₄ and CoFe₂O₄. Figures 4.4a and 4.4b show the composition of syngas exiting the reactor during the reduction step as a function of time for samples of Fe₂O₃ and Fe₃O₄. Samples were reduced for a total of fifteen minutes at 873 K. Flow of syngas to the reactor began at t = 0 s, and the gases took 275 s to travel from the mass flow controllers to the mass spectrometer capillary port. For the Fe₂O₃ sample, from t = 275 s to t = 425 s (the region labeled “1” in Figure 4.4a), CO₂ was the only reactant or product gas through the reactor due to the oxidation of CO to CO₂ as CO reduced the metal oxide. The reduction product H₂O, also expected, was removed in the drierite column before the mass spectrometer to prevent condensation in the capillary tube. A sharp breakthrough of CO and H₂ was observed at approximately t = 425 s (the beginning of region 2, Figure 4.4a), signaling that all the Fe₂O₃ had been consumed and converted to Fe₃O₄ or FeO. As discussed, equilibrium constants for the reduction of Fe₂O₃ to Fe₃O₄ are large ($K_{eq,CO} = pCO_2/pCO = 100,000$, $K_{eq,H_2} = pH_2O/pH_2 =$

33,000 at 600°C), which indicates that the reaction can proceed until essentially all H₂ or CO is consumed. [6, 7] Analysis of pre-breakthrough effluent gases (gas composition in region 1, Figure 4.4a) confirmed greater than 99% conversion of H₂ and CO, indicating H₂ levels less than 500 ppm and CO levels less than 650 ppm.

Oxidation of the reduced Fe₂O₃ sample in H₂O formed Fe₃O₄, which was verified using XRD. As expected, upon subsequent reduction, this sample showed immediate simultaneous CO, H₂, and CO₂ breakthrough (beginning of region 1, Figure 4b). In this experiment, the measured pCO₂/pCO ratio was 1.17 and the pH₂O/pH₂ ratio was 0.45 (H₂O values were calculated assuming all H₂ not observed with the mass spectrometer was oxidized to H₂O), which both agree with the theoretical values $K_{eq}(pCO_2/pCO) = 1.2$ and $K_{eq}(pH_2O/pH_2) = 0.43$. A similar equilibrium was observed after breakthrough for the Fe₂O₃ samples. These results for Fe₂O₃ and Fe₃O₄, shown in Figures 4.4a and 4.4b, agree well with previously published literature. [2, 6, 28]

Figure 4.4c and 4.4d shows the composition of syngas exiting the bed as a function of time for samples of NiFe₂O₄ and CoFe₂O₄ during fifteen minute reductions. To ensure the CoFe₂O₄ and NiFe₂O₄ samples were in oxidation states achievable with only steam oxidation, the samples were reduced and subsequently oxidized in steam before these data were collected.

From $t = 275$ s to $t = 625$ s, the NiFe₂O₄ effluent gas contained only CO₂ (region 1, Figure 4.4d). All H₂O was removed in the drierite column. At $t = 625$ s, breakthrough of CO and H₂ was observed and the CO₂ level decreased (region 2, Figure 4.4c). Breakthrough of CO and H₂ occurred simultaneously and increased at nearly identical rates, thus the mass spectrometer traces lie almost directly on top of each other in Figure 4.4c. Gas analysis during

region 1 indicated less than 500 ppm H₂ and 800 ppm CO in the effluent gas, an H₂ and CO conversion greater than 99%.

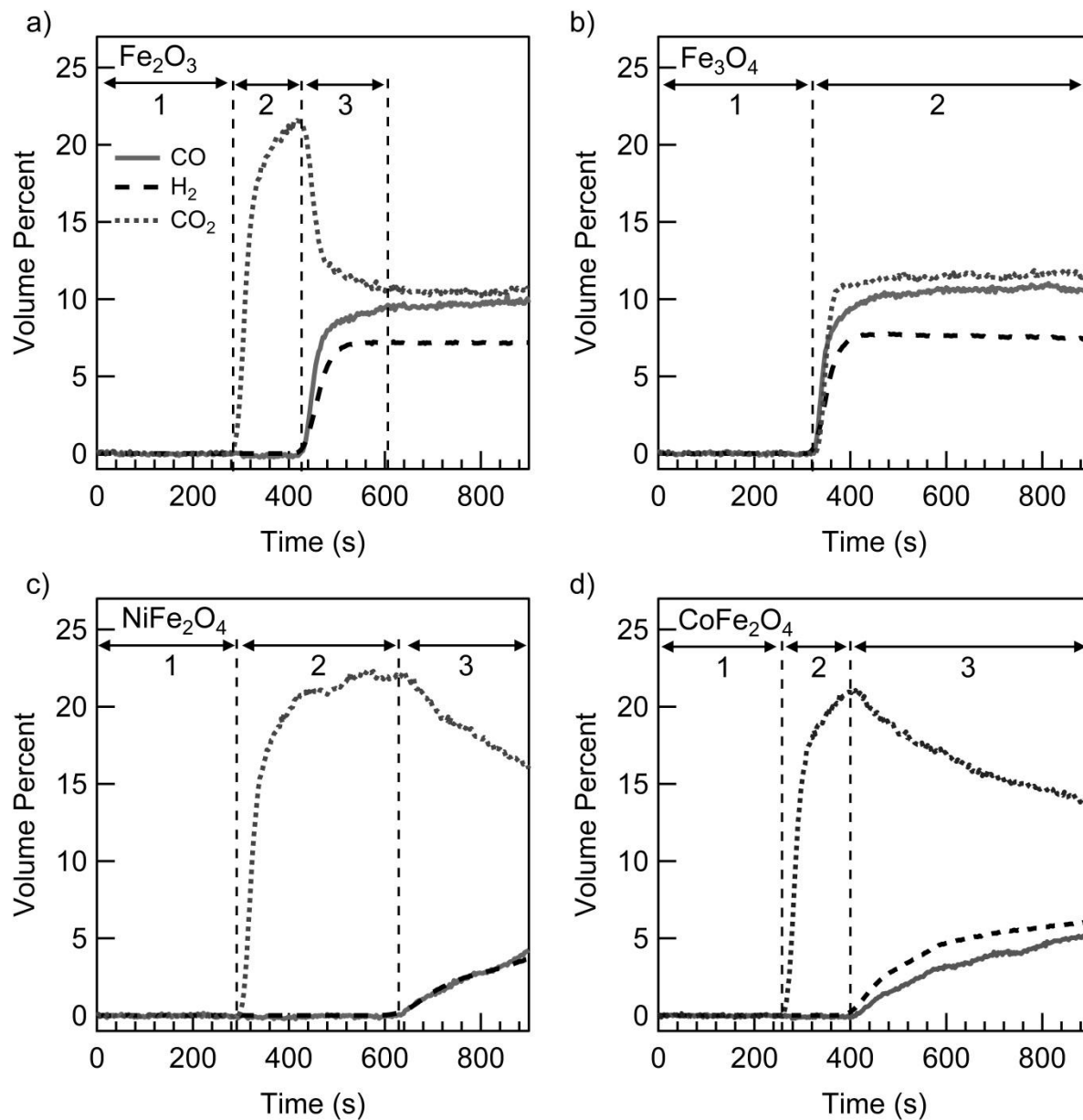


Figure 4.4: Fifteen minute syngas reductions of a) Fe₂O₃, b) Fe₃O₄, c) NiFe₂O₄, and d) CoFe₂O₄.

From $t = 275$ s to $t = 400$ s the CoFe₂O₄ effluent gas contained only CO₂ (region 1, Figure 4.4c). Again, H₂O was expected, but was removed in the drierite column. At $t = 600$ s,

the CO₂ level decreased and breakthrough of CO and H₂ was observed (region 2, Figure 4.4c). Breakthrough of H₂ occurred more rapidly than breakthrough of CO, in accordance with the FactSage predictions discussed in Section 3.1. As with NiFe₂O₄, gas analysis during region 1 during CoFe₂O₃ reduction indicated less than 500 ppm H₂ and 800 ppm CO in the effluent gas, an H₂ and CO conversion greater than 99%.

These data confirm the thermodynamic prediction that fully oxidized NiFe₂O₄ and CoFe₂O₄, like Fe₂O₃, are capable of oxidizing essentially all the H₂ and CO in the syngas to H₂O and CO₂. Unlike the sharp breakthrough of H₂ and CO during Fe₂O₃ reduction, the CO and H₂ breakthroughs were gradual for NiFe₂O₄ and CoFe₂O₄, and H₂ and CO values continued to rise until the end of the reduction. Before the reduction was terminated, the pCO/pCO₂ and pH₂/pH₂O ratios increased to values near 0.2 for both NiFe₂O₄ and CoFe₂O₄. In this gas composition range, FactSage predictions show formation of a Fe-rich spinel and Ni or Co metal. As FactSage predicted, under the same conditions, breakthrough of H₂ and CO were observed earlier for CoFe₂O₄ than for NiFe₂O₄ because of higher overall pH₂/pH₂O and pCO/pCO₂ values at the same M_{1-0.75δ}Fe₂O_{4-δ} composition.

4.4.4 XRD and Raman Analysis

X-ray diffraction spectra of NiFe₂O₄ and CoFe₂O₄ materials after three minutes of reduction, after twelve minutes of reduction, and after complete H₂O oxidation are shown in Figure 4.5a. For these experiments, 0.4 g of previously cycled sample were loaded into the reactor, and the material for XRD analysis was taken from the middle of the bed after the reactor was cooled under a continuous Ar purge.

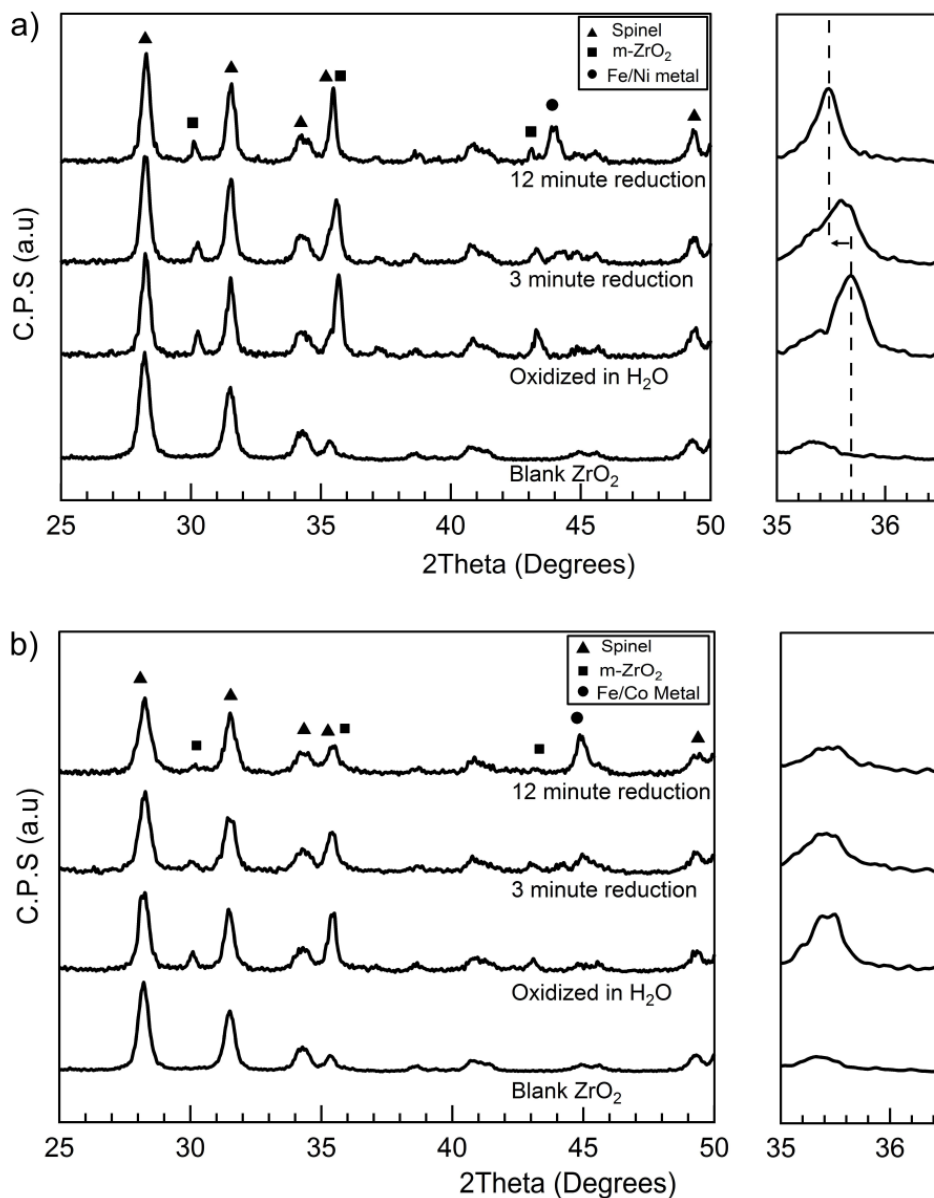


Figure 4.5: XRD data for a) NiFe₂O₄ and b) CoFe₂O₄ samples. The spinel phase is regenerated during H₂O oxidation for each sample, and a metallic phase forms during reduction.

As seen in Figure 4.5a, the H₂O oxidation products for NiFe₂O₄ were the spinel phase and the monoclinic ZrO₂ phase (ICCD-JCPDS 13-0307). The lack of a discernible NiO peaks indicates that the fully oxidized material does not exhibit significant phase segregation, and the

amount of NiO remaining due to equilibrium is negligible or too small to detect with this instrument.

Analysis of reduced NiFe_2O_4 shows that a metallic phase was formed during the three minute reduction, detectable from a reflection near $2\theta = 44^\circ$. This metallic phase grew at the expense of the spinel phase between three and twelve minutes of reaction time for both samples. The XRD patterns for the cubic spinels Fe_3O_4 and NiFe_2O_4 are nearly identical; however, small peak shifts occur in the XRD reflections due to small changes in the spinel lattice constant, a , when a Ni^{2+} is substituted for an Fe^{2+} in the lattice. [29] These differences are slight but evident in the standard spinel (311) lattice plane reflection seen at $2\theta = 35.42^\circ$ for Fe_3O_4 (ICCD-JCPDS #19-0629) and at $2\theta = 35.68^\circ$ for NiFe_2O_4 (ICCD-JCPDS #44-1485). Figure 4.5a shows the (311) peak for the NiFe_2O_4 sample when fully oxidized, after three minutes of reduction, and after twelve minutes of reduction. A peak shift from $2\theta=35.67^\circ$ when fully oxidized to $2\theta=35.48^\circ$ after twelve minutes of reduction is observed, which indicates the expected shift in spinel composition from NiFe_2O_4 to one enriched in Fe. The formation of a metallic phase and an iron-rich spinel phase are evidence that the reduction of these two mixed metal ferrites proceeds as FactSage calculations predict under these conditions. This phenomena has also been observed using Mossbauer spectroscopy in the reduction of a 4:1 Fe:Ni catalyst to form a $\text{Fe}_{3-\psi}\text{Ni}_\psi\text{O}_4$ and a metallic phase. [30] The difference in energy between Ni-O and Fe-O bonds could cause the preferential loss of oxygen from the Ni in the spinel before the Fe rather than equally from both the cations to form an oxygen deficient 2:1 Fe:Ni spinel.

Bond strength in crystals depends on the bond length and the electronegativities of each atom. [31, 32] In NiFe_2O_4 , the Ni^{2+} ion sits in an octahedral site, while the Fe^{3+} occupies both the octahedrally and tetrahedrally coordinated sites. A Ni^{2+} atom has radius of 0.069 nm in the

octahedral spinel position, while the Fe^{3+} ion has a radius of 0.049 nm in the tetrahedral coordination and 0.0645 Å in the octahedral coordination. [33] A greater bond strength would be expected between an Fe cation and an O anion due to the higher charge density on the Fe^{3+} ion. This is consistent with calculations based on density functional theory, which showed that the energy required to form an Fe vacancy is always greater than the energy required to form an Ni vacancy. [34] Oxygen anions bonded with Ni^{2+} cations will be more easily removed by H_2 and CO on the surface, leaving Ni in a reduced state before removing the O bonded to Fe^{3+} in the spinel phase.

A similar argument can be made for the reduction of CoFe_2O_4 , which has also been shown to have a mostly inverse structure. [29] In the inverse structure, an octahedrally coordinated Co^{2+} ion has a radius of 0.072 Å, while the tetrahedrally coordinated Fe^{3+} ions have a radius of 0.049 Å, and octahedrally coordinated Fe^{3+} ions have a radius of 0.065 Å. The resulting charge density is lower for the Co^{2+} ion, and oxygen anions bonded to a Co^{2+} cation will be more easily removed than those bonded to an Fe cation in CoFe_2O_4 . Reduction and in-situ XPS analysis of a mixed Fe-Co spinel at 543 K shows complete reduction of Co at the surface after one hour, while a significant amount of Fe on the surface remains bonded to oxygen anions. After five hours of reduction, only metallic Fe and Co are detectable on the surface. [35] Diffraction data from samples for our study (shown in Figure 4.5b) indicated formation of a metallic phase during the three minute and twelve minute reductions of CoFe_2O_4 . Although an Fe-rich spinel was expected to form, a peak shift was not observed for the CoFe_2O_4 (311) reflection. Since the reflection is at $2\theta = 35.42^\circ$ for Fe_3O_4 (ICCD-JCPDS #19-0629) and $2\theta = 35.44^\circ$ for CoFe_2O_4 (ICCD-JCPDS #22-1086), the diffraction resolution for these materials is

believed to be too poor to capture the expected shift. [36] The H₂O oxidation regenerates the spinel phase, as shown in Figure 4.5b.

Since the data from Raman spectroscopy are not solely reliant on the lattice parameter of the material, but rather on the vibrational modes of the lattice, the Fe₃O₄ and CoFe₂O₄ Raman spectra have different A_{1g}, F_{2g}, and E_g peak positions. [37, 38] The fully oxidized CoFe₂O₄ and the CoFe₂O₄ reduced for three minutes were examined using Raman spectroscopy and compared to known samples shown in Figure 4.6. The peak positions of the A_{1g} and F_{2g}(3) reflections for the fully oxidized material align with those of the CoFe₂O₄ sample. The A_{1g} peak position of the reduced sample shift left, indicating a change in the octahedral divalent cation. [39-41] In CoFe₂O₄, this cation is Co²⁺, while in Fe₃O₄ this cation is Fe²⁺. The peak shift indicates that the material does not retain a 2:1 Fe:Co ratio. The shift towards the Fe₃O₄ peak implies a replacement of the Co²⁺ octahedral cations with Fe²⁺ cations and formation of a Fe-rich spinel.

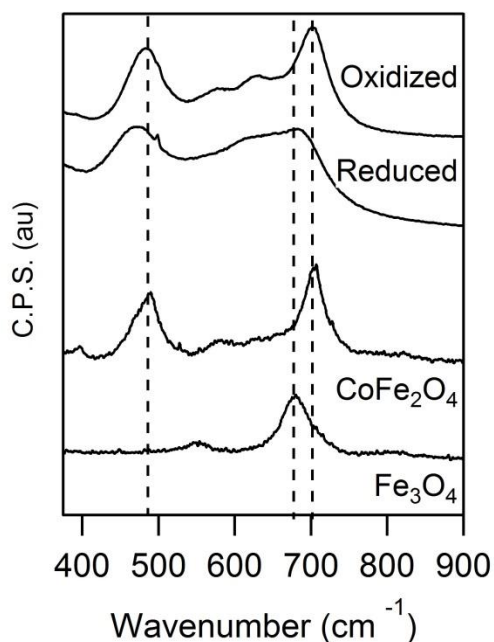


Figure 4.6: Raman spectra of fully oxidized CoFe_2O_4 and a CoFe_2O_4 sample reduced for three minutes. The peak shift to the left indicates a change in octahedral divalent cation from Co^{2+} to Fe^{2+} .

4.4.5 Oxidation Step

To investigate and compare the reduced ferrite reactivity with steam, sample materials were reduced for twelve minutes, then oxidized in 10% H_2O until H_2 levels returned to the baseline measured before reaction. Plots of the H_2 generation during H_2O oxidation and the total amounts of H_2 generated for each material are shown in Figure 4.7. Oxidation of the Fe-based material was rapid, with complete oxidation to Fe_3O_4 occurring in less than 30 min. Reduced CoFe_2O_4 took approximately 100 min to oxidize, while reduced NiFe_2O_4 took over eight hours to completely oxidize (the entire oxidation is not shown in Figure 4.6. For NiFe_2O_4 and CoFe_2O_4 oxidation, an initial peak transitioned into a long tail portion at about 25 min, and then H_2 levels slowly returned to baseline. Despite their lengthy oxidations, the total H_2 production per mass of material was factors of several greater for NiFe_2O_4 and CoFe_2O_4 than for Fe_2O_3 .

The solid material extent of reduction (X) was calculated from

$$X = \frac{\text{Moles } H_2 \text{ produced during oxidation}}{\text{Total active moles of O in sample}} \quad \text{Eq. 11}$$

The total active moles of O were calculated for each sample from the measured sample mass, with the assumption that Fe_2O_3 , $NiFe_2O_4$, and $CoFe_2O_4$ are the fully oxidized phases and Fe, Co, and Ni metals are the fully reduced phases. The Fe_2O_3 sample reached a conversion of 17%, while the $CoFe_2O_4$ sample conversion was 53% and the $NiFe_2O_4$ sample conversion was 68%. The high conversion of $NiFe_2O_4$ and $CoFe_2O_4$ in comparison to that of Fe_2O_3 was not surprising given FactSage thermodynamic predictions and supporting XRD data. Syngas entering the reactor is able to reduce both the Fe^{3+} and Fe^{2+} ions in the spinel when the ratios of pH_2/pH_2O and pCO/pCO_2 are high. As the reacting syngas is oxidized, these ratios fall below the minimum levels to reduce Fe^{3+} and Fe^{2+} . In the case of Fe_3O_4 , the syngas would cease to change the composition of the metal oxide through the remainder of the bed, as the gas phase would be in contact with only Fe^{2+} and Fe^{3+} ions. However, with $NiFe_2O_4$ and $CoFe_2O_4$, the oxidized syngas is still able to reduce the Ni^{2+} and Co^{2+} ions, leaving an Fe-rich spinel in the remainder of the bed. The Ni^{2+} and Co^{2+} ions are reduced throughout the entire bed, allowing a higher material conversion. This will be shown in more detail in Chapter 6.

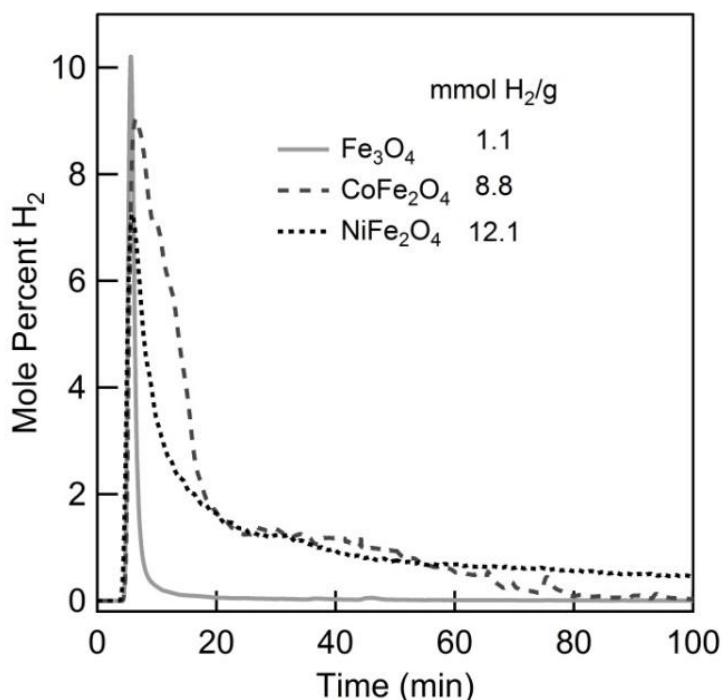


Figure 4.7: H₂ production comparison for Fe-only, NiFe₂O₄ and CoFe₂O₄ samples after 12 minutes of reduction. Each material proved to be reactive with H₂O, and NiFe₂O₄ and CoFe₂O₄ produce significantly more H₂ than the Fe-only material under these conditions.

Literature regarding the oxygen oxidation of NiFe and CoFe alloys indicates the long oxidation times are due to the incorporation of dopant cations Co²⁺ and Ni²⁺ into the spinel structure, a process that decreases the cation diffusion rates. [42] Oxygen oxidation experiments of NiFe alloys at 973 K show the formation of an outer layer of Fe₃O₄ in contact with a Ni-enriched alloy phase after only fifteen minutes. Almost 90 h into the oxidation, the Ni begins to be incorporated into the spinel layer. [43] Oxygen oxidation of 20% Fe/80% Ni alloy films at temperatures between 473 K and 673 K confirms the development of an outer layer of iron oxide and a metallic inner layer which is depleted of Fe during the oxidation process. [44, 45] The oxygen oxidation of a 48.7% Fe/49.3% Co/2% V alloy at temperatures between 773 K and 873 K results in the preferential oxidation of Fe, leaving a Co/V-enriched metal phase. A

CoFe₂O₄ phase formed upon further oxidation. [46] Although these referenced experiments were conducted with bulk samples in an oxygen environment, rather than sub-micron sized particles in a steam environment, they still illustrate the relative rates at which these processes occur.

As expected, regardless of the length of time required to fully oxidize the reduced materials, the experiments indicated complete oxidation was vital for complete conversion of H₂ and CO during the following reduction step. When oxidation reactions were terminated before H₂ levels returned to baseline, high levels of CO and H₂ were subsequently observed during the next reduction reaction because the spinel was left in an oxidation state with equilibrium p_{H₂}/p_{H₂O} and p_{CO}/p_{CO₂} ratios higher than 0.005. Since the production of steam for the oxidation process is energy intensive, long oxidation times can be prohibitive in an industrial setting. Consequently, the effect of H₂O concentration during oxidation and the effect of a surface catalyst should be explored to determine if the oxidation kinetics can be improved for these materials.

4.4.6 Cyclability

Multiple cycles were performed on each sample to determine the long term cyclability of NiFe₂O₄ and CoFe₂O₄. Materials were reduced for three minutes, then oxidized in 30% H₂O in Ar. Cycles are shown in Figure 4.8. Both materials prove to be highly cyclable with consistent H₂ production amounts. In contrast, under the same conditions the Fe-only material produced 0.9 mmH₂/g, only about 25% of the H₂ produced using NiFe₂O₄ and CoFe₂O₄.

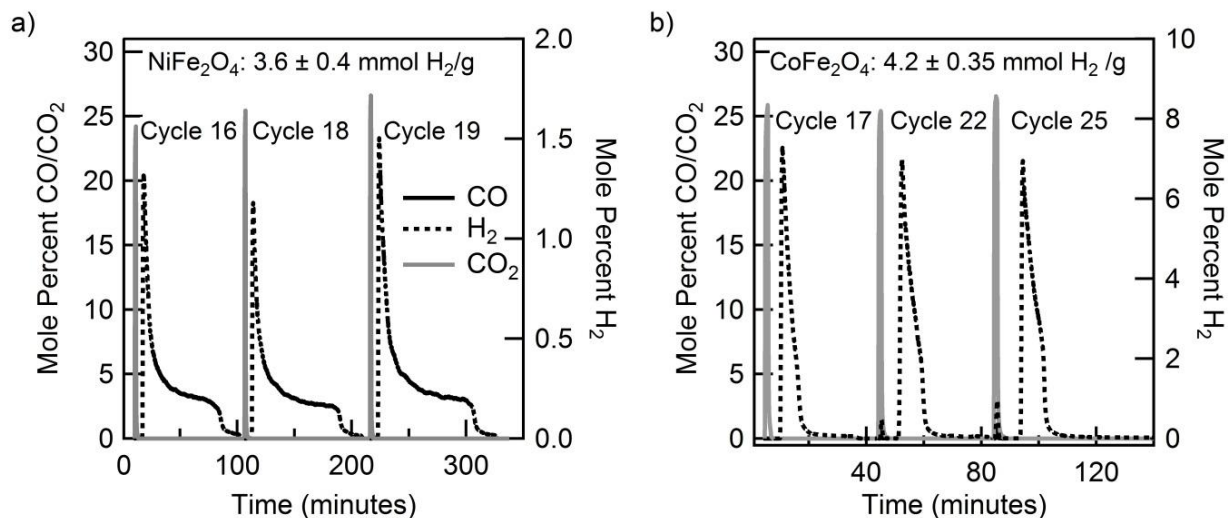


Figure 4.8: Cyclability of the a) NiFe_2O_4 and b) CoFe_2O_4 samples. Each was cycled over 20 times with stable H_2 production totals and peak rates.

4.4.7 Effect of Metal Oxide Choice on H_2 Recovery

The CLH process uses a reduction step to store the chemical energy of syngas in the reduced metal oxide material, leaving a stream of only H_2O and CO_2 , and then releases that energy in the form of pure H_2 during the oxidation step. Ideally, every mole of H_2 and CO used to reduce the metal oxide in the first step is converted to H_2 in the second step. With Fe_2O_3 , this is not possible, as the H_2 and CO used to reduce Fe_2O_3 to Fe_3O_4 is not recovered.

Figure 8 shows how the pre-breakthrough percent conversion of H_2/CO in the syngas back to H_2 during H_2O oxidation varies as a function of the conversion of Fe_2O_3 . This assumes uniform conversion throughout the sample. Up to 11% conversion of Fe_2O_3 results in 0% conversion of the syngas back to H_2 as this leaves a mixture of Fe_3O_4 and Fe_2O_3 , which is unable to split water. Once FeO begins to form, water splitting is possible and H_2 can be generated from the chemical energy stored during the reduction step. The maximum theoretical conversion of H_2 and CO in the syngas to H_2 during oxidation is 89%, which occurs at full conversion of the

Fe₂O₃ to Fe. With NiFe₂O₄ and CoFe₂O₄, 100% conversion of H₂ and CO in the syngas to H₂ at all extents of reduction are theoretically possible since NiFe₂O₄ and CoFe₂O₄ can be regenerated with H₂O alone.

To investigate this possibility, material balances were performed on the data taken to evaluate material cyclability, which were three minute reductions and subsequent oxidations in 30% H₂O. Total moles of H₂/CO fed to the reactor during reduction were calculated, and any H₂ or CO detected during the reduction step was quantified and subtracted from the calculated total amount fed. The resulting number was the amount of H₂ and CO consumed in the reaction. A carbon mole balance was generally closed to within 5%, calculated by comparing the amounts of CO and CO₂ measured during the reduction with the amount of CO and CO₂ fed to the reactor. The total amount of H₂ generated during the oxidation was then used to calculate how much of the H₂ and CO consumed in the reduction was recovered as H₂ during the H₂O oxidation. This ratio is called the syngas *conversion efficiency*

$$\text{Conversion Efficiency (\%)} = \frac{\text{Moles H}_2 \text{ generated during oxidation}}{\text{Moles H}_2 \text{ and CO consumed in reduction}} \times 100 \quad \text{Eq. 12}$$

Values calculated for Fe₂O₃, CoFe₂O₄, and NiFe₂O₄ are plotted in Figure 8. In these experiments, the Fe₂O₃ sample showed 18% solid conversion, calculated from the amount of H₂ and CO consumed in the reaction, and ~22% conversion efficiency. The NiFe₂O₄ and CoFe₂O₄ showed conversion efficiencies of nearly 90% and 95%, respectively, even though the solid conversion was only 22% and 24%, respectively. The highest reported conversion of solids in a packed bed without syngas breakthrough is 49%, achieved in a reactor optimized for the CLH process with counter-flow moving solids and gas. [12] This mixture was determined to be 74.6% FeO and 25.4% Fe, resulting in a potential conversion efficiency of 78%, though figures

concerning oxidation were not published in the study. Unlike the highly exothermic O_2 oxidation of Fe_3O_4 to Fe_2O_3 ($\Delta H = -84.5$ kJ/mole Fe_2O_3 at 873 K), the H_2O oxidation of Fe_3O_4 and Ni to $NiFe_2O_4$ and Co, and Fe_3O_4 to $CoFe_2O_4$, are only slightly exothermic ($\Delta H = -9.4$ kJ/mol $NiFe_2O_4$ at 873 K, $\Delta H = -7$ kJ/mol $CoFe_2O_4$ at 873 K). The trade-off between heat generation and additional H_2 production would need to be evaluated depending on the specifics of the system and the desired products, but $NiFe_2O_4$ and $CoFe_2O_4$ provide an option for significantly higher H_2 recovery that Fe-only materials cannot.

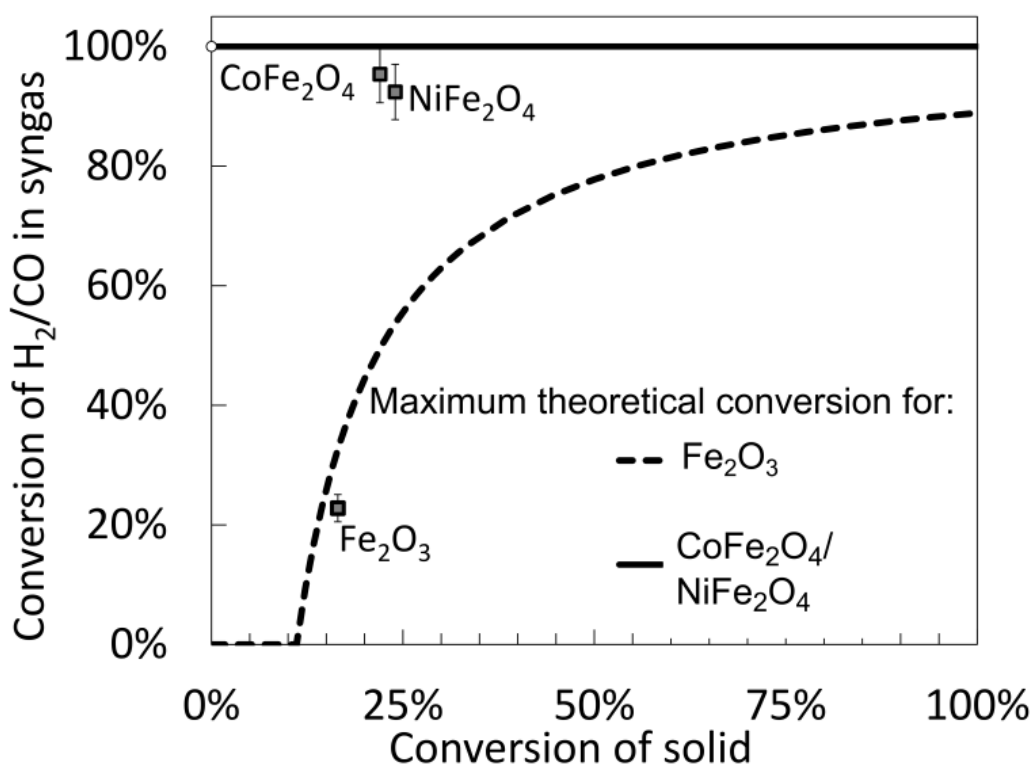


Figure 4.9: Conversion efficiency of Fe-based materials (- -) and mixed metal ferrites (-), and experimental results from laboratory packed bed reactor. Mixed metal ferrites approach the theoretical value of 100% conversion efficiency, while Fe-based materials approach their theoretical maximum of 25% conversion efficiency.

4.5 Conclusions

Investigation of NiFe_2O_4 and CoFe_2O_4 as CLH materials has shown both fully oxidized mixed metal spinels are indeed capable of oxidizing the H_2 and CO in syngas nearly fully to H_2O and CO_2 , and behave comparably to Fe_2O_3 during the reduction step. Findings are in accordance with thermodynamic predictions, which indicate syngas compositions between approximately 0.005-1 pCO/pCO_2 and 0.005 - 1.5 $\text{pH}_2/\text{pH}_2\text{O}$ will form a metallic phase and an Fe-enriched spinel phase. Analysis of the materials at three minutes and twelve minutes into the reduction showed the presence of a spinel structure and a metal phase at both times. Reduced NiFe_2O_4 and CoFe_2O_4 were highly reactive with steam and able to regenerate the mixed-metal spinel structure. The total H_2 production per mass of mixed metal spinel was four times greater than that of the Fe_2O_3 samples due to complete oxide regeneration in steam. In these experiments, Fe_2O_3 had a conversion efficiency of 22%, whereas NiFe_2O_4 and CoFe_2O_4 had conversion efficiencies of nearly 100%. Further research will focus on better understanding the rate limitations of the water oxidation step for the mixed metal ferrite, as well as further investigating the trade-off between heat/electricity production of the conventional Fe-based CLH process and the additional H_2 production with the novel mixed metal ferrites.

4.6 Acknowledgements

This work was supported by the National Science Foundation via Grant CBET 0966201, by the U.S. Department of Energy Fuel Cell Technologies Program via the Solar Thermochemical Hydrogen (STCH) directive, and by the U.S. Department of Education Graduate Assistance in Areas of National Need Program.

4.7 References

- [1] Farmer R. 2009 DOE Hydrogen Program & Vehicle Technologies Program. 2009. p. http://www.hydrogen.energy.gov/pdfs/review09/pd_0_farmer.pdf.
- [2] Solunke R, Veser G. Hydrogen Production via Chemical Looping Steam Reforming in a Periodically Operated Fixed-Bed Reactor. *Ind Eng Chem Res*. 2010;49:11037-44.
- [3] Smith B, Loganathan M, Shantha M. A Review of the Water Gas Shift Reaction Kinetics. *Int J Chem React Eng*. 2010;8.
- [4] Fan L. *Chemical Looping Systems for Fossil Energy Conversion*. Hoboken, NJ: John Wiley & Sons, Inc.; 2010.
- [5] Sircar S, Golden TC. Purification of Hydrogen by Pressure Swing Adsorption. 2000;35:667-87.
- [6] Bohn CD, Muller CR, Cleeton JP, Hayhurst AN, Davidson JF, Scott SA, et al. Production of Very Pure Hydrogen with Simultaneous Capture of Carbon Dioxide using the Redox Reactions of Iron Oxides in Packed Beds. *Ind Eng Chem Res* 2008;47:7623-30.
- [7] Gupta P, Velazquez-Vargas L, Fan L. Syngas Redox (SGR) Process to Produce Hydrogen from Coal Derived Syngas. *Energy Fuels*. 2007;21:2900-8.
- [8] Li F, Kim H, Wang D, Zeng L, Chen J, Fan L. Syngas Chemical Looping Gasification Process: Oxygen Carrier Particle Selection and Performance. *Energy Fuels*. 2009;23:4182-9.
- [9] Lorente E, Pena JA, Herguido J. Kinetic study of the redox process for separation and storing hydrogen: Oxidation stage and ageing of solid. *Int J Hydrogen Energy*. 2008;33:615-26.
- [10] Svoboda K, Siewiorek A, Baxter D, Rogut J, Pohorely M. Thermodynamic possibilities and constraints for pure hydrogen production by a nickel and cobalt-based chemical looping process at lower temperatures. *Energy Convers Manag*. 2008;49:221-31.
- [11] Svoboda K, Slowinski G, Rogut J, Baxter D. Thermodynamic possibilities and constraints for pure hydrogen production by iron based chemical looping process at lower temperatures. *Energy Convers Manag*. 2007;48:3063-73.
- [12] Li F, Zeng L, Velazquez-Vargas L, Yoscovitis Z, Fan L. Syngas Chemical Looping Gasification Process: Bench-scale Studies and Reactor Simulations. *AIChE J*. 2010;56:2186-99.
- [13] Graves P, Johnston C, Campaniello J. Raman Scattering in Spinel Structure Ferrites. *Mater Res Bull*. 1988;23:1651-60.
- [14] Scheffe JR, Allendorf MD, Coker EN, Jacobs BW, McDaniel AH, Weimer AW. Hydrogen Production via Chemical Looping Redox Cycles Using Atomic Layer Deposition-Synthesized Iron Oxide and Cobalt Ferrites. *Chem Mater*. 2011;23:2030-8.

- [15] Allendorf M, Diver R, Siegel N, Miller J. Two-Step Water Splitting Using Mixed-Metal Ferrites: Thermodynamic Analysis and Characterization of Synthesized Materials. *Energy Fuels*. 2008;4115-24.
- [16] Scheffe J, Li J, Weimer A. A spinel/hercynite water-splitting redox cycle. *Int J Hydrogen Energy*. 2010;3333-40.
- [17] DECTEROV SA, JUNG I-H, JAK E, KANG Y-B, HAYES P, PELTON AD. Thermodynamic modelling of the $\text{Al}_2\text{O}_3\text{-CaO-CoO-CrO-Cr}_2\text{O}_3\text{-FeO-Fe}_2\text{O}_3\text{-MgO-MnO-NiO-SiO}_2\text{-S}$ system and applications in ferrous process metallurgy. VII International Conference on Molten Slags Fluxes and Salts 2004.
- [18] Frisk K, Selleby M. The compound energy formalism: applications. *Journal of Alloys and Compounds*. 2001;320:177-88.
- [19] Jung IH, Decterov SA, Pelton AD, Kim H, Kang Y. Thermodynamic evaluation and modeling of the Fe-Co-O system. *Acta Materialia*. 2004;52:507-19.
- [20] Bale CW, Chartrand P, Degterov SA, Eriksson G, Hack K, R. Ben Mahfoud R, et al. FactSage Thermochemical Software and Databases. *Calphad*. 2002;26:189-228.
- [21] Bleeker MF, Veringa HJ, Kersten SRA. Deactivation of iron oxide used in the steam-iron process to produce hydrogen. *Appl Catal, A*. 2009;357:5-17.
- [22] Bleeker MF, Veringa HJ, Kersten SRA. Pure Hydrogen Production from Pyrolysis Oil Using the Steam-Iron Process: Effects of Temperature and Iron Oxide Conversion in the Reduction. *Ind Eng Chem Res*. 2010;49:53-64.
- [23] Yang J, Cai N, Li Z. Hydrogen Production from the Steam-Iron Process with Direct Reduction of Iron Oxide by Chemical Looping Combustion of Coal Char. *Energy Fuels*. 2008;22:2570-9.
- [24] Moran M, Shapiro H. *Fundamentals of Engineering Thermodynamics - 5th Edition*: John Wiley & Sons; 2004.
- [25] Spycher N, Reed M. Fugacity coefficients of H_2 , CO_2 , CH_4 , H_2O and of $\text{H}_2\text{O-CO}_2\text{-CH}_4$ mixtures: A virial equation treatment for moderate pressures and temperatures applicable to calculations of hydrothermal boiling. *Geochim Cosmochim Acta*. 1988;52:739-49.
- [26] Mattison T, Jardnas A, Lyngfelt A. Reactivity of Some Metal Oxides Supported on Alumina with Alternating Methane and Oxygens: Application for Chemical-Looping Combustion. *Energy Fuels*. 2003;17:643-51.
- [27] Hossain MM, Sedor KE, de Lasa HI. Co-Ni/ Al_2O_3 oxygen carrier for fluidized bed chemical-looping combustion: Desorption kinetics and metal-support interactions. *Chem Eng Sci*. 2007;62:5464-72.

- [28] Muller C, Bohn C, Song Q, Scott S, Dennis J. The production of separate streams of pure hydrogen and carbon dioxide from coal via an iron-oxide redox cycle. *Chem Eng J (Amsterdam, Neth)* 2011;166:1052-60.
- [29] O'Neil HSC, Navrotsky A. Simple Spinel: crystallographic parameters, cation radii, lattice energies, and cation distribution. *American Mineralogist*. 1983;68:181-94.
- [30] Unmuth EE, Schwartz LH, Butt JB. Iron Alloy Fischer-Tropsch Catalysts I. Oxidation-Reduction Studies of the Fe-Ni System. *Journal of Catalysis*. 1980;61:242-55.
- [31] Sloczynski J, Ziolkowski J, Grzybowska B, Grabowski R, Jachewicz D, Wcislo K, et al. Oxidative Dehydrogenation of Propane on $\text{Ni}_x\text{Mg}_{1-x}\text{Al}_2\text{O}_4$ and NiCr_2O_4 Spinel. *Journal of Catalysis*. 1999;187:410-8.
- [32] Ziolkowski J, Dziembaj L. Empirical Relationship between Individual Cation-Oxygen Bond Length and Bond Energy in Crystals and in Molecules. *Journal of Solid State Chemistry*. 1985;57:291-9.
- [33] Sickafus KE, Wills JM, Grimes NW. Structure of Spinel. *Journal of the American Ceramic Society*. 1999;82:3279-92.
- [34] Perron H, Mellier T, Domain C, Roques J, Simoni E, Drot R, et al. Structural investigation and electronic properties of the nickel ferrite NiFe_2O_4 : a periodic density functional theory approach. *Journal of Physics: Condensed Matter*. 2007;19.
- [35] Tihay F, Pourroy G, Richard-Plouet M, Roger AC, Kiennemann A. Effect of Fischer-Tropsch synthesis on the microstructure of Fe-Co-based metal/spinel composite materials. *Applied Catalysis A: General*. 2001;206:29-42.
- [36] Roiter BD, Paladino AE. Phase Equilibria in the Ferrite Region of the System Fe-Co-O. *Journal of the American Ceramic Society*. 1962;45:128-33.
- [37] Liao YY, Li YW, Hu XG, Chu JH. Temperature dependent phonon Raman scattering of highly a-axis oriented CoFe_2O_4 inverse spinel ferromagnetic films grown by pulsed laser deposition *Applied Physics Letters*. 2012;100:071905.
- [38] Shebanova ON, Lazor P. Raman spectroscopic study of magnetite (Fe_3O_4): a new assignment for the vibrational spectrum. *Journal of Solid State Chemistry*. 2003;174:424-30.
- [39] Hosterman BD. Raman Spectroscopic Study of Solid Solution Spinel Oxides. Las Vegas: University of Nevada; 2011.
- [40] Bahlawane N, Ngamou PHT, Vannier V, Kottke T, Heberle J, Kohse-Hoinghaus K. Tailoring the properties and the reactivity of the spinel cobalt oxide. *Physical Chemistry Chemical Physics*. 2009;11:9224-32.

- [41] da Cunha Belo M, Walls M, Hakiki NE, Corset J, Picquenard E, Sagon G, et al. Composition, structure and properties of the oxide films formed on the stainless steel 316L in a primary type PWR environment. *Corrosion Science*. 1998;40:447-63.
- [42] Wallwork G. The oxidation of alloys. *Rep Prog Phys*. 1976;5.
- [43] Menzies I, Lubkiewicz J. Oxidation of an Fe-12% NiAlloy in Oxygen at 700C-1000C. *Oxid Met*. 1971;3:41-58.
- [44] Bajorek C, Nicolet M, Wilts C. Preferential Oxidation of Fe in Permalloy Films. *Appl Phys Lett*. 1971;82:82-4.
- [45] Bruckner W, Baunack S, Hecker M, Thomas J, Groudeva-Zotova S, Schneider CM. Oxidation of NiFe(20 wt.%) thin films. *Mater Sci Eng B*. 2001;B86:272-5.
- [46] Sundar S, Deevi S. Isothermal oxidation behavior of FeCo-2V intermetallic alloy. *Intermetallics*. 2004;12:1311-6.

Chapter 5: Investigation of the H₂O Oxidation Kinetics of Reduced Fe₃O₄, CoFe₂O₄ and NiFe₂O₄ in a Stagnation Flow Reactor

5.1. Abstract

The oxidation kinetics of NiFe₂O₄, CoFe₂O₄, and Fe₃O₄ in H₂O at temperatures between 773 K and 873 K were investigated in a stagnation flow reactor. Thin films of metal oxides were deposited on higher surface area ZrO₂ substrates using atomic layer deposition (ALD) to minimize the effect of diffusion in the metal oxide oxidation. Materials were reduced in a syngas mixture, then oxidized in 10%, 20%, and 30% steam/He mixtures. The Fe₃O₄ sample showed no diffusion limitation during oxidation, instead following an order of reaction model with an $E_a = 78 \pm 10$ kJ/mol. This is believed to describe a surface reaction limitation. The mixed metal oxides also followed an order of reaction model with similar activation energies for the initial oxidation, followed by a diffusion limited reaction model with $E_a = 122 \pm 10$ kJ/mol (CoFe₂O₄) and 148 ± 15 kJ/mol (NiFe₂O₄). The diffusion limitation is believed to come from a decrease in the cation diffusion coefficient through the spinel as the concentration of the secondary cation increases. This eventually causes cation diffusion in the spinel to be slower than the initially limiting surface reaction.

5.2. Introduction

Mixed metal ferrites in the CLH process produce over three times the quantity of H₂ per cycle than conventional Fe-based materials. Although the materials look promising as candidate CLH metal oxides, the steam oxidation of the mixed metal ferrites in a packed bed reactor has been shown to take significantly longer than the oxidation of Fe-only material. A fundamental understanding of the mechanism of this slow oxidation and the factors that affect it would allow the development of superior materials and better utilization of active metal oxide.

Metal oxidation reactions are usually controlled by one of three processes: solid state diffusion, a surface reaction, or a reaction at the gas/solid or solid/solid interface (phase boundary). Solid state diffusion involves the migration of atoms through the lattice via defects, and is influenced by the type of atom moving and the number defects. [1] Surface reactions are numerous and depend upon the reactant species, but may include the adsorption of a reactant, rate of bond cleavage of the reactant ($\text{H}_2\text{O} \rightarrow \text{OH}_{(a)} + \text{O}_{(a)}$), or desorption of a reaction product. [2] For either of these processes to be rate-limiting, the chemical reaction in the solid must be rapid so the rate is controlled by reactants reaching or products leaving the reaction site. When the reaction itself is the slow step, a phase boundary control is typically observed since the reaction is usually occurring at a gas/solid or solid/solid boundary. [3]

In the case of iron, cobalt, and nickel metal oxidation, a scale of oxidized material (CoO , NiO , and Fe_3O_4) is formed over the top of un-oxidized metal. [4] In order for the metal to continue oxidizing, oxygen anions must diffuse through the scale through defects or metal cations and electrons must diffuse outwards through the scale through defects and holes to react with oxygen at the surface. [3] As the scale grows thicker, the additional diffusion distance decreases the oxidation rate. In each of these metals, the diffusion of oxygen through the metal oxide lattice has a lower diffusion coefficient due to a significantly higher energy barrier associated with the movement of large anions through the lattice. It is often assumed that the reaction between oxygen anions and metal cations takes place near the metal oxide surface rather than at the metal-oxide interface. [3] In support of this theory, outward diffusion of the metal cations has been found to be the rate controlling process for metal oxidation reactions when a compact scale is formed. [2, 5] The diffusion of the metal ions away from the metal and towards the surface can leave a void space after significant oxidation has occurred; however, at

small thicknesses, plastic deformation of an unconstrained scale allows continued contact with the metal. [2]

The O₂ and H₂O oxidation of Fe-, Co-, and Ni-only materials has been studied at length and some oxidation parameters found in literature are summarized in Table 5.1. Limited literature regarding the oxidation to mixed metal spinels exists in the literature, leaving the effect of the secondary cation on the oxidation unclear. The goal of this study is to investigate the effect of the Co and Ni cations on the kinetics of H₂O oxidation of Fe materials and to determine the rate-limiting mechanism during the oxidation.

Material	Oxidizer	Temperature (K)	Mechanism	Activation Energy (E_a) (kJ/mol)	Reference
FeO	H ₂ O	773-1173	Diffusion	77.9	[6]
MnFe ₂ O ₄	H ₂ O	773-1173	Diffusion	109.7	[6]
ZnFe ₂ O ₄	H ₂ O	773-1173	Diffusion	102.3	[6]
Fe	H ₂ O	1073 – 1400	Surface reaction	76	[7]
Fe	H ₂ O	973-1073	Surface reaction	47	[8]
FeO	CO ₂	973-1073	Surface reaction	73	[9]
			Diffusion	106	

Table 5.1: Experimental rate-limiting mechanisms and activations energies for Fe oxidation.

5.3. Materials and Methods

5.3.1. Sample Preparation

Since diffusion is often found to be rate-limiting for the oxidation of metals and metal oxides, materials with very small diffusion distances, like thin films, could improve the rates at which oxidation occurs. To generate metal oxides with small diffusion distances, samples were made using atomic layer deposition (ALD). The ALD process is a self-limiting deposition technique that allows metal oxide films to be deposited over high surface area substrates with precise control of the film thickness. [10] During the ALD process for metal oxide deposition, a

precursor containing the metal ion is dosed and reacts with hydroxyls on the surface of the material, leaving the surface covered with metal precursor molecules. Once all surface hydroxyls have been consumed or blocked due to steric hindrance from the attached metal precursor, no additional metal precursors attach to the surface. The reactor is purged and a second precursor is introduced to react with the ligands of the metal precursor, removing them and leaving hydroxyls on the surface. [11] After a purge step, the cycle is repeated. Film thickness increases layer-by-layer, allowing precise control over film thickness and mass percent of the metal oxide. Films are often amorphous as deposited, so calcination in air or an inert is necessary to form the desired metal oxide phase. [12]

Films of NiFe_2O_4 , CoFe_2O_4 , and Fe_3O_4 were deposited using ALD on crushed and sieved 50 m^2/g monoclinic zirconia. The support was identical to the support used for incipient wetness samples in the packed bed proof of concept study. Five grams of the substrate material were placed in a fluidized bed ALD reactor where they were alternately dosed with a metal precursor and O_2 at a temperature of 723 K and a pressure of 0.13 kPa. Metal precursors ferrocene, cobaltocene, and nickelocene were dosed from bubblers heated to 353 K. [12] During dosing, N_2 flowing through the bubbler was saturated with vapor and carried to the reactor. In-situ mass spectrometry was used to ensure that breakthrough was reached for each cycle. Between 20 and 35 total ALD cycles were performed on each sample, forming a 2-5 nm conformal metal oxide film over the surface of the support. The samples were annealed at 873 K for eight hours before characterization.

5.3.2 Material Characterization

Sample mass loadings and deposited cation ratios were confirmed via inductively coupled plasma-atomic emission spectroscopy (ICP-AES). Phase identification before and after

cycling was performed with a Raman spectrometer using a 532 nm Nd:YAG laser with a 1 μm spot size, calibrated with a neon lamp. Multiple sites on each material were sampled to ensure sample conformity. Surface areas were measured using Brunauer-Emmett-Teller (BET) surface area analysis. Samples were also examined with a JSM-7401F field emission scanning electron microscope (FESEM) equipped with an energy dispersive X-ray spectrometer (EDS) for surface elemental analysis and mapping.

5.3.3. Kinetic Analysis in Stagnation Flow Reactor

Kinetic parameters for each metal oxide were investigated using a stagnation flow reactor (SFR) system at Sandia National Laboratories, as shown schematically in Figure 5.1. [13] Reactant gas flow, controlled using calibrated mass flow controllers, proceeded through an insulated and heated stainless steel manifold to the reactor tube. A shallow, loosely packed bed of ferrite sample was placed on a flat ZrO_2 piece positioned at the bottom of the vertically oriented, closed-end, Al_2O_3 reactor tube. Reactant gases entered the reactor and impinged on the sample through an Al_2O_3 tube situated concentrically inside the outer closed-end tube. This inner tube was positioned such that gases exited it 8 mm above the sample surface, forming a region of uniform stagnation flow, thus eliminating velocity gradients over the top of the sample and allowing diffusive transport to dominate in reaction control volume. [13] The lack of thermal and velocity gradients allow the sample to be in contact with a uniform gas composition, providing an ideal environment for kinetic analysis. [14]

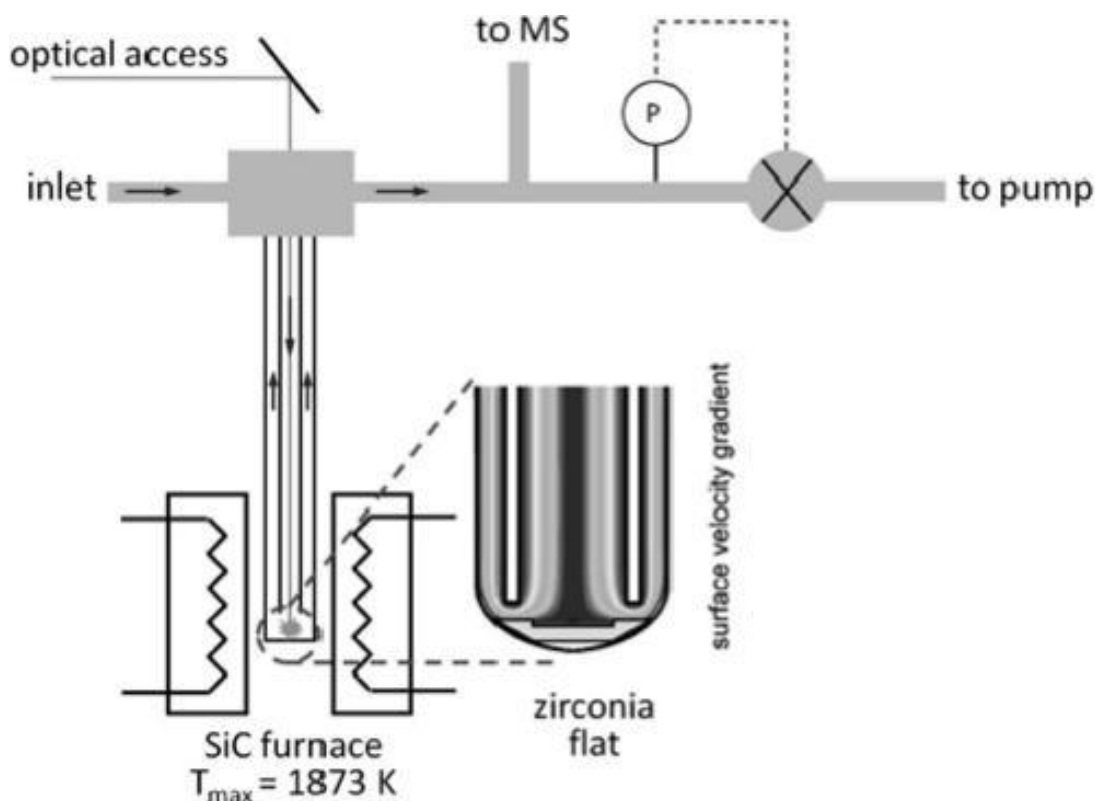


Figure 5.1: Stagnation flow reactor. Gases flow through the center tube and onto the sample at the bottom of the closed-end tube. Dimensions are such to minimize velocity gradients across the sample. From Scheffe *et al.* Chemistry of Materials 2011;23:2030 (Ref. [13])

After contact with the sample, the gases exited the reactor by flowing up between the tubes and out the top of the reactor. Exiting gas concentrations were measured with a differentially pumped, modulated effusive beam mass spectrometer (Extrell C50, 500 amu) designed to increase detection sensitivity in the presence of background gases. The mass spectrometer was calibrated daily using analytical standard gases, with four-point calibrations in the H₂, CO, and CO₂ partial pressure ranges observed during reduction and oxidation reactions. To prevent H₂O from entering the mass spectrometer during H₂O oxidation, H₂O was condensed out of the gas stream in liquid nitrogen cooled cryogenic trap prior to gas sampling.

A vacuum pump and pressure controller were used to maintain a constant 1 kPa pressure in the system during the reaction. Samples were reduced for ten minutes at 873 K using a syngas mixture containing 2% CO₂/ 2% H₂/2% CO/Balance He to simulate reduction conditions during the CLH process. [15] Oxidization of the reduced material occurred at temperatures between 773 K and 873 K in 10% H₂O in Helium for Fe –only samples, and in 10%, 20%, and 30% H₂O in Helium for CoFe₂O₄ and NiFe₂O₄. Steam was generated at 348 K using a RASIRC steam generation unit incorporating a humidity sensor that allowed accurate water flow rate control and recording during the reaction. Oxidations were continued until the H₂ signal returned to its baseline, usually after 10 to 30 minutes of oxidation.

5.3.4. Method of Kinetic Analysis

5.3.4.1 Mathematical Model of Reactor

The measured H₂ production ($MH_2(t)$, in moles), as monitored by mass spectrometry, was used to hypothesize a reaction model for each material using standard solid state kinetic models.[16] These models assume that the rate of reaction, and therefore H₂ production, is governed by non-equilibrium processes on the material surface or in the material bulk. [17] Solid state reaction rates are generally expressed as follows:

$$\frac{d\alpha}{dt} = k f(\alpha) \quad \text{Eq. 5.1}$$

where α is the material conversion, $\frac{d\alpha}{dt}$ is the reaction rate, and k is a temperature dependent Arrhenius kinetic expression, $Ae^{\frac{-E_a}{RT}}$, where A is the pre-exponential constant, E_a is the activation energy for the reaction, R is the ideal gas constant, and T is the reaction temperature in Kelvin. Material conversion, $\alpha(t)$, at time t is calculated for these experiments using:

$$\alpha(t) = \frac{\int_0^t MH_2(t)dt}{\int_0^{t_f} MH_2(t)dt} \quad (0 \leq \alpha \leq 1) \quad Eq. 5.2$$

The t_f term indicates the time that oxidation is complete, such that $\alpha(t)$ represents the ratio of moles of hydrogen produced at time t to the total moles of hydrogen produced when the reaction has finished. Since the moles of H_2 generated during oxidation is equivalent to the moles of oxygen gained by the sample, H_2 measurement can be used as an analogue to calculate material conversion. In Eq. 10, the $f(\alpha)$ term represents the reaction model, which expresses how the reaction rate changes as a function of the conversion. [18] Models for $f(\alpha)$ are mathematically derived based on common reaction pathways such as nucleation and growth throughout a particle, surface nucleation and growth according a particle geometry, diffusion through a product layer, or rate proportional to the amount of unreacted material. [16] Common $f(\alpha)$ terms are shown in Table 5.2.

Common Reaction Pathway Models		
	Differential	Integral
Model	$f(\alpha) = \frac{1}{k} \frac{d\alpha}{dt}$	$g(\alpha) = kt$
Power Law (P2)	$2\alpha^{1/2}$	$\alpha^{1/2}$
Contracting Volume	$3(1-\alpha)^{2/3}$	$1-(1-\alpha)^{1/3}$
1-D Diffusion	$1/2\alpha$	α^2
Second Order	$(1-\alpha)^2$	$[1/(1-\alpha)]-1$
Third Order	$(1-\alpha)^3$	$(1/2)[(1-\alpha)^{-2}-1]$

Table 5.2: Common $f(\alpha)$ terms that express how the rate of reaction changes with reaction extent.

As described by Scheffe, et al., [14] in the SFR the transient nature of the H_2 generated during oxidation is distorted due to the time lag before the H_2O impinges on the sample, the detector time lag, and the dispersion of the gases as they flow through the reactor tube, manifold, and the volume of the liquid nitrogen water trap, as shown in Figure 5.2. These effects can have a significant impact on the shape of the H_2 generation curve and on the solid state model that is

found to best describe the reaction, and thus the determined rate-limiting oxidation mechanism. To account for the effects of these reactor-specific phenomena, the models developed in [14] for the water-delivery to the reactor and for the dispersion of the H_2 downstream of the reactor were used in this analysis. A simulation of the water delivery through the manifold and reactor tube provided an expression for a time-dependent water flow to the sample, and a simplified model of the reactor volume, cryogenic trap, and downstream manifold as a series of CSTR's accounted for the dispersion of the H_2 before the detection, as well as the time lag to reach the detector. The number of CSTR's, the space velocity (τ), and the detector time lag (t_s) were determined with H_2 pulse experiments through and around the reactor and cryogenic trap.

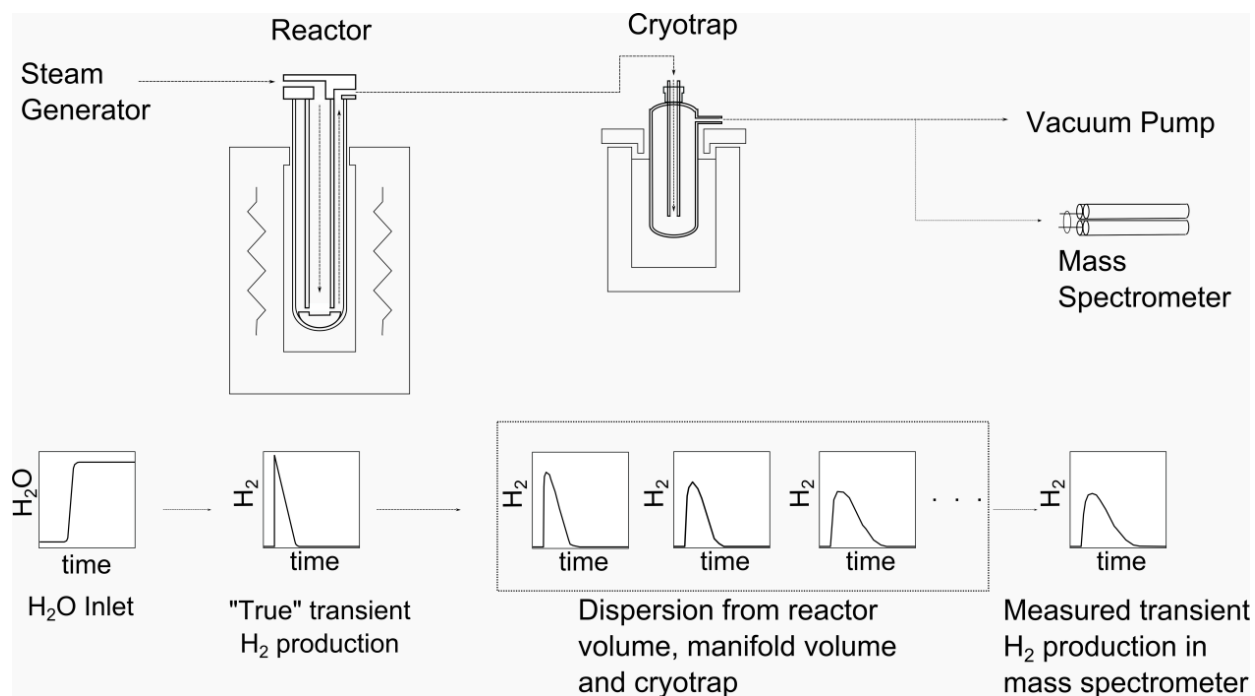


Figure 5.2: Each component of the system introduces dispersion, which affects the measured peak shape and kinetic model if not accounted for in analysis.

The equations used to model the system are shown in Table 5.3. Equation 5.3 shows the extent of reaction of the material based on a solid state reaction model, and Equation 5.4 shows

the total extent of reaction if more than one reaction occurs simultaneously. The water mole fraction, $Y_{H_2O,k}$, includes the time-dependent correction from the steam delivery system simulation. Equation 5.6 expresses a series of n CSTR's and is used to model the dispersion of H₂ and detector lag time, and Equation 5.6 relates the H₂ mole fraction and the reaction extent. The experimental H₂ mole fraction detected at the mass spectrometer, $\bar{Y}_{H_2,k}$ is compared with the predicted H₂ mole fraction, $Y_{H_2,n=last,k}$, and the residual sum squared error is used to optimize the kinetic parameters A_i , E_i , and γ for given solid state models $f(\alpha_i)$.

A Mathematica script was written to read kinetic data at different temperatures and H₂O concentrations, guess model values of A, Ea, and γ , and solve the differential equations in Table 5.3 using the NDSolve function. The model then compares predicted H₂ mole fraction to the measured H₂ mole fraction and minimizes Equation 5.7 using the NMinimize numerical minimization routine. This analysis led to the global best-fit mechanism and parameters, as the error associated with every data point was included in the minimization.

$\frac{d\alpha_{i,k}}{dt} = A_i * [Y_{H_2O,k}(t - t_{s,k})]^{Y_{H_2O_i}} * \exp\left[\frac{-E_i}{RT}\right] * f(\alpha_i)$		Eq. 5.3
$\frac{d\alpha_{tot,k}}{dt} = \sum_i \frac{d\alpha_{i,k}}{dt}, \alpha_{tot,k} \leq 1$		Eq. 5.4
$\frac{dY_{H_2,n,k}}{dt} = \tau_k * (Y_{H_2,n-1,k} - Y_{H_2,n,k})$		Eq. 5.5
$Y_{H_2,0,k} = \frac{v_{H_2,k}}{F_{tot,k}} * \frac{d\alpha_{tot}}{dt}$		Eq. 5.6
$RSSQ = \sum_k \sum_t \omega_{H_2,k} * [\bar{Y}_{H_2,k} - Y_{H_2,n=last,k}]^2$		Eq. 5.7
i	Reaction model (process)	
k	Experiment number (run #)	
α	Extent of reaction	
A	Pre-exponential factor (1/s)	
E	Activation Energy (kJ/mol)	
γ	Reaction Order	
Y_{H_2O}	Mole Fraction H ₂ O	
τ	Space velocity (1/s)	
t	Detector time lag (s)	
V	Standard volume (scm ³)	
F	Standard total flow rate (scm ³ /s)	
ω	Weighting factor	

Table 5.3: Equations used in modeling the oxidation kinetics.

5.3.4.2. Determination of τ and t_{shift}

To determine the dispersion of the H₂ through the system and cryotrap, pulses of H₂ were sent through the system, measured with the mass spectrometer, and the H₂ was modeled as the output of a series of CSTR's. The variables τ , t_{shift} , and the number of CSTR's were determined by a least squares analysis that compared the predicted H₂ response with the measured H₂ signal from the reactor. With higher H₂O concentrations, larger deviation from the original pulse was observed due to higher dispersion in the cryotrap as an increased volume of gases were condensed out of the gas flow, as evident in the values of τ required in the model to obtain a good fit with the pulse data.

5.4 Results and Discussion

5.4.1 Material Characterization

Sample properties are shown in Table 5.4. After deposition of the metal oxides and annealing, surface areas were between 35 and 40 m²/g. Metal oxide phases CoFe₂O₄ and NiFe₂O₄ were identified using Raman Spectroscopy to confirm formation of the mixed metal spinel phase before and after cycling, as shown in Chapter 3. In accord with the incipient wetness samples, no evidence of cation interaction with, or diffusion into, the ZrO₂ lattice was observed for the ALD materials.

Sample	Metal Oxide (Mass %)	Cation ratio	Surface Area (m ² /g) (before cycling)	Surface Area (m ² /g) (after cycling)
CoFe ₂ O ₄	12.2	2.15:1 Fe:Co	41 ± 2	19 ± 2
NiFe ₂ O ₄	18.3	2.3:1 Fe:Ni	36 ± 2	19 ± 2
Fe ₂ O ₃	13.1	All Fe	39 ± 2	17 ± 2

Table 5.4: Mass % metal oxide, cation ratio, and surface areas of ALD materials used in the kinetic study.

5.4.2 Material Cyclability

Before kinetic analysis, cyclability of the ALD material was established to ensure that changes in the transient nature of H₂ production were due solely to kinetic changes. The CoFe₂O₄ showed excellent cyclability, as shown in Figure 5.3. The NiFe₂O₄ and Fe₃O₄ materials showed more variability from cycle to cycle, which added additional error to their determined kinetic parameters. These samples also showed an initial decrease in peak H₂ production, but stabilized after a few cycles. This was most likely due to sintering and the associated surface area decrease of the metal oxides in the first few cycles since ZrO₂ substrate itself does not see a significant surface area change at 873 K. As shown in Table 5.4, the surface areas of the samples decrease to around 20 m²/g during cycling.

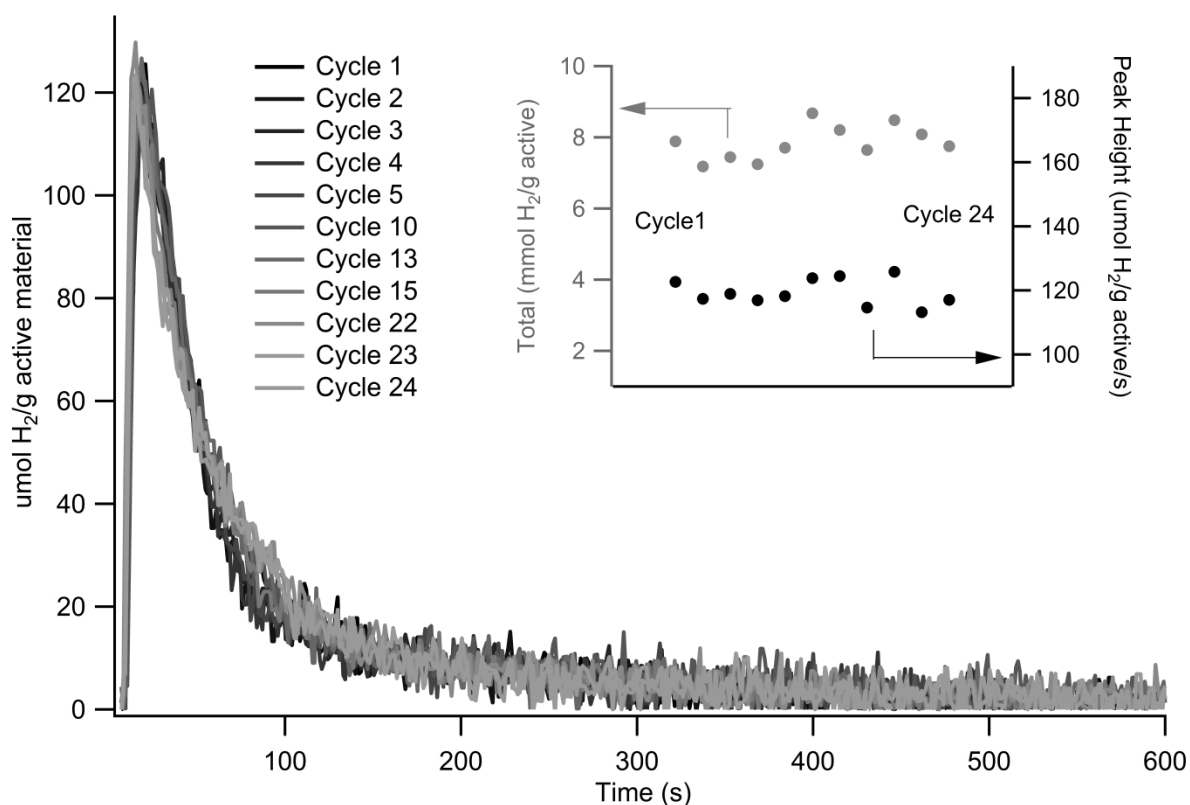


Figure 5.3: Cyclability of CoFe₂O₄ sample

5.4.3 Kinetic Analysis

Analysis using the method described in Section 5.3.4 shows that a second order reaction model gave a minimum global error for the oxidation of reduced Fe₃O₄, with an activation energy of 78 ± 10 kJ/mole. This second order reaction model is similar to kinetic models used in homogeneous gas phase kinetics, and indicates that the reaction rate is proportional to the amount of unreacted iron in the sample. [16] Figure 5.4 shows the quality of fit over the temperature range investigated.

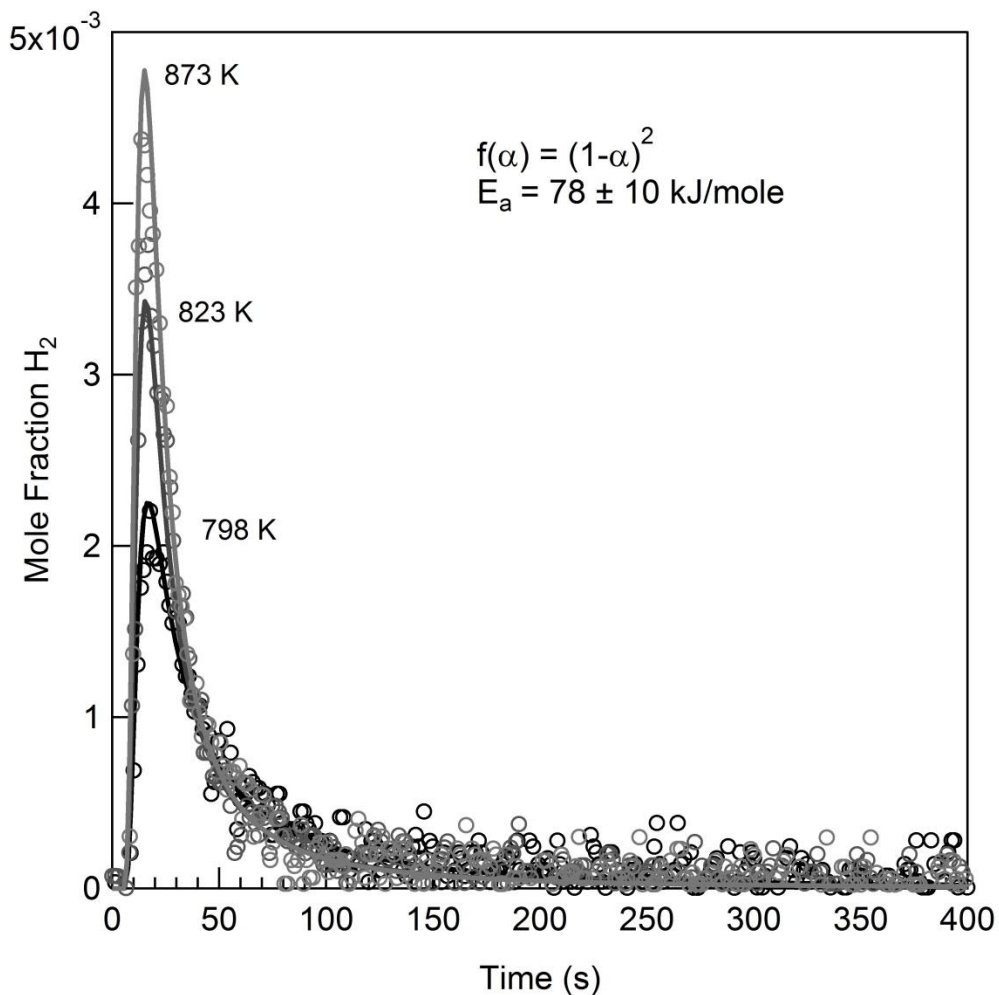


Figure 5.4: Fe data and best-fit kinetic model.

As seen in the packed bed experiments reported previously in Chapter 3, the NiFe₂O₄ and CoFe₂O₄ oxidations were initially rapid, but H₂ production slowed before returning to baseline, especially for the NiFe₂O₄ material, and shows a long plateau of H₂ production before the reaction is stopped. This is again in contrast with the rapid oxidation of the Fe-only material under the same conditions.

Analysis of the NiFe₂O₄ using only one model did not give an adequate fit over the entire time domain of the reaction. Figure 5.5 shows the best fit with a third order reaction model, the

single model with the lowest error. While this model predicts the peak H_2 production with some accuracy, it fails to capture the long-term slow H_2 production observed after the initial peak. A diffusion limited model predicts peak H_2 production uncharacteristic of the observed peak behavior, but accurately describes the tail portion of the reaction. A model that includes these two simultaneous reaction mechanisms fits the data with lower global error than the single model. Figure 5.5 shows the best fit for the data in this range. Although the diffusion limited model does not appear to add significant H_2 at any single point in time, the small production over the time during which it is active results in nearly 20% of the total H_2 production of the material. The reaction order model was found to have an $E_a = 68 \pm 13$ kJ/mol, and the diffusion-based model had an $E_a = 148 \pm 15$ kJ/mol. At near complete conversion, the parabolic rate equation no longer accurately described the rate of H_2 production, indicating an additional rate controlling mechanism change. This may be due to a thermodynamic limitation. The equilibrium constant for

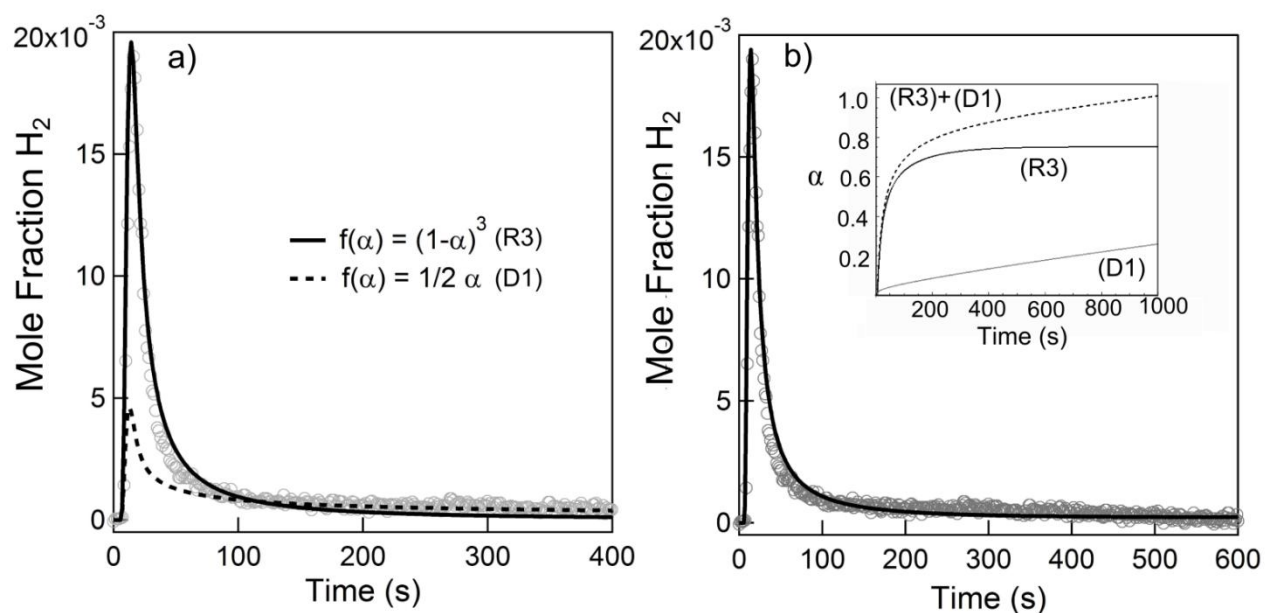


Figure 5.5: a) An order of reaction model fits the reaction peak, while a diffusion model fits the long-term H_2 production b) A combination of two kinetic models gives the best fit for the $NiFe_2O_4$ material.

H₂O oxidation of the nearly-fully oxidized NiFe₂O₄ is small, and at some point the amount of H₂O supplied will not be sufficient to observe a kinetic limitation.

Analysis of CoFe₂O₄ kinetic data similarly showed that a single model systematically under predicted the H₂ production after 200 s of oxidation. A dual model analysis found the best fit for CoFe₂O₄ data to be a second order reaction model with an $E_a = 79 \pm 8$ kJ/mol, and a diffusion based model with an $E_a = 122 \pm 10$ kJ/mol.

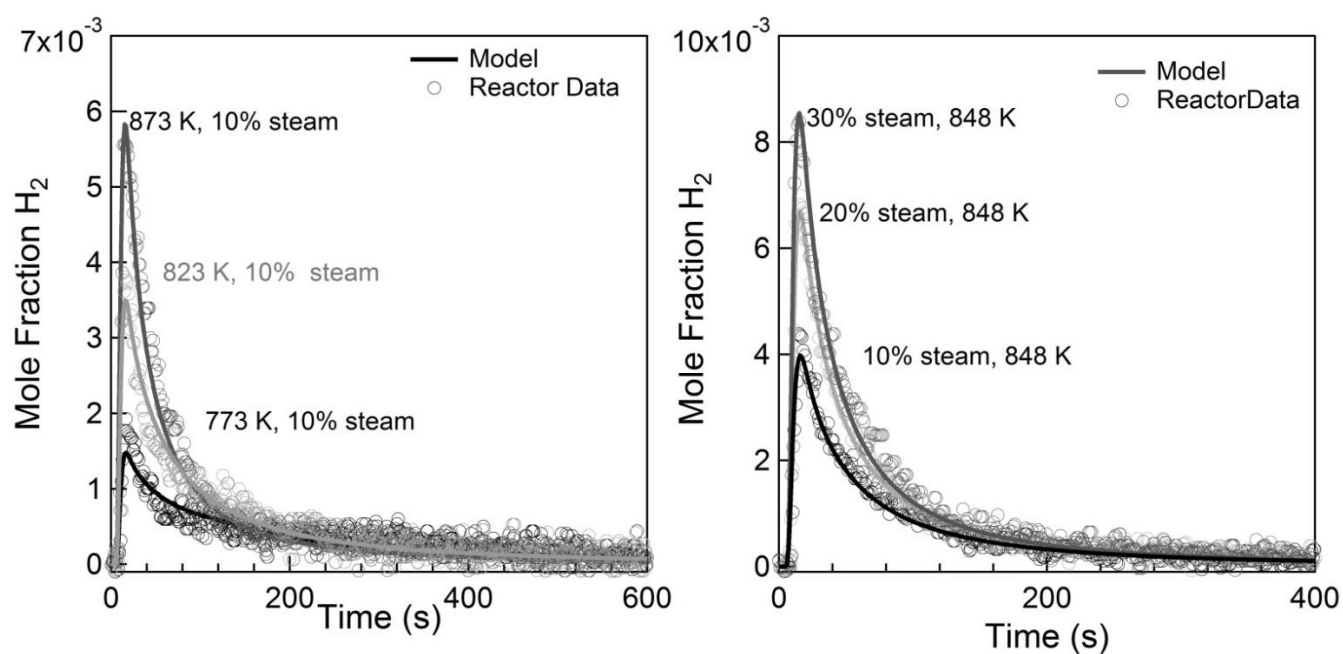


Figure 5.6: CoFe₂O₄ kinetic plots.

The activation energies calculated in this study are reasonable when compared with literature values for similar materials shown in Table 5.1. Activation energies for FeO, MnFe₂O₄, and ZnFe₂O₄ oxidation with H₂O are reported between 78 and 110 kJ/mol. [19] Oxidation of ZnFe₂O₄ with CO₂ has an activation energy of 73.4 ± 8.5 kJ/mol. [20]

The Fe oxidation to Fe₃O₄ is consistently found to follow a diffusion-limited mechanism after an initial rapid surface oxidation. [8, 9] A spectral emissivity study of the air oxidation of polished Fe discs at temperatures between 688 K and 843 K shows oxide film thickness increases as predicted by the parabolic model for up to 24 h with an E_a of 155 ± 15 kJ/mol. [21] Oxidation of Fe rods in 5% H₂O at temperatures between 623 K and 823 K show adherence to a surface-limited reaction mechanism followed by a parabolic diffusion mechanism at high temperatures. The E_a value for the surface limited reaction is calculated to be 47 kJ/mol. [8] A study of the CO₂ oxidation of ~50 μm diameter FeO powder at temperatures between 923 K and 1473 K shows the reaction to be controlled initially by a surface reaction with an E_a of 73.4 ± 8.5 kJ/mol, followed by a parabolic reaction with an E_a of 106.4 ± 8.8 kJ/mol. [9] Steam oxidation of 100-150 μm reduced Fe₂O₃ particles follows a diffusion limited model, the Jander equation, with an E_a of 77.9 kJ/mol between 773 K and 1173 K; however, the quality of fit is poor in this study. [6] Further support for an initial surface reaction limitation is found in literature reporting success in the use of surface catalysts to enhance the H₂O oxidation of

	Region 1		Region 2	
<u>Material</u>	<u>Reaction Type</u>	<u>E_a (kJ/mol)</u>	<u>Reaction Type</u>	<u>E_a (kJ/mol)</u>
Fe ₂ O ₃	Second Order	78 ± 10	-	-
NiFe ₂ O ₄	Third Order	68 ± 13	Parabolic diffusion	148 ± 15
CoFe ₂ O ₄	Second Order	79 ± 8	3D diffusion	122 ± 10

Table 5.5: Models and activation energies determined experimentally for the oxidation of Fe₂O₃, CoFe₂O₄, and NiFe₂O₄ materials.

reduced metal oxides. [22] Deposition of Rh, Pt, and Ru decrease the temperature at which H_2 is evolved during H_2O oxidation of Fe materials; however, a mechanism is not proposed in the referenced study.

Experiments in this study showed that solid state diffusion effects during oxidation were eliminated from the Fe_3O_4 samples under these reaction conditions. Instead, an order of reaction model is observed, with an E_a comparable to the surface reactions reported in [8] and [9]. We believe that due to the thin film materials on high surface area supports, oxidation of these materials remains in the surface reaction limited regime for the entire extent of the reaction. Materials that reported parabolic diffusion limitations in Fe_3O_4 were using materials with longer diffusion distances than the ALD-prepared materials. The smallest metal oxide particles were 50 μm in diameter. Although we expect some sintering and agglomeration of the ALD films during cycling, we do not expect the metal oxide agglomerates to reach sizes larger than a few μm due to the substrate material and the sample mass loadings. In fact, images from SEM analysis before and after cycling, shown in Figure 5.7, demonstrate the development of $\sim 1 \mu m$ agglomerates of metal oxide during cycling. Under these conditions, the cation diffusion in the Fe_3O_4 film material is rapid enough to not be rate controlling.

While diffusion effects were successfully eliminated from the Fe_3O_4 samples, kinetic fits with the lowest global error for the similarly prepared thin film $CoFe_2O_4$ and $NiFe_2O_4$ samples contained a diffusion limited model at high conversions during oxidation under the same conditions. The best fit combination of models could be considered a completely empirical method of describing these complex reactions; however, literature regarding the oxidation of mixed metal oxides indicates that a two stage model can be a reasonable approximation of the solid state processes occurring during oxidation.

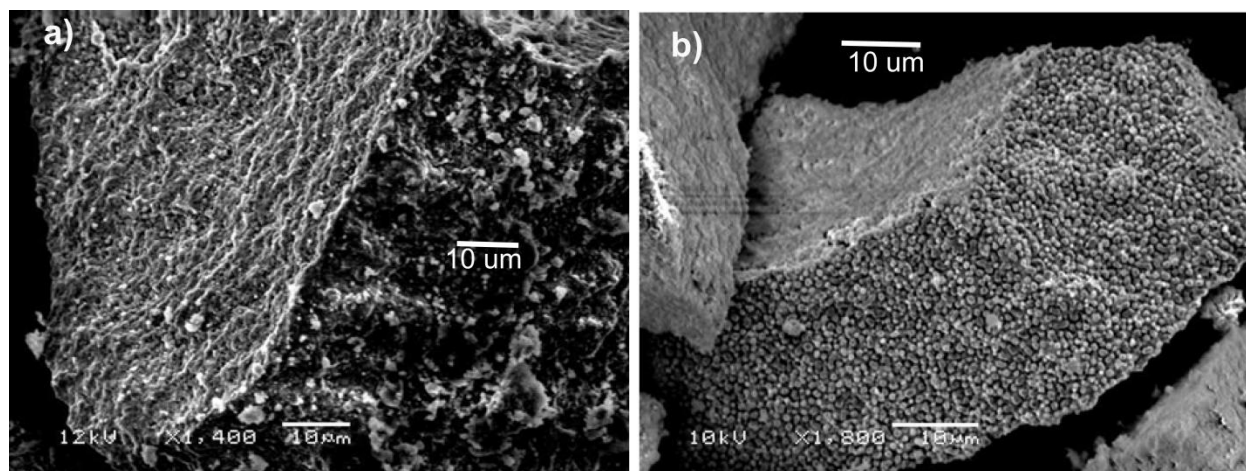


Figure 5.7: a) SEM image of uncycled sample b) SEM image of sample after 20 cycles. $1\ \mu\text{m}$ agglomerates of metal oxide form during cycling.

Although only a small amount of data regarding oxidation of reduced NiFe_2O_4 or CoFe_2O_4 at temperatures between 773 K and 873 K are published in the literature, data regarding alloy oxidation can address the observed mechanism change to a diffusion limited reaction at high conversions. When mixed metals are oxidized, the metal with the most negative Gibb's free energy of oxidation, ΔG_{oxd} , will usually oxidize first and form a protective scale, a process called selective oxidation. [3] Observed in materials such as steel, selective oxidation of one alloy constituent leaves an alloy enriched in the second alloy constituent. The second metal will also eventually oxidize, if able, and will form a thermodynamically stable oxide phase. [2] Thermodynamic analysis predicts the scale and alloy composition at equilibrium conditions, though knowledge of the diffusion processes in both the alloy and the scale is key to developing an understanding of the oxidation kinetics. Similar to the oxidation of pure metals, several possible rate-limiting steps exist for the oxidation of alloys: diffusion in the scale, diffusion in the alloy, or an alloy/scale or scale/gas interface reaction. A scale will only form and continue to grow if diffusion is rapid in the alloy, allowing the more easily oxidized metal to be replenished at the scale-alloy interface. In this case, the reaction at the scale/alloy interface or diffusion

through the scale is rate-limiting. If diffusion in the alloy is slow, then the alloy/scale interface becomes depleted and the diffusion in the alloy becomes rate-limiting. [2]

At 873 K, the ΔG_{oxd} for the Fe to Fe_3O_4 oxidation is -414 kJ/mol O_2 , for the oxidation of Ni to NiO it is -320 kJ/mol O_2 , and for Co to CoO it is -345 kJ/mol O_2 . [2] These values indicate that if preferential oxidation occurs in a NiFe alloy or CoFe alloy, Fe would be the first metal to oxidize. Experimentally, oxygen oxidation experiments of NiFe alloys at 793 K show the formation of an outer layer of Fe_3O_4 in contact with a Ni-enriched alloy phase after fifteen minutes. At longer oxidation times, Ni was incorporated into the spinel. [23] Oxygen oxidation of 20% Fe/80% Ni alloy films at temperatures between 473 K and 673 K confirms the initial development of an outer layer of iron oxide and a metallic inner layer that is depleted of Fe during the oxidation process. [24, 25] Similarly, the oxygen oxidation of a 48.7% Fe/49.3% Co/2% V alloy at temperatures between 773 K and 873 K results in the preferential oxidation of Fe, leaving a Co/V-enriched metal phase. A CoFe_2O_4 phase forms upon further oxidation. [26]

To determine the phases present in the reduced NiFe_2O_4 sample when the reaction mechanism changes from a third order reaction to a diffusion controlled reaction, oxidation of the reduced NiFe_2O_4 was stopped immediately following the peak H_2 production. Analysis of the resulting material with XRD indicated the presence of only Fe_3O_4 and a metallic phase. Since the material was partially oxidized without formation of an oxidized Ni phase, such as NiFe_2O_4 or NiO, we believe preferential oxidation of the reduced Fe may have occurred. A similar analysis could not be completed for CoFe_2O_4 due to the inability to differentiate between CoFe_2O_4 and Fe_3O_4 with XRD.

In our analysis, the initial peak observed in CoFe_2O_4 and NiFe_2O_4 oxidation is best described with an “order of reaction” model, similar to the oxidation of the Fe-only material, with

measured E_a values close to that of the Fe-only material (79 ± 8 kJ/mole and 68 ± 13 kJ/mole in comparison to 78 ± 10 kJ/mol). This indicates a similar process controls the reaction rate for each of these materials during the peak of H_2 production, most likely a surface reaction with H_2O as observed in the oxidation of Fe.

Studies of vacancy formation and migration in $CoFe_2O_4$ at high temperatures (1473 K) show that diffusion occurs by migration through cation vacancies at high O_2 activities. [27] As the spinel becomes less Fe-rich at the same O_2 activity, the overall defect concentration decreases, an effect attributed to the increasing difficulty of oxidizing Me^{2+} to Me^{3+} as the cobalt concentration increases. These defect changes cause the measured cation tracer diffusion rate to decrease two orders of magnitude as the composition of the spinel changes from Fe_3O_4 to $CoFe_2O_4$ at 1473 K.

Oxygen activity dependence of the rate-limiting cation migration mechanism has also been observed in Fe_3O_4 between the temperatures of 773 K and 1473 K, and several studies all indicate the same type of materials behavior as a function of O_2 activity, regardless of the temperature. [5, 28, 29] For Fe_3O_4 , low temperature data agree with data extrapolation from higher temperature studies to lower temperature studies. Similarities between the behavior of Co and Ni tracers in Fe_3O_4 and Fe self diffusion in Fe_3O_4 indicate that the mechanism is the same for cation transport of each through the spinel lattice. [30]

Although no comprehensive data regarding the diffusion mechanisms in $CoFe_2O_4$ and $NiFe_2O_4$ at 873 K exist in literature, the similarities between Fe_3O_4 and $CoFe_2O_4$ diffusion data indicate that high temperature $CoFe_2O_4$ data may be accurately extrapolated to lower temperatures. In this case, the diffusion limitation seen in the kinetic analysis presented here is most likely related to the decrease in cation vacancies as the secondary cation content of the

Fe_3O_4 increases. As the secondary cation concentration increases in the oxidized layer, the diffusion coefficient decreases until it becomes the rate-limiting process and H_2 production reflects the controlling mechanism change. The E_a for the diffusion – limited portion increases between CoFe_2O_4 and NiFe_2O_4 , which may be due to a difference in the energy of formation of vacancies between the two oxides, or in the difference in energy barriers of cation migration in NiFe_2O_4 in comparison to CoFe_2O_4 . A diffusion limitation involving the metal atoms through the un-oxidized phase, as mentioned above, is also possible. Vacancy formation enthalpies and migration barriers for pure Co, Fe and Ni and their corresponding alloys, as well as the spinel phases Fe_3O_4 , NiFe_2O_4 and CoFe_2O_4 , were investigated using density functional theory calculations. As detailed in Appendix A, the migration barriers were found to be greater in the spinel phase than in the metallic phase for each system, confirming diffusion in the spinel phase as the most likely kinetic limitation.

5.5 Conclusions

Using the ALD method as a sample preparation technique was generally successful in eliminating the diffusion effects often found to limit metal oxidations in H_2O . The Fe-only sample showed no diffusion limitations during oxidation and was shown to fit a reaction order model with an E_a of 78 ± 10 kJ/mol, consistent with other observed surface reaction-limited behavior. The CoFe_2O_4 and NiFe_2O_4 sample oxidations were initially limited by the reaction order model, similarly to the Fe_3O_4 sample and with nearly identical E_a 's (79 ± 8 kJ/mol and 68 ± 13 kJ/mol). Despite identical sample preparation and cycling techniques, the CoFe_2O_4 and NiFe_2O_4 samples showed a diffusion limitation during the last portion of the oxidation. This is believed to be caused by a decrease in the diffusion coefficient through Fe_3O_4 as the concentration of a secondary cation increases. As the Co and Ni are incorporated into the spinel, the cation

diffusion rate decreases, eventually becoming slower than the surface reaction and affecting the rate of H₂ production. The E_a for diffusion in the NiFe₂O₄ layer is greater than the E_a for diffusion in the CoFe₂O₄ layer (148 ± 15 kJ/mol vs. 122 ± 10 kJ/mol).

5.6 Acknowledgements

The author wishes to thank Tony McDaniel at Sandia National Laboratories in Livermore, CA for the use of the excellently maintained stagnation flow reactor, as well as for the Mathematica script files for analysis of the data generated at the facility.

5.7 References

- [1] Stark JP. Solid State Diffusion: John Wiley & Sons, Inc.; 1976.
- [2] Young D. High Temperature Oxidation and Corrosion of Metals. Amsterdam, The Netherlands: Elsevier; 2008.
- [3] Birks N, Meier, G., Pettit, F. Introduction to the High-Temperature Oxidation of Metals. Cambridge, UK: Cambridge University Press; 2006.
- [4] Atkinson A. Transport processes during the growth of oxide films at elevated temperature. Reviews of Modern Physics. 1985;57:437-70.
- [5] Atkinson A, O'Dwyer ML, Taylor RI. ⁵⁵Fe diffusion in magnetite crystals at 500C and its relevance to oxidation of iron. Journal of Materials Science. 1983;18:2371-9.
- [6] Go KS, Son SR, Kim SD. Reaction kinetics of reduction and oxidation of metal oxides for hydrogen production. Int J Hydrogen Energy. 2008;33:5986-95.
- [7] Turkdogan ET, McKewan WM, Zwell L. Rate of Oxidation of Iron to Wustite in Water-Hydrogen Gas Mixtures. The Journal of Physical Chemistry. 1965;69:327-34.
- [8] Stehle RC, Bobek MM, Hooper R, Hahn DW. Oxidation reaction kinetics for the steam-iron process in support of hydrogen production. Int J Hydrogen Energy. 2011;36:15125-35.

[9] Loutzenhiser PG, Gálvez ME, Hischer I, Stamatiou A, Frei A, Steinfeld A. CO₂ Splitting via Two-Step Solar Thermochemical Cycles with Zn/ZnO and FeO/Fe₃O₄ Redox Reactions II: Kinetic Analysis. *Energy & Fuels*. 2009;23:2832-9.

[10] King DM, Spencer II JA, Liang X, Hakim LF, Weimer AW. Atomic layer deposition on particles using a fluidized bed reactor with in situ mass spectrometry. *Surface and Coatings Technology*. 2007;201:9163-71.

[11] Leskelä M, Ritala M. Atomic layer deposition (ALD): from precursors to thin film structures. *Thin Solid Films*. 2002;409:138-46.

[12] Scheffe JR, Francés A, King DM, Liang X, Branch BA, Cavanagh AS, et al. Atomic layer deposition of iron (III) oxide on zirconia nanoparticles in a fluidized bed reactor using ferrocene and oxygen. *Thin Solid Films*. 2009;517:1874-9.

[13] Scheffe JR, Allendorf MD, Coker EN, Jacobs BW, McDaniel AH, Weimer AW. Hydrogen Production via Chemical Looping Redox Cycles Using Atomic Layer Deposition-Synthesized Iron Oxide and Cobalt Ferrites. *Chem Mater* 2011;23:2030-8.

[14] Scheffe JR, McDaniel AH, Allendorf MD, Weimer AW. Kinetics and mechanism of solar-thermochemical H₂ production by oxidation of a cobalt ferrite–zirconia composite. *Energy & Environmental Science*. 2013.

[15] Muller C, Bohn C, Song Q, Scott S, Dennis J. The production of separate streams of pure hydrogen and carbon dioxide from coal via an iron-oxide redox cycle. *Chem Eng J* 2011;166:1052-60.

[16] Khawam A, Flanagan, D. Solid State Kinetic Models: Basics and Mathematical Fundamentals. *Journal of Physical Chemistry B*. 2006;110:17315-28.

[17] Galwey AK. Is the science of thermal analysis kinetics based on solid foundations?: A literature appraisal. *Thermochimica Acta*. 2004;413:139-83.

[18] Bamford CH, Tipper, C.F.H. *Comprehensive Chemical Kinetics: Volume 22 Reactions in the Solid State* Elsevier Scientific Publishing Company; 1980.

[19] Go K, Son, S., Kim, S. Reaction kinetics of reduction and oxidation of metal oxides for hydrogen production. *International Journal of Hydrogen Energy*. 2008;33:5986-95.

- [20] Loutzenhiser P, Galvez, M., et al. CO₂ Splitting via Two-Step Solar Thermochemical Cycles with Zn/ZnO and FeO/Fe₃O₄ Redox Reactions II: Kinetic Analysis. *Energy and Fuels*. 2009;23:2832-9.
- [21] Campo Ld, Perez-Saez RB, Tello MJ. Iron oxidation kinetics study by using infrared spectral emissivity measurements below 570 C. *Corrosion Science*. 2008;50:194 -9.
- [22] Ryu J-C, Lee D-H, Kang K-S, Park C-S, Kim J-W, Kim Y-H. Effect of additives on redox behavior of iron oxide for chemical hydrogen storage. *Journal of Industrial and Engineering Chemistry*. 2008;14:252-60.
- [23] Menzies I, Lubkiewicz, J. Oxidation of an Fe-12% NiAlloy in Oxygen at 700C-1000C. *Oxidation of Metals*. 1971;3:41-58.
- [24] Bajorek C, Nicolet, M., Wilts, C. Preferential Oxidation of Fe in Permalloy Films. *Applied Physics Letters*. 1971;82:82-4.
- [25] Bruckner W, Baunack, S., Hecker, M. et al. Oxidation of NiFe(20 wt.%) thin films. *Materials Science and Engineering B*. 2001;B86:272-5.
- [26] Sundar S, Deevi S. Isothermal oxidation behavior of FeCo-2V intermetallic alloy. *Intermetallics*. 2004;12:1311-6.
- [27] Lu F-H, Tinkler S, Dieckmann R. Point defects and cation tracer diffusion in (Co_xFe_{1-x})_{3-d}O₄ spinels. *Solid State Ionics*. 1993;62:39-52.
- [28] G.V.Lewis, Catlow CRA, Corma AN. Defect Structure and Migration in Fe₃O₄. *J PhysChem Solids* 1985;46:1227-33.
- [29] Peterson NL, Chen WK, Wolk D. Correlation and Isotope Effects for Cation Diffusion in Magnetite. *J Phys Chem Solids*. 1980;41:709-19.
- [30] Dieckmann R, Mason T, Hodge J, Schmalzried H. Defects and Cation Diffusion in Magnetite (III). Tracer diffusion of Foreign Cations as a Function of Temperature and Oxygen Potential Ber Bunsenges Phys Chem. 1978;82.

Chapter 6: A Thermodynamic Investigation of the Chemical Looping Hydrogen Process: Comparison of Novel Mixed Metal Oxides

6.1 Abstract

The mixed metal spinels CoFe_2O_4 and NiFe_2O_4 have been shown to produce about four times the amount of H_2 compared to conventional Fe-based materials during the CLH process in laboratory experiments. In addition, these mixed metal spinels have been shown to be capable of complete regeneration during steam oxidation unlike Fe-based materials. Materials with such improved properties could increase the flexibility of the CLH process, allowing more H_2 production than is currently possible with the Fe-based materials while maintaining the ability for electricity generation from supplemental O_2 oxidation. However, significant steam generation is required for full H_2O oxidation of CoFe_2O_4 and NiFe_2O_4 , raising the concern that the energy required to generate steam for oxidation will detract from the overall system efficiency. A model of the CLH process with Fe_2O_3 , CoFe_2O_4 , and NiFe_2O_4 was developed to investigate the material conversion in the bed before breakthrough of CO and H_2 , the product gas composition, the amount of H_2O necessary to fully oxidize the reduced material and steam-associated energy requirements, and the possibility of hybrid $\text{H}_2\text{O}/\text{O}_2$ oxidation for H_2 and electricity generation. The mixed metal spinel materials were found to be ideally suited for converting lower quality syngas (less than a 3:1 reducing gas/oxidizing gas ratio) to H_2 via lower temperature reactions.

6.2 Introduction

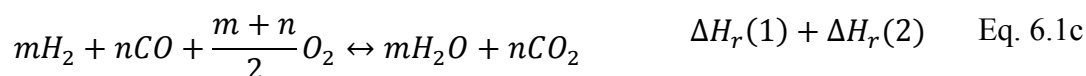
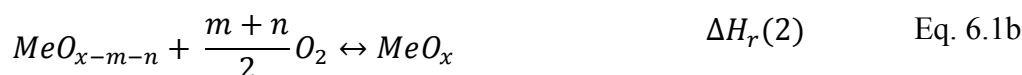
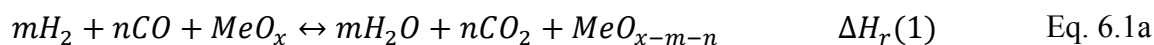
The CLH process allows the production of separate streams of pure H_2 and CO_2 from syngas without the use of energy intensive pressure swing adsorption or solvent-based gas

separation techniques. [1] The current state-of-the-art material for the CLH process, Fe_2O_3 , allows the production of pure H_2 in addition to electricity, as a H_2O oxidation step is followed with an O_2 oxidation step that produces significant amounts of heat. [2] This O_2 oxidation is necessary for Fe_2O_3 regeneration and leads to decreased H_2 recovery from the CLH process. The Fe-based CLH process has been shown to produce H_2 from syngas with an overall process efficiency of 68% and electricity with an energy conversion efficiency of 43% with integrated carbon capture. [3] The same study shows the energy conversion efficiency of H_2 production from coal with the WGS reaction at 58%, and the energy conversion efficiency of electricity production with the IGCC-Selexol system at 35%. Technologies to further the capability of the CLH process are important in advancing this attractive option for future H_2 and electricity production with integrated CO_2 capture.

Previous laboratory experiments show that the mixed metal oxides CoFe_2O_4 and NiFe_2O_4 produce about four times more H_2 per mass than Fe-based materials, allowing complete recovery of the H_2 and CO used to reduce the metal oxide. This increased H_2 recovery could give the CLH process the flexibility to generate exclusively H_2 , which Fe-based materials cannot do because of the necessary O_2 oxidation. Although the conversion of the solid in the bed has not been investigated for these materials, the increased H_2 production is assumed to be due to higher material conversions in the bed from the reduction of the Co and Ni cations to their metallic state, and the ability of CoFe_2O_4 and NiFe_2O_4 to completely regenerate under H_2O oxidation. Experiments verify the necessity of complete regeneration of the mixed metal spinel for high syngas conversions in the subsequent reduction step. The additional H_2 recovery for the CoFe_2O_4 and NiFe_2O_4 involves steam oxidation for a significantly longer time than for Fe-based

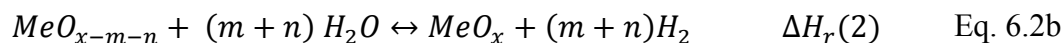
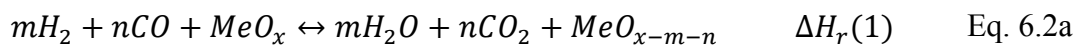
materials and may require more energy for steam production than is recovered from the H₂ produced and the heats of reaction.

The CLH process energetics are bracketed on one side by the CLC reaction energetics and on the others side by the water-gas shift reaction. In the CLC process, syngas (or methane) is used to reduce a metal oxide, and the metal oxide is subsequently oxidized with O₂. As Eqns. 6.1a-c show, the total heat evolved in the reduction and oxidation reactions is equal to the heat released from conventional combustion of the syngas. [4, 5]



The CLC process produces significant amounts of heat during the O₂ oxidation of the reduced metal oxides (>-250 kJ/mol H₂/CO consumed), which is used to drive a steam turbine/gas turbine system for electricity generation. [3] The reduction of metal oxides with H₂, CO, and CH₄ can be endothermic or exothermic, and the magnitude depends greatly upon the syngas composition, the metal oxide material, and the reaction temperature. However, the heats of reaction for reduction are usually small in comparison to the heats of reaction of O₂ oxidation. [6]

The complete H₂O oxidation of the reduced metal oxide gives the energetics of the WGS reaction, as shown in Eqns. 6.2 a-c. [7]



The heat of reaction for the reduction of the metal oxide is the same as for the reduction step of the CLC process and depends greatly on the composition of the syngas. The H₂O oxidations of reduced metal oxides are usually slightly exothermic, and the overall WGS reaction has a value of about -30 kJ/mol in the CLH process temperature range. Since the desired product in this process is H₂ rather than heat, the lack of heat generation is only troubling when the energy to produce steam for oxidation is significantly greater than the energy content of the H₂ that is produced and the heat recovered from the reduction and oxidation reactions. For example, with the Fe-based system, the conversion of H₂O to H₂ is nearly 60% for the H₂O oxidation of Fe to FeO at 1073 K, making it a process that requires only moderate excess steam generation. [8] Oxidation of Fe₃O₄ to the Fe₂O₃ phase with H₂O produces less than 1 x 10⁻⁷ moles of H₂ per mole of H₂O fed, so O₂ is used for re-oxidation because this reaction is not feasible for H₂ production. [1]

As shown in Chapter 3, the metal oxides CoFe₂O₄ and NiFe₂O₄ have a unique equilibrium value for each Fe-rich spinel composition rather than one H₂/H₂O ratio at which Co/Ni and Fe₃O₄ are oxidized to form the mixed metal spinel. The H₂/H₂O ratios range from 1 to 10⁻⁶ in this composition range at 873 K, which allows between 50% and 10⁻⁶% conversion of the steam to H₂. The mixed metal oxides can be regenerated with supplementary O₂ when H₂ production is no longer efficient, as with the Fe-based system. This O₂ oxidation is predicted to be highly exothermic and would allow electricity generation in addition to H₂ generation. The overall energetics of this process will depend on the syngas composition, the metal oxide

material, the temperature of reaction, and the material conversion at which H₂O oxidation is stopped and O₂ oxidation begins. Analyzing the balance between H₂O and O₂ oxidation for these materials is requisite in determining how viable CoFe₂O₄ and NiFe₂O₄ are for use in a CLH process.

Due to the complex nature of the reactions and the resulting conversion of the solid material in the reactor, a system model is necessary to evaluate the energy balances for the reduction and oxidation reactions in the CLH system. [8] In addition to modeling the H₂O and O₂ oxidations of reduced material, the model must be capable of predicting the amounts of CO and H₂ that can be consumed before breakthrough during reduction to obtain the conversion of the material in the reactor at the beginning of the oxidation step. Such a model would allow an investigation of the effects of syngas composition, reaction temperature, metal oxide, and H₂O and O₂ oxidations on the material conversion, H₂ production, and overall energy efficiency of the CLH process. Modeling the entire gasification and electricity generation system would provide more insight into the overall efficiency of the CLH process coupled with a gasifier; however, this study seeks only to examine the materials used in the CLH process. We believe a comparison of the mixed metal oxide performance with that of the widely accepted Fe₂O₃ in the CLH reactor is sufficient to establish viability, assuming that all other system components remain the same between the Fe-based material and the mixed metal oxides.

This investigation seeks to develop and validate such a model of the CLH system, and then use the model to evaluate a range of operating conditions for the CLH process with Fe₂O₃, CoFe₂O₄ and NiFe₂O₄. The model will be validated against predictions from FactSage and experimental results from a laboratory packed bed reactor to ensure accuracy in approximating the CLH process. The investigation will allow us to probe the nature of solid conversion in the

reactor before breakthrough as a function of gas/solid ratio and its relationship to H₂ production, which is of interest due to the significantly higher H₂ production observed for mixed metal oxides than for Fe₂O₃. The model will allow investigation into the total amount of steam required to fully oxidize the solid material and the associated energy requirements to determine if complete H₂O oxidation is feasible. The possibility of hybrid H₂O/O₂ oxidation will be explored for combined H₂ and electricity production using the mixed metal oxides.

6.3. Materials and Methods

6.3.1. Mathematical Model of the Chemical Looping Hydrogen Process

The mathematical model of the system was developed in MATLAB and encompasses the reduction reactions, oxidation reactions, and the steam generation for the oxidation. Energy balances for gas cooling for condensation of H₂O from the streams exiting the reduction and oxidation reactors have been calculated but are not reported due to their dependence on the type of equipment used and placement in a larger system. Figure 6.1 shows the CLH schematic with only H₂O oxidation, and Figure 6.2 shows the CLH schematic with a supplementary O₂ oxidation step.

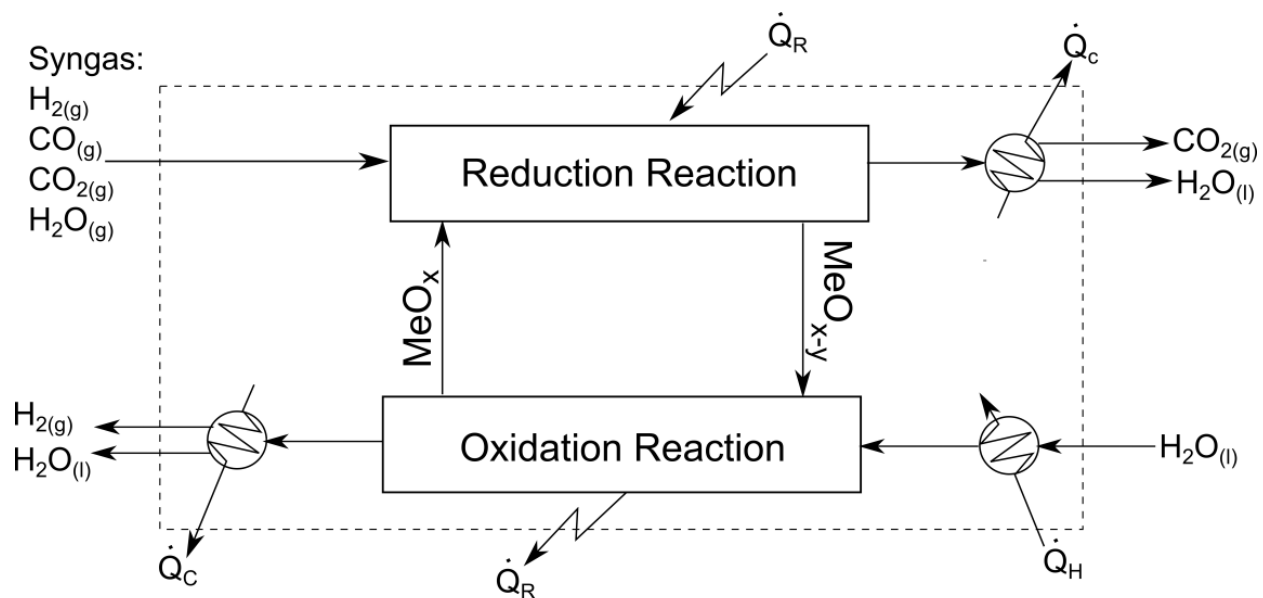


Figure 6.1: Process schematic for the model operating with only H₂O oxidation.

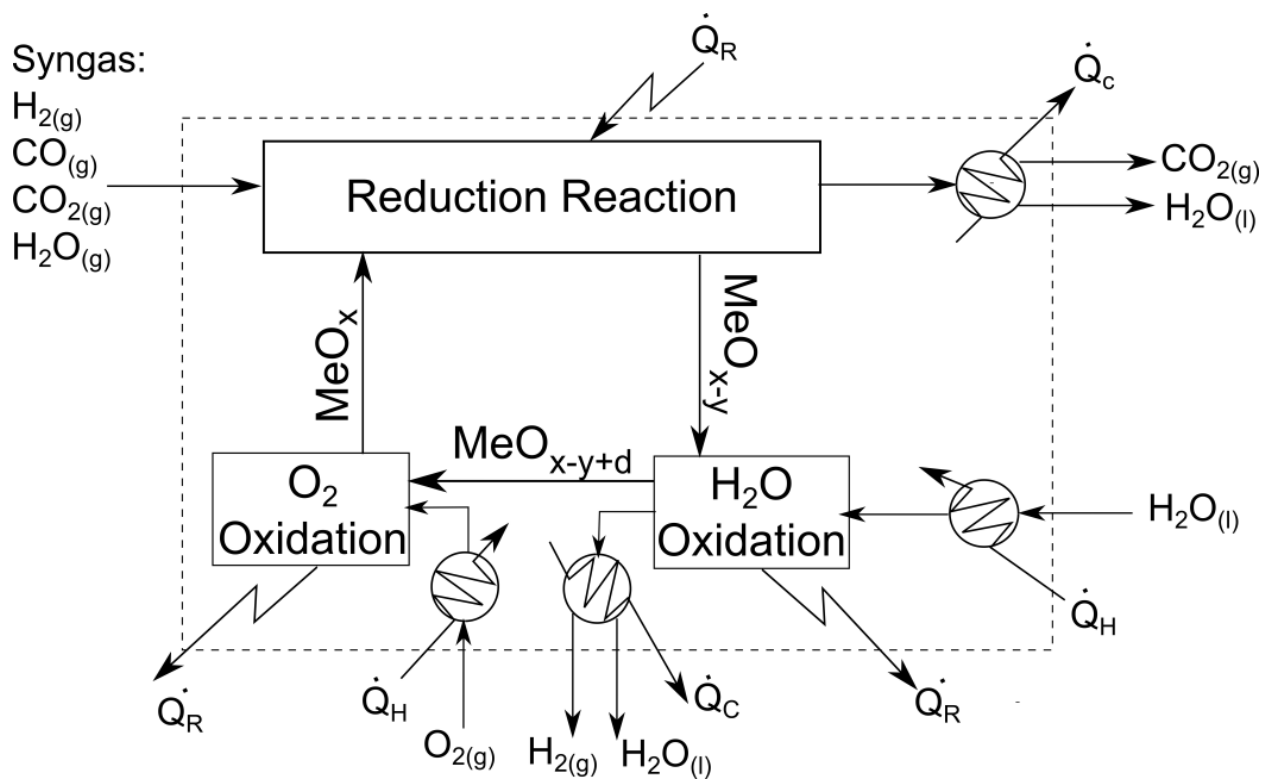


Figure 6.2: Process schematic for the model operating with both H₂O and O₂ oxidation.

Key model assumptions are listed in Table 6.1. The packed bed reactor is modeled as a series of CSTR segments in which gas-solid equilibrium is reached between the H₂/H₂O and CO/CO₂ systems and the solid phases in the reactor. The equilibrium conditions in each segment are a function of the reaction temperature, initial gas composition, and the conversion of the material in the bed and are discussed in section 6.3.2. [9]

Model Assumptions:	
1)	Clean, particulate- and tar-free syngas enters the reactor at the reaction temperature without any additional heating or cooling.
2)	Both the reduction and oxidation reactions have sufficient heating or cooling to operate isothermally.
3)	Reactions of H ₂ and CO with the solid proceed simultaneously and independently and reach equilibrium. The resulting gas then reacts to WGS equilibrium.
4)	The forward reaction, reverse reaction, and the water-gas shift reactions are all considered in the reactor.
5)	Equilibrium conditions are for H ₂ , H ₂ O, CO, CO ₂ , and the solid phases only. No solid carbon or hydrocarbon formation is considered.

Table 6.1: List of key assumptions made in development of MATLAB model

6.3.2 FactSage Calculations

Temperature dependent equilibrium solid and gas compositions for the Fe-only, Fe-Co, and Fe-Ni CLH systems were investigated using FactSage (Version 6.2), which uses Gibbs free energy minimization calculations and extensive thermodynamic property databases for thermodynamic modeling. Multiple studies show the FactSage program correctly models the phase and composition of mixed metal spinels during thermal reduction and H₂O oxidation. [10, 11] Including solution phases from the FactSage oxide solution database (version 5.3) in thermodynamic calculations, rather than only stoichiometric line compounds, significantly affects the accuracy of the thermodynamic calculations. [10] FactSage is able to reproduce thermodynamic properties, activities, M²⁺/M³⁺ ratios, solution sublattice cation distributions, and

partial pressures of equilibrium gases from compiled experimental data using these databases. [12]

In addition to pure solids and gases from the Fact 5.3 database, spinel, metal oxide and alloy solution phases were included for this study. The FactSage spinel solution phase uses the compound energy formalism model to describe the distribution of cations over spinel tetrahedral and octahedral sites. Vacancies in the octahedral sublattice allow oxygen non-stoichiometry and deviations from the ideal 2+/3+ cation ratio in the spinel phase model $(\text{Fe}^{2+}, \text{Fe}^{3+}, \text{M}^{2+}, \text{M}^{3+})^{\text{T}}[\text{Fe}^{2+}, \text{Fe}^{3+}, \text{M}^{2+}, \text{M}^{3+}, \text{Va}]_2\text{O}_4$. [13] The metal oxide solution phase is modeled as a random solution of M^{+2} , Fe^{+2} , and Fe^{+3} ions on cation sites. Vacancies associated with Fe^{+3} ions on cation sites allow for excess Fe cations in the wustite (Fe_{1-x}O) phase. [10, 14] These models allow the calculation of the Gibbs energy of each possible reaction product in the solution phase as a function of T, P and composition, and have been optimized over the temperatures and compositions examined in this chapter and validated by reproducing several thermodynamic datasets from literature. [12, 15]

FactSage uses a Gibbs energy minimization technique to identify the most probable reaction products at equilibrium given a set of constraints. The equation

$$G = \sum_{\substack{\text{ideal} \\ \text{gas}}} n_i(g_i^{\circ} + RT\ln P_i) + \sum_{\substack{\text{pure} \\ \text{condensed} \\ \text{phases}}} n_i g_i^{\circ} \quad \text{Eq. 6.3}$$

$$+ \sum_{\text{solution}_1} n_i(g_i^{\circ} + RT\ln X_i + RT\ln \gamma_i) + \sum_{\text{solution}_2} n_i(g_i^{\circ} + RT\ln X_i + RT\ln \gamma_i) + \dots$$

where

$$n_i = \text{moles}$$

P_i = gas partial pressure

X_i = mole fraction

γ_i = activity coefficient

g_i^0 = standard molar Gibbs Energy

is minimized by determining the combination of n_i , P_i , and X_i in the system. FactSage was used to construct phase diagrams for the Fe-O, Co-Fe-O, and Ni-Fe-O systems at temperatures between 673 K and 1173 K to identify the equilibrium solid composition as a function of the partial pressure of O₂ (p_{O_2}). The solid composition and p_{O_2} data were then used in the model to determine the amount of oxygen exchange between the solid and gas phases to reach equilibrium, along with the resulting reaction products in each reactor segment.

6.3.2.1 Fe-O system

The gas-solid equilibrium for the binary Fe-O system as a function of temperature and p_{O_2} is shown in Figure 6.3. The y axis, $\log_{10}p(O_2)$, is the partial pressure of O₂, which is related to the H₂/H₂O and CO/CO₂ systems by the relationships:



If the amounts of CO₂ and CO or H₂O and H₂ in a gas mixture are known, then the p_{O_2} can be calculated with knowledge of the temperature dependent equilibrium constant for the Eq. 6.4a or b, and the overall pressure, using Equation 6.5:

$$K p_O = \exp\left(-\frac{\Delta G^\circ}{RT}\right) = \frac{p_{CO} p_{O_2}^{\frac{1}{2}}}{p_{CO_2}} \quad \text{Eq. 6.5}$$

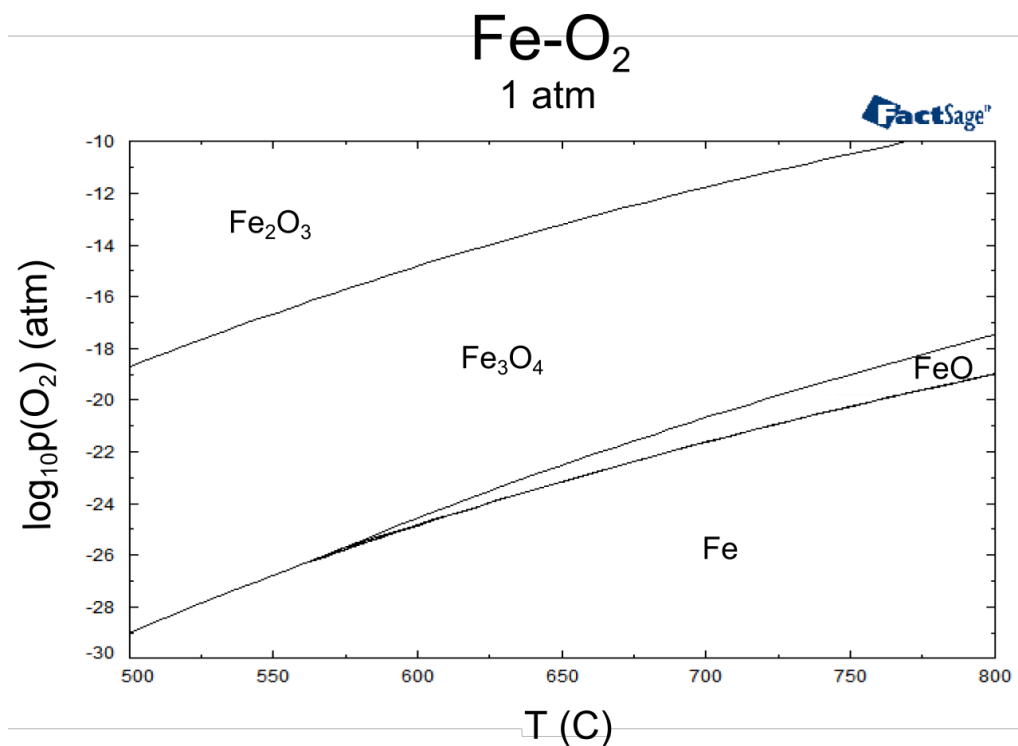


Figure 6.3: Composition of solid in the Fe-O binary system as a function of temperature and p_{O_2}

The lines in Fig. 6.3 show the oxygen partial pressures at which the reactions in Eq. 6.6-6.9 take place:



Figure 6.3 is the same as Figure 6.4, which commonly appears in CLH literature. [1, 2] The $p_{\text{CO}_2}/p_{\text{CO}}$ and $p_{\text{H}_2}/p_{\text{H}_2\text{O}}$ values on the left and right axes correspond to the p_{O_2} values from Figure 6.3 using equation 6.5. For example, at 773 K (500°C), the p_{O_2} at equilibrium between Fe and Fe_3O_4 is 10^{-29} . From Figure 6.4, the equilibrium constant between Fe and Fe_3O_4 at 773 K is 0.3 for the $\text{H}_2/\text{H}_2\text{O}$ system and 1.5 for the CO/CO_2 system. At 773 K, a gas with $p_{\text{H}_2\text{O}}/p_{\text{H}_2}$ ratio of 0.3 has an O_2 partial pressure of 2×10^{-29} , which is the $\log_{10}(p_{\text{O}_2})$ value predicted in Figure 6.3. A gas with a $p_{\text{CO}_2}/p_{\text{CO}}$ value of 1.5 at 773 K has an O_2 partial pressure of 1.5×10^{-29} , which also correlates with the $\log_{10}(p_{\text{O}_2})$ predicted in Figure 6.3. Mixtures of $\text{H}_2/\text{H}_2\text{O}$ and CO/CO_2 are commonly used to achieve the low p_{O_2} values necessary for oxidation of metals and metal oxides. [16]

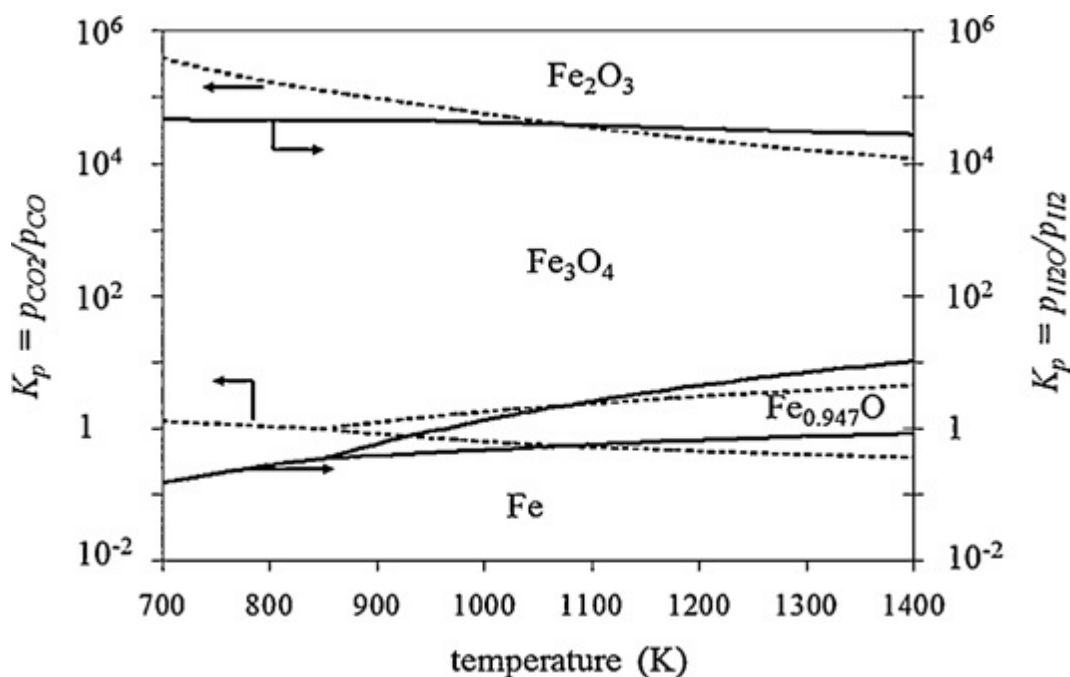
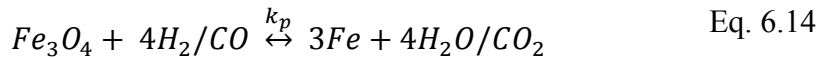
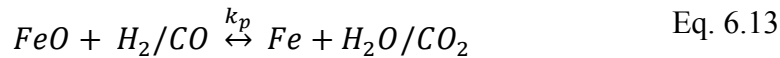
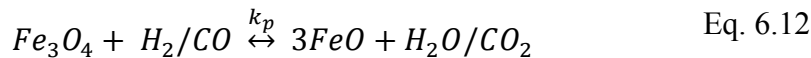
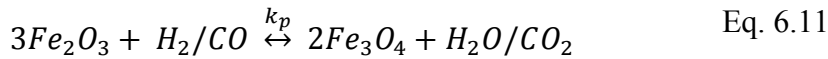


Figure 6.4: Equilibrium for the Fe-CO-CO₂ and Fe-H₂-H₂O system. From Muller *et al.* Chemical Engineering Journal; 2011:166 [17]

The lines in Figure 6.4 give the equilibrium constants (K_p) for the oxidation and reduction reaction in the Fe – H₂ – H₂O and Fe – CO – CO₂ systems. For example, a gas with a p_{CO_2}/p_{CO} ratio of 0.1 would reduce Fe₃O₄ at 700 K until either the gas composition reaches the composition shown by the line between the Fe and Fe₃O₄ phases (about 1) and would leave a mixture of Fe₃O₄ and Fe, or would reduce until only Fe remained if the solid was the limiting reactant. Using the data from Figure 6.3, the gas composition and solid composition in each reactor segment were evaluated to determine if a reaction was predicted, and, if so, the final composition was calculated based on the limiting reactant. In the Fe-O system, each component is a pure compound with an activity of 1, allowing the simplified equilibrium constant to be

$$K_p = \frac{p_{CO_2}}{p_{CO}} \text{ or } \frac{p_{H_2O}}{p_{H_2}} \quad \text{Eq. 6.10}$$

The following reactions involving only H₂, H₂O, CO, CO₂, and the solid metal oxide phases, are included in the model:



6.3.2.2 Fe-Co-O and Fe-Ni-O systems

The ternary Co-Fe-O and Ni-Fe-O systems are more complex than the Fe – O system and contain two-phase regions of solid solutions of mixed metal spinels, metal oxides (MeO – FeO, CoO, NiO), metallic and alloy phases. The constant temperature and constant pressure

equilibrium distribution of solid phases for each Fe-Co-O composition, calculated from Gibbs free energy minimization, can be expressed in a phase diagram as shown in Figure 6.5. The dotted line marks the Fe/(Fe+Co) ratio for a material with a 2:1 Fe:Co, and an analysis at each point gives the equilibrium solid composition under the specified conditions. At low O mole fractions, a metal/alloy phase and a spinel phase are present. The composition transitions to spinel and Fe₂O₃ as the O mole fraction increases.

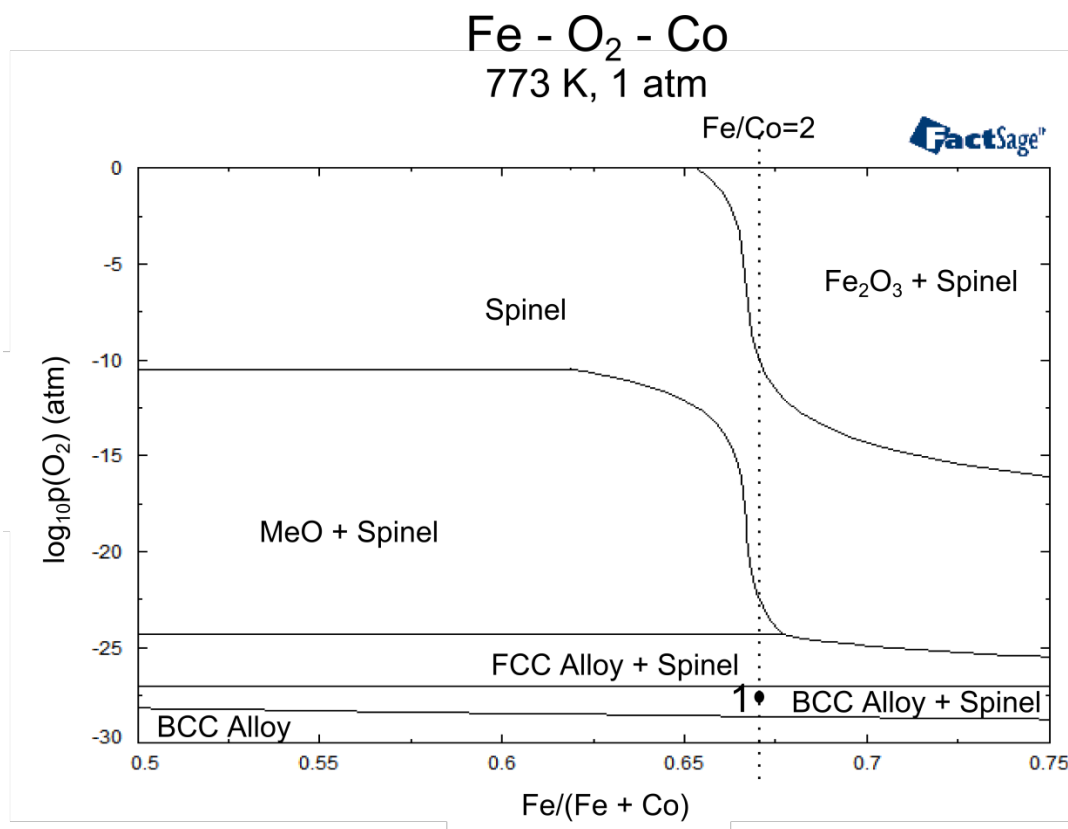


Figure 6.5: Phases present for the Fe-Co-O system under varying pO_2 .

The relative amounts and compositions of the solid phases at equilibrium can be calculated along the 2:1 Fe:Co line using tie lines and the lever rule or, if available, software. For example, at point 1 in Figure 6.5, the overall system mole fractions are 0.28 O, 0.48 Fe and

0.24 Co. The equilibrium solid distribution at this composition is 0.25 moles Fe and 0.24 moles Co in the BCC phase, and 0.23 moles Fe and 0.28 moles O in the spinel phase. As before, the $\log_{10}p(\text{O}_2)$ can be easily converted to $p\text{CO}_2/p\text{CO}$ or $p\text{H}_2\text{O}/p\text{H}_2$, allowing the determination of the relationship between gas composition and the solid phases present in the material. These equilibrium solid compositions were calculated for each $p\text{O}_2$ value along the 2:1 Fe:Co line shown in Figure 6.5. Resulting data describing the amount and composition of each solid phase were used in the model to determine the oxygen exchange between the gas and the solid phase and the equilibrium solid composition in each reactor segment.

For example, if 1 mole of solid with a composition at point 1 in Figure 6.5 was contacted with 1 mole of gas with a $p\text{H}_2\text{O}/p\text{H}_2$ value of 10 at 773 K, the $\log_{10}p(\text{O}_2)$ value would be 10^{-26} . The equilibrium solid phases under these conditions are FCC alloy and spinel, while the solid phase in the segment is a BCC alloy and spinel. The solid material would oxidize under these conditions, increasing the O in the solid phase while the Fe:Co ratio remained 2:1, and the $\log_{10}(p\text{O}_2)$ value would decrease along with the amount of H_2O in the gas phase. An iterative approach was used to determine simultaneous small changes in both the gas and solid compositions. Iterations continued until the new gas composition was in equilibrium with the new solid composition. In these calculations the $\log_{10}(p\text{O}_2)$ values are treated as pseudo-equilibrium constants, as they allow the determination of equilibrium solid phases present with a given gas composition but do not contain explicit information regarding the activity of the solid solutions in the material. The same process was applied to the Ni-Fe-O system to determine the applicable equilibrium conditions.

6.3.3 Model Development

Simultaneous solid reaction with CO and H₂ were modeled, with each component reaching equilibrium with the solid phase independently. Oxygen balances were performed for each segment using Equations 6.15a-c and 6.17a-c and conditions regarding the relevant equilibrium conditions based on the gas composition and the oxygen available in the solid.

$$\frac{H_2O_i + x_H}{H_{2,i} - x_H} = K_{eq,H} \quad \text{Eq. 6.15a}$$

$$\frac{CO_{2,i} + x_C}{CO_i - x_C} = K_{eq,C} \quad \text{Eq. 6.16a}$$

$$H_2O_f = H_2O_i + x_H \quad \text{Eq. 6.15b}$$

$$CO_{2,f} = CO_{2,i} + x_C \quad \text{Eq. 6.16b}$$

$$H_{2,f} = H_{2,i} - x_H \quad \text{Eq. 6.15c}$$

$$CO_f = CO_i - x_C \quad \text{Eq. 6.16c}$$

$$O_{solid,f} = O_{solid,i} - x_H - x_C \quad \text{Eq. 6.17}$$

The conversions of the H₂ (x_H) and CO (x_C) were determined from the conditions described in sections 6.3.2 and were used to calculate the equilibrium amounts of H₂, CO, H₂O, CO₂, and oxygen in the solid.

All reactors shown schematically in Figure 6.1 and 6.2 are assumed to have sufficient heating or cooling to operate isothermally. Syngas entering the reactor was assumed to be at the temperature of reaction and free of any particulate matter or tars. The reduction reaction was assumed to reach equilibrium conditions; gas exiting a segment is in equilibrium with the solid material in the segment. For example, the reduction of Fe₃O₄ to FeO with H₂ has an equilibrium constant of 0.97 at 923 K, meaning that gas with an H₂O/H₂ ratio greater than 0.97 will reduce Fe₃O₄ until the H₂/H₂O ratio is 0.97 or until the metal oxide is completely converted to FeO and no further O can be removed from the solid. Gas with an H₂O/H₂ ratio greater than 0.97 will flow over the Fe₃O₄ without changing the gas or solid composition. The assumption that the

materials reach equilibrium implies that the reactions have rapid enough kinetic rates that equilibrium is reached in the time that the gas is in contact with the solid. Based on the previous laboratory experiments showing nearly complete conversion of H_2 and CO for the Fe_2O_3 , $CoFe_2O_4$, and $NiFe_2O_4$ materials during the first two to three minutes of reduction (detailed in Chapter 4), as well as analysis by other researchers showing near-equilibrium gas conversions during experiments, we believe this assumption is valid at low to moderate solid conversions.

[9]

The gas phase water-gas shift reaction was assumed to reach equilibrium in this model due to its relatively rapid kinetics at temperatures above 873 K and the propensity of Fe, Co, and Ni as WGS catalysts. [18] In a reactor, the gas-solid reactions and the WGS reactions would happen simultaneously; however, in this model the WGS reaction is considered after gas-solid equilibrium is reached. The $CoFe_2O_4$ and $NiFe_2O_4$ materials were assumed to reduce as FactSage predicts, first to Co/Ni and Fe_3O_4 , then to reduce to Fe. We believe this assumption to be valid based on the XRD and Raman data from reacted samples, shown in Chapter 3. Equilibrium and enthalpy of reaction values for each reaction considered were obtained in the temperature range of 673-1273 K from the thermodynamic databases in FactSage.

During the oxidation reaction, the gas phase was also assumed to be in equilibrium with the solid phase; however, only the H_2/H_2O equilibrium is considered. In the reactor, the reverse reaction is also implemented since the H_2/H_2O may be high enough from oxidizing materials at the beginning of the reactor to reduce materials with lower conversions near the end of the reactor. For example, the equilibrium constant for oxidation of Fe to FeO at 973 K is 2.43. Steam in contact with Fe in the reactor will react until the H_2/H_2O ratio is 2.43, or until the Fe is fully oxidized to FeO; however, any Fe_3O_4 remaining in the bed will be reduced at H_2/H_2O ratios

greater than 1.1. The assumption of thermodynamic equilibrium during oxidation is made to allow us to analyze the “best case” scenario for the system since oxidation kinetics may depend greatly on the method of material preparation. Energy for steam generation was calculated using the standard temperature dependent heat capacities of liquid H₂O and steam, and heat of vaporization for H₂O that were obtained from the FactSage thermodynamic databases.

6.4 Sample Preparation and Reactor for Experimental Validation

Experiments in a packed bed reactor were used to validate the H₂ and CO conversions during the reduction reaction step and overall H₂ production during subsequent H₂O oxidation. The reactor and metal oxide sample preparation described here are addressed in detail in Chapter 4.

6.4.1 Sample Preparation

Samples of Fe₂O₃, NiFe₂O₄, and CoFe₂O₄ were prepared via the incipient wetness method from iron nitrate (Fe(NO₃)₃ · 9H₂O, Sigma Aldrich, 98%), nickel nitrate (Ni(NO₃)₂ · 6H₂O, Alfa Aesar, 98%), and cobalt nitrate (Co(NO₃)₂ · 6H₂O, Alfa Aesar, 98%). [19, 20] Crushed catalyst pellets made of approximately 20 nm sintered ZrO₂ spheres (Alfa Aesar, 99%, 0.31 cm³/g, 50 m²/g), were sieved to 110 – 175 μm diameter particle size and subsequently mixed with the aqueous metal nitrate solutions of the desired stoichiometry. Samples were calcined at 873 K in air for eight hours once 30% by mass of metal oxide was reached. Sample mass loadings and deposited cation ratios were confirmed via inductively coupled plasma-atomic emission spectroscopy (ICP-AES) and phase identification was performed using X-Ray diffraction (XRD, Scintag PAD5 Powder Diffractometer, CuKα1 radiation, λ=0.15406 nm, scan rate 0.5°/min, step size 0.02°).

6.4.2 Packed Bed Reactor

Approximately 250 mg of sample material were placed on top of ZrO_2 spheres inside an alumina reactor tube to form a bed of active material. The tube was placed in a horizontal furnace constructed using a 1.27 cm OD/0.95 cm ID (0.5" OD/0.375" ID) Al_2O_3 tube wrapped in nichrome wire secured using a high temperature ceramic epoxy and wrapped in insulation. An Omega CNI16 process controller module was used to control the temperature of the reactor, which was monitored using a thermocouple placed between the furnace tube and the Al_2O_3 reactor tube.

Calibrated MKS 1179A mass flow controllers delivered gases to the system. A New Era NE-1000 syringe pump delivered water to heated coils and a stream of Ar carrier gas to generate steam for the oxidation step. A constant stream of Ar purged the reactor before and after delivery of reactant gases. The reducing syngas mixture and oxidizing steam mixture equilibrated on a separate pressure controlled reactor bypass line for fifteen minutes prior to introduction contact with the sample. Upon completion of each reaction step, the Ar purge immediately resumed. A column of drierite removed H_2O from the gas stream before the mass spectrometer. Pressure controllers and a vacuum pump maintained a constant pressure on the bypass and reactor lines, and the bypass line pressure controller monitored the upstream pressure during the reactions.

A downstream absolute pressure of 81.3 ± 0.03 kPa (610 ± 0.2 Torr) was maintained during reduction and oxidation of the sample. A flowrate of 24 sccm of syngas and steam in argon created a 13 - 20 kPa (100-150 Torr) pressure drop across the reactor. Reduction and oxidation reactions were performed at a furnace temperature of 873 ± 1.5 K. Steam production

occurred at 383 K by injecting 0.006 mL/min of H₂O into 20 sccm of Ar in heated coils. The resulting mixture was 30% steam in Ar. All gas lines were maintained at a temperature of 293 K to avoid condensation of H₂O before the drierite column. Oxidations continued until H₂ levels returned to their baseline as measured before reaction.

6.4.2 Gas Composition and Analysis

A Stanford Research Systems QMS 200 mass spectrometer monitored reaction products in each experiment. Five point calibrations, performed each day for H₂, CO, and CO₂, covered the gas parts-per-million (ppm) ranges observed in reactor operation. Two different syngas compositions were used in reduction; a 10% H₂, 10% CO, 13% CO₂ in Argon mixture and an 8% H₂, 8% CO, 30% CO₂ in Argon mixture.

6.5 Results and Discussion

6.5.1 Model Validation

Model results were compared with FactSage predictions to verify correctness of calculations, and then with laboratory experiments to confirm accurate approximation of the CLH system.

First, to ensure model results were in accord with thermodynamic predictions from FactSage, the same conditions were evaluated in both the MATLAB model and with FactSage predictions. The FactSage Equilibrium module functions as a batch reactor, in which solid and gas are in direct contact and change composition until gas-solid equilibrium is reached without any material leaving the reactor. A batch reactor predicts significantly lower conversions than would be observed in a packed bed, because in a packed bed gasses that inhibit the forward reaction are swept away and replaced with gasses that are farther away from equilibrium. As

with the MATLAB model, in FactSage a packed bed reactor can be simulated with a series of reactor “segments” in which small amounts of solid and gas are allowed to reach equilibrium, after which the gas is moved to the next segment and the solid is contacted with the gas from the previous segment. [8]

For both FactSage and the model, total moles of metal oxide were divided into five segments for the calculation to simulate five reactors in series (see Figure 6.3). A model with a higher number of segments was tested, but gave results equivalent to the five-segment model. An amount of syngas equal to the moles of metal oxide was contacted with the solid in each segment, but divided into five portions, or “time steps”, to simulate the flow over a period of time. FactSage calculations were completed in the Equilibrium module, and solid streams were recycled for each timestep to carry the products from the previous timestep to the subsequent one. The CLH MATLAB model was run in a similar manner, but solid recycle was not necessary due to the ability to store the solid phase products at each timestep. Results from the model for timesteps 1 through 3, before breakthrough of H₂ and CO was observed for Fe₂O₃, are shown with results from FactSage in Figure 6.6. Conversions of H₂ and CO

$$X_H = 1 - \frac{H_2}{H_2 + H_{2O}} \quad \text{Eq. 6.18}$$

$$X_C = 1 - \frac{CO}{CO + CO_2} \quad \text{Eq. 6.19}$$

in each segment are shown at timesteps 1 through 3, and illustrate the decreased ability of reacted solid to convert CO to CO₂ and H₂ to H₂O. Nearly identical values were calculated using FactSage and the CLH MATLAB model. Similarly, the solid conversion

$$X_M = 1 - \frac{\text{Moles } O_{final}}{\text{Moles } O_{initial}} \quad \text{Eq. 6.20}$$

at timestep 5 showed nearly identical predictions from both FactSage and the CLH MATLAB model.

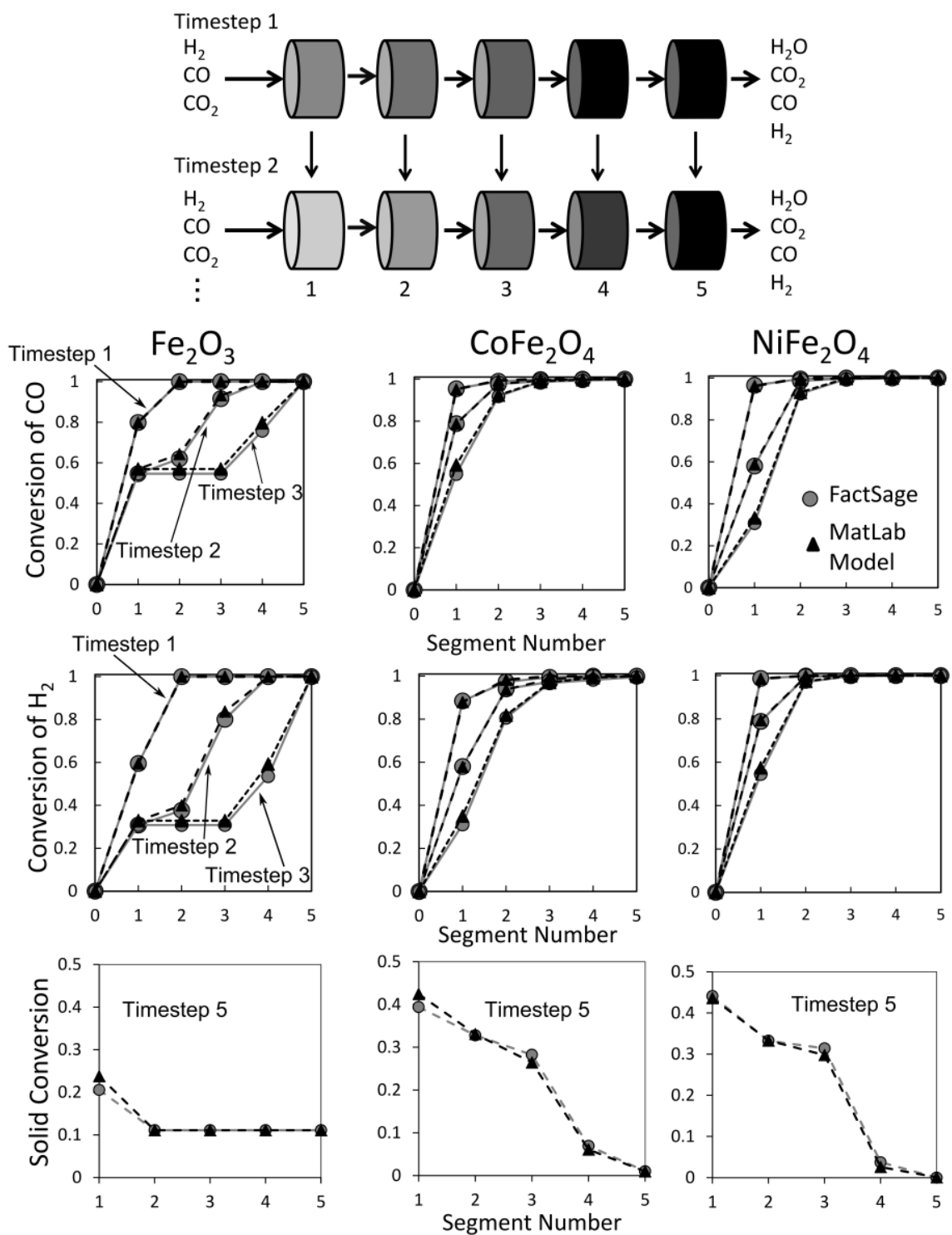


Figure 6.6: Model predictions for gas and solid conversions in the packed bed in comparison to FactSage predictions.

To verify the heats of reaction from the model, the total heats of reaction associated with syngas reduction and O_2 or H_2O oxidations were calculated. In the case of O_2 oxidation, the heat of reaction was compared with the energy of combustion for the syngas, as shown in Eq. 6.1. The heat of reaction for the complete oxidation with H_2O was compared with the WGS reaction, as shown in Eq. 6.2. In all cases, the heats of reaction from the model were within 3% of the calculated combustion and WGS reaction energies.

Packed bed reactor experiments were conducted using the same total moles of metal oxide, syngas composition, and temperature as modeled in both FactSage and MATLAB. Reductions lasted for three minutes, followed by a reactor purge and H_2O oxidation. Breakthrough of H_2 and CO was not observed during the reduction step for $CoFe_2O_4$ and $NiFe_2O_4$, but was seen for the Fe_2O_3 material between two and three minutes of reduction. Model predictions under the same material conditions showed no breakthrough during three minute reductions of $CoFe_2O_4$ and $NiFe_2O_4$, but breakthrough occurred in the last minute of the Fe_2O_3 reduction. Measured H_2 production during H_2O oxidation matched the predicted H_2 production closely, as shown in Figure 6.7. Equivalent H_2 production from the reactor and the model, in combination with nearly 100% conversion of the H_2 and CO in the syngas observed in experiments during the reduction step, confirm that the assumption of equilibrium during the reduction step is reasonable under these conditions.

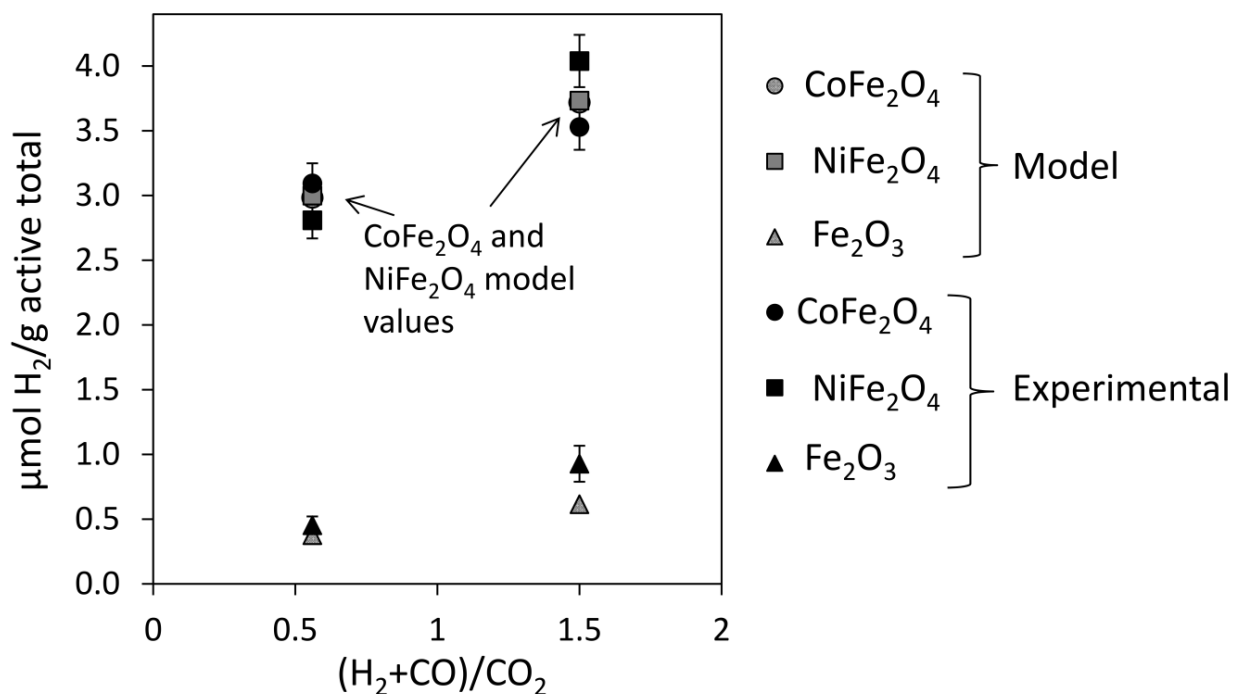


Figure 6.7: Model H₂ predictions and H₂ production from laboratory packed bed reactor experiments.

6.5.2. Model Results and Analysis

6.5.2.1. Solid Conversion

The packed bed reactor experiments in Chapter 4 showed significantly higher H₂ production from CoFe₂O₄ and NiFe₂O₄ materials than from Fe₂O₃ under the same conditions. We proposed this additional H₂ generation to result from a combination of the ability of the mixed metal ferrites to be reduced under lower H₂/H₂O and CO/CO₂ ratios, and the recovery of all the H₂ and CO used in the reduction step as H₂ during H₂O oxidation using the mixed metal ferrites. An examination of the predicted metal oxide conversion in the reactor from the model allowed us to investigate the solid conversion for each material and the resulting H₂ production.

Figures 6.8 and 6.9 show the conversion of the material in the bed at syngas breakthrough for two different syngas compositions (1:1 reducing gas to oxidizing gas and 3:1 reducing gas to oxidizing gas, referred to as “1:1 syngas” and “3:1 syngas”) at 873 K and 1073 K. The total moles of oxygen in the metal oxide materials were the same for each test (135 mol O). These simulations investigated material behavior normalized by available O in the solid, but in a pilot or test-scale system, a mass- or volume-based metric would be more applicable. The conversion of the solid is calculated as before

$$X_M = 1 - \frac{\text{Moles } O_{\text{final}}}{\text{Moles } O_{\text{initial}}} \quad \text{Eq. 6.21}$$

where moles O_{final} is moles of oxygen in the solid and moles O_{initial} is moles of O initially in the solid. For Fe_2O_3 , a conversion of 11% gives Fe_3O_4 , a conversion of 33% gives FeO, and a conversion of 100% gives Fe metal. For NiFe_2O_4 and CoFe_2O_4 , a conversion of 33% gives a mixture of Co or Ni metal and Fe_3O_4 , while a conversion of 50% gives a mixture of Co or Ni metal and FeO. A conversion of 100% gives metallic Fe and Co or Fe and Ni. The metal oxide’s capacity for oxidizing H_2 and CO to H_2O and CO_2 before H_2 and CO breakthrough, R , is expressed as

$$R = \frac{M_{\text{Solid},T}}{M_{\text{Gas},B}} \quad \text{Eq. 6.22}$$

where $M_{\text{Solid},T}$ is the total moles of Fe_2O_3 , NiFe_2O_4 or CoFe_2O_4 in the reactor and $M_{\text{gas},B}$ is the total moles of syngas through the reactor at breakthrough. A lower R value translates to fewer moles of solid necessary per mole of syngas reacted, and would likely require smaller reactor sizes for the same syngas throughput.

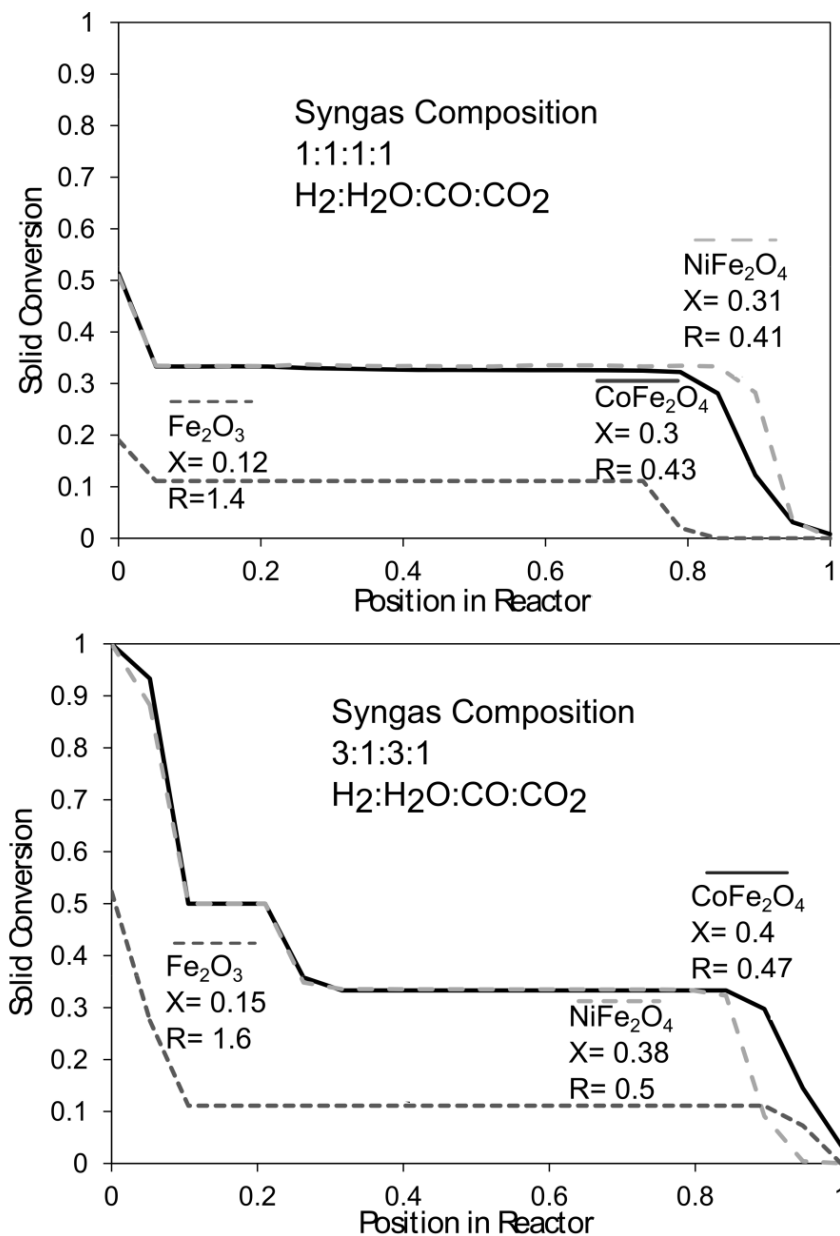


Figure 6.8: Conversion of solid materials at syngas breakthrough at 873 K for each metal oxide type under two different syngas compositions. X values are material conversion and R-values are the ratio of moles of solid in the bed to moles of syngas through the reactor at breakthrough.

Figure 6.8 shows the pre-breakthrough solid conversion for Fe_2O_3 is much lower than for the mixed metal oxides at 873 K. The 1:1 syngas composition and the 3:1 syngas composition both form Fe_3O_4 (solid conversion = 0.11) throughout the bed before breakthrough. The 1:1 syngas forms a small amount of FeO at the bed entrance, while the higher quality 3:1 syngas

forms slightly more FeO at the bed entrance before breakthrough. Since the material reduced to Fe₃O₄ cannot be regenerated with H₂O, the predicted H₂ output of the Fe₂O₃ at these temperatures is less than 0.1 moles of H₂ per mole of metal oxide after reduction with either syngas composition.

CoFe₂O₄ and NiFe₂O₄ are also reduced to Fe₃O₄ at 873 K; however, the Co and Ni are reduced as well, giving the material a conversion of at least 33% (representative of solid products Fe₃O₄ and Co or Ni) throughout the bed before breakthrough. As with the Fe₂O₃ material, a small amount of FeO forms during reduction with the 1:1 syngas. Reduction with the 3:1 syngas forms Fe in the first 10% of the bed, which was not seen with the Fe₂O₃. For these materials at 873 K, the H₂ production per mole of metal oxide was 1.25 after reduction with 1:1 syngas, and 1.5 after reduction with the 3:1 syngas. The R value for the Fe₂O₃ was nearly three times the value of R for the mixed metal ferrites, meaning that over three times the Fe₂O₃ would be needed in a reactor to react with the same amount of syngas as the CoFe₂O₄ and NiFe₂O₄.

At 1073 K (Figure 6.9), the 1:1 syngas reduced about one third of the Fe₂O₃ in the bed to FeO (solid conversion = 33%), a direct result of the increase in H₂O/H₂ equilibrium constant as the temperature increases, which allows formation of Fe and FeO at higher H₂O/H₂ ratios. The rest of the material is reduced to Fe₃O₄. The 3:1 syngas reduced nearly half of the Fe₂O₃ to FeO, and formed a small amount of Fe in the first 5% of the reactor. At these higher temperatures, the H₂ produced per mole of metal oxide is 0.52 after reduction with 1:1 syngas and 0.78 after reduction with 3:1 syngas.

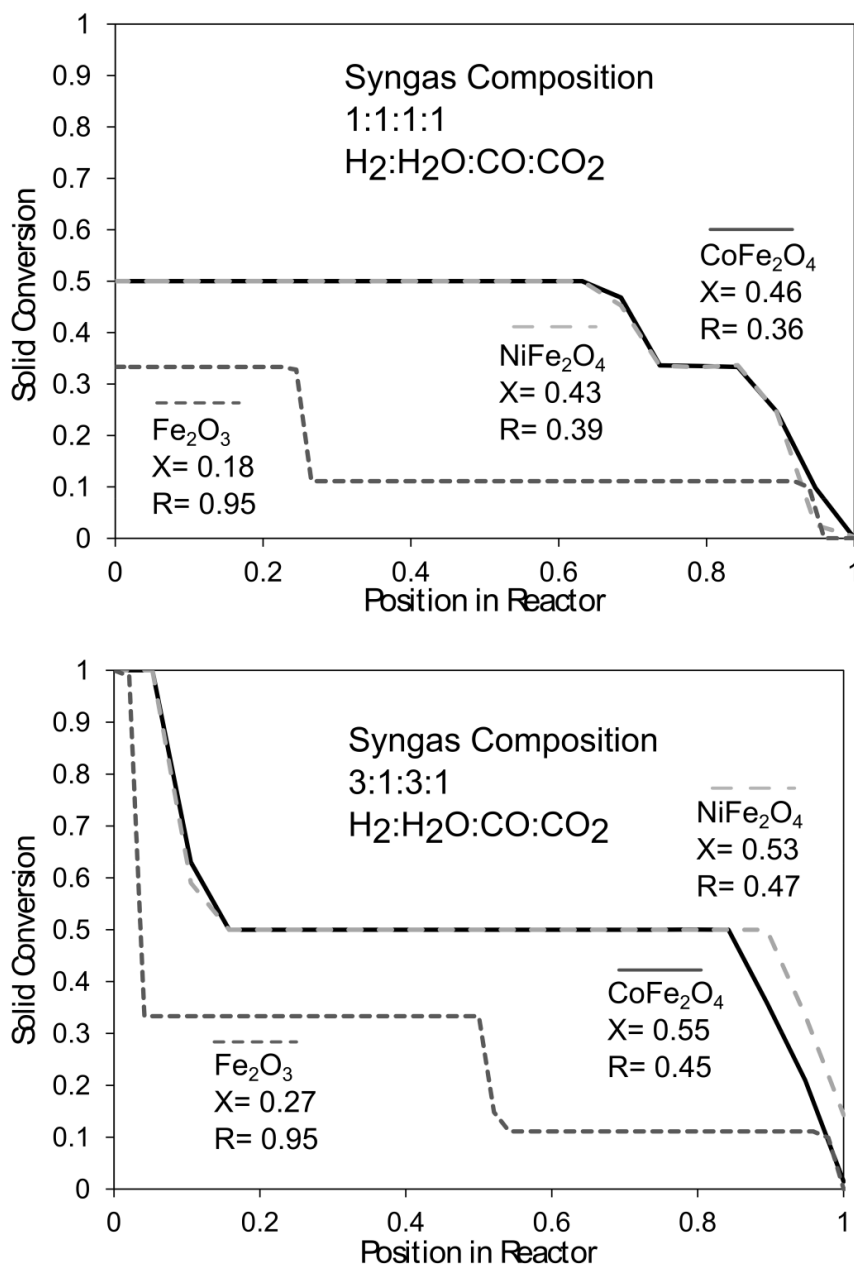


Figure 6.9: Conversion of solid materials at breakthrough for each metal oxide type at 1073 K under different syngas compositions and temperatures. X values are material conversion and R values are the ratio of moles of solid in the bed to moles of syngas through the reactor at breakthrough.

The CoFe₂O₄ and NiFe₂O₄ were also reduced to FeO and Co or FeO and Ni (solid conversion = 0.5) in the majority of the bed under both syngas compositions at 1073 K. The 3:1

syngas formed Fe in the first 10% of the reactor, and the materials had an H₂ production per mole of metal oxide of 2.1. After reduction with 1:1 syngas, the H₂ production per mole of metal oxide was 1.65. The R values for Fe₂O₃ under these conditions are nearly twice those of the mixed metal ferrites, meaning that twice as much Fe₂O₃ as CoFe₂O₄ or NiFe₂O₄ is necessary to fully react with the same amount of syngas.

For both materials, higher temperatures resulted in higher overall conversions due to the increase in the equilibrium constant, which allows access to more of the O in the solid under the same gas compositions. Although the higher temperature is attractive for the reduction step, in the oxidation step, the result is lower conversions of H₂ to H₂O during the H₂O oxidation.

6.5.2.2. Complete Steam Oxidations

Simulations for complete H₂O oxidation following syngas reduction allowed the calculation of the energy requirement for steam generation. Reduction simulations were performed with 1:1 and 3:1 syngas compositions at 873 K and 1073 K until the point of breakthrough, and then complete H₂O oxidation was simulated at the same temperature. The ratio of total H₂ generated/total H₂O fed and the HHV of produced H₂/ steam generation energy for these oxidations are shown in Table 6.2, and indicate significant energy requirements to generate enough steam for complete H₂O oxidation of mixed metal oxides. For Fe₂O₃, the ratio of H₂/H₂O ranges from 0.35 to 0.57, indicating an overall high conversion of the H₂O to H₂ as expected. For the 1:1 syngas, the H₂/H₂O ratio decreases at higher temperatures due to the decrease in the equilibrium for H₂O oxidation at higher temperatures; however, the 3:1 gas composition shows an increase in conversion. This is due to the formation of Fe metal at the higher temperature, which has a higher H₂O to H₂ conversion during oxidation.

Material	Reducing Gas	Temperature (K)	Mol H ₂ /Mol H ₂ O	HHV H ₂ /ΔH _{steam}
Fe ₂ O ₃	1:1	873	0.37	1.4
	1:1	1073	0.26	0.86
	3:1	873	0.38	1.5
	3:1	1073	0.57	0.95
CoFe ₃ O ₄	1:1	873	0.1	0.4
	1:1	1073	0.01	0.04
	3:1	873	0.1	0.3
	3:1	1073	0.01	0.05
NiFe ₂ O ₄	1:1	873	0.03	0.14
	1:1	1073	< 0.01	0.004
	3:1	873	0.02	0.1
	3:1	1073	< 0.01	0.005

Table 6.2: Moles of H₂ produced per mole of H₂O fed to the reactor and the HHV value of the H₂ produced in comparison to the energy needed to generate steam for full H₂O oxidation of materials for reduction conditions and temperatures.

For CoFe₂O₄, the amount of energy required to generate steam for complete oxidation was more than double the energy gained from the H₂ produced at 673 K, and the overall conversion of H₂O to H₂ was less than 10%. At higher temperatures these values decrease due to the decrease in the oxidation equilibrium constant. The energy necessary to produce steam for the NiFe₂O₄ oxidation was nearly ten times the energy recovered from the H₂, and overall H₂O conversion to H₂ during oxidation was less than 5% under all conditions. These results indicate that full oxidation with H₂O is not feasible for CoFe₂O₄ and NiFe₂O₄, and that an O₂ oxidation

step is necessary for efficient full regeneration in a CLH reactor. The combined H₂O/O₂ oxidation is investigated in the next section.

6.5.2.3. Hybrid steam/O₂ Oxidations

The point at which H₂O oxidation should be terminated and O₂ oxidation begun is system specific, but depends on the amount of H₂ recovered, the amount of H₂O necessary to produce the H₂, and the heats of reaction for both the reduction and oxidation reactions. Two parameters were calculated in this analysis to compare the benefit of the H₂ recovery to the energy cost of the additional steam generation. The first was called the CLH efficiency, and was defined as

$$\eta_{CLH} = \frac{\Delta H_r[-] + \Delta H_{C,H_2}[-] + \Delta H_{steam}[+]}{\Delta H_{C,syngas}[-]} \quad \text{Eq. 6.23}$$

where $\Delta H_{C,H_2}$ is the heat of combustion of the generated H₂, $\Delta H_{C,syngas}$ is the heat of combustion of the syngas used in the reduction, and ΔH_r is the sum of all heats of reaction in the system:

$$\Delta H_r = \Delta H_{reduction} + \Delta H_{H_2O\ oxidation} + \Delta H_{O_2\ oxidation} \quad \text{Eq. 6.24}$$

This parameter penalized the process for the energy required to generate steam, ΔH_{steam} . The bracketed signs indicate the sign expected for each ΔH value. The total ΔH_r should always be negative, as should the $\Delta H_{C,H_2}$ and the $\Delta H_{C,syngas}$. The ΔH_{steam} will always be positive; therefore, when the energy required to generate steam for the oxidation is more than can be recovered from the H₂ combustion, and the reduction and oxidation reactions combined, the η_{CLH} becomes negative. A value of 1 represents the combustion of the syngas and is the CLC limit. The second parameter was the syngas conversion efficiency, as defined in Chapter 3:

$$\eta_{\text{syngas conversion}} = \frac{\text{Moles } H_2 \text{ generated}}{\text{Moles } H_2/CO \text{ consumed in reduction}} \quad \text{Eq. 6.25}$$

and was a measure of the H_2 recovered from the process.

Two syngas compositions were tested for each material at temperatures 873 K and 1073 K, and the CLH efficiency and conversion efficiency were calculated for each. Reduction until breakthrough was modeled for each condition, and different ratios of H_2O oxidation followed by O_2 oxidation were modeled for each reduction condition at the same temperature. Results are plotted in Figure 6.10.

At 873 K, the CLH conversion value was greater than 80% under all conditions for Fe_2O_3 ; however, the syngas conversion was limited to under 25% due to the inability to oxidize Fe_3O_4 to Fe_2O_3 . This was especially evident with the 1:1 syngas, as less than 10% of the H_2 was recovered from the process. For the 1:1 syngas reduction at 873 K, the performance of the mixed metal ferrites was superior to that of the Fe_2O_3 material due to this low conversion.

For the 3:1 syngas reductions at 873 K, the $CoFe_2O_3$ and $NiFe_2O_4$ CLH conversion values follow those of the Fe_2O_3 up until syngas conversion is nearly 30%. Then, the slope of the CLH conversion curves for $NiFe_2O_4$ and $CoFe_2O_4$ change to follow the slope of the 1:1 syngas reduction values. These trends make clear the dependence of the oxidation properties on the reduction state of the materials in the bed prior to oxidation. As shown in Figure 6.9, mixed metal ferrites reduced with 3:1 syngas form FeO and Fe near the entrance of the reactor. The oxidation thermodynamics of Fe and FeO in the mixed metal ferrites bed follow those of the Fe -only material during the initial oxidation of the Fe to Fe_3O_4 , as shown in Figure 6.10. Then, they follow a characteristic curve for the formation of the mixed metal spinel from Fe_3O_4 and Co or Fe_3O_4 and Ni . The response is non-linear due to the non-linear relationship between H_2O

generated and H_2 produced as the reaction proceeds. The H_2 recovered along this curve does add significantly to the total H_2 recovered from the process; however, it does so at the expense of the CLH efficiency value.

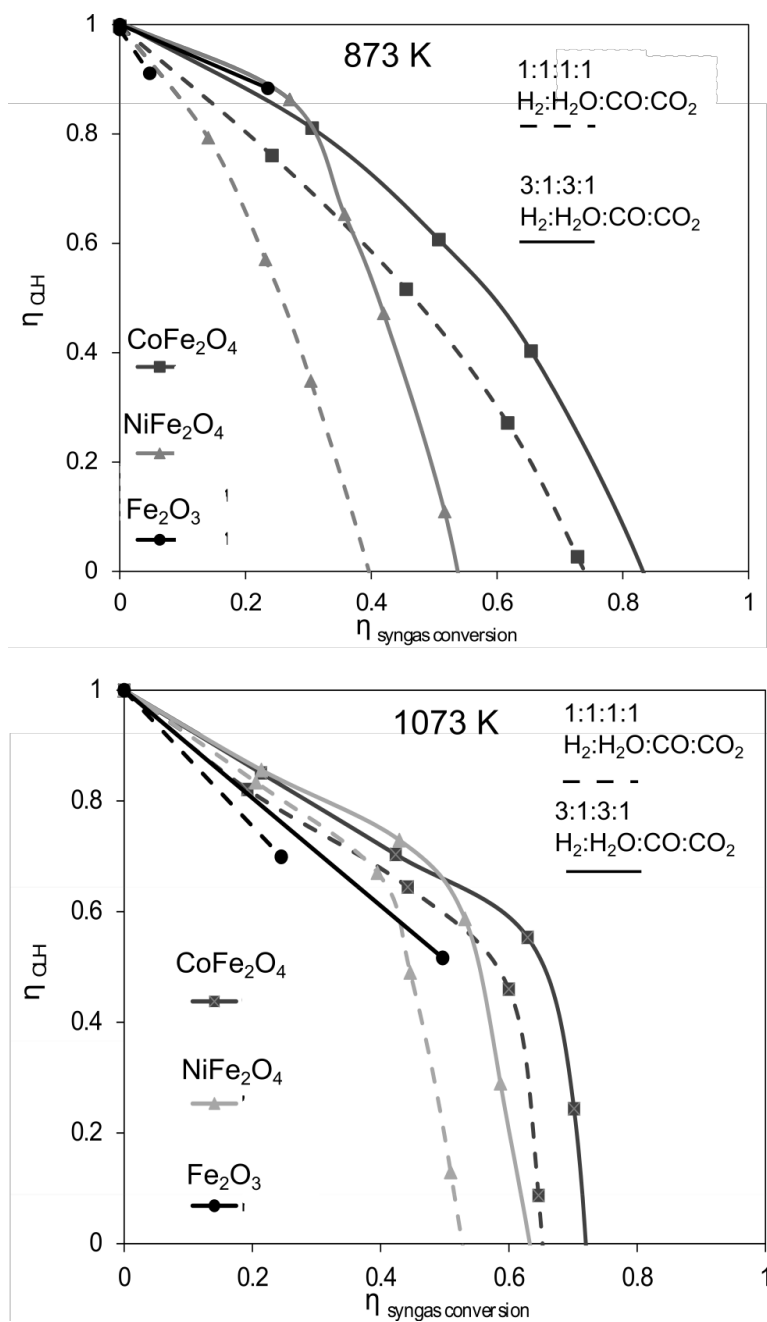


Figure 6.10: CLH efficiency vs. the conversion efficiency of the materials at 873 K and 1073 K after reduction with two different syngas compositions

At 1073 K, the syngas conversions for the Fe_2O_3 material double from their values at 873 K. This H_2 recovery is due to the Fe and FeO formed in the reactor during reduction, which allow significantly more H_2 recovery than the Fe_3O_4 and FeO formed at 873 K do. The mixed metal ferrites show higher syngas conversions than Fe_2O_3 up to about 60%, at which point the CLH efficiency drops to zero with a 5-10% increase in syngas conversion. This sharp decrease in CLH efficiency is due to the decrease in oxidation equilibrium constant at the higher temperatures for the regeneration of the mixed metal ferrite.

Results show that these materials can operate as efficiently as Fe_2O_3 in the lower syngas conversion region of the plot at both temperatures under each reduction condition. At 873 K, the mixed metal ferrites, especially CoFe_2O_4 , can have a significantly higher syngas conversion at lower CLH efficiency values. The NiFe_2O_4 can only offer modest H_2 recovery gains at lower CLH efficiency values. At 1073 K, both mixed metal ferrites offer significant H_2 recovery compared to Fe_2O_3 after reduction with the 1:1 syngas; however, the H_2 recovery gain is modest after the 3:1 syngas reduction. Under all conditions, use of the mixed metal ferrites would require less material in the bed for the same syngas throughput, thereby decreasing the size of reactor for the CLH process.

Mixed metal ferrites would offer significant advantage over conventional Fe_2O_3 materials for systems with lower quality syngas and/or lower operating temperatures. For example, much of the syngas produced from gasification of biomass, such as wood products, has reducing gas to oxidizing gas ratios between 1:1 and 2:1, which are lower ratios than much of the syngas produced from coal gasification. [21] In this composition range, the mixed metal ferrites would allow higher metal oxide conversions than Fe_2O_3 , and would give the CLH process more flexibility with the amounts of H_2 produced without sacrificing the ability to efficiently generate

electricity with integrated CO₂ capture. Depending on efficiency requirements of the system, up to 80% of the H₂ could be recovered from the process.

6.6 Conclusions

First, this study showed that the reduction step for the CLH process with Fe₂O₃, CoFe₂O₄, and NiFe₂O₄ in a packed bed reactor can be reasonably approximated in a model as reaching thermodynamic equilibrium at low to moderate solid conversions. The developed model was used to investigate the conversion of Fe₂O₃, CoFe₂O₄, and NiFe₂O₄ during syngas reduction in a packed bed reactor prior to H₂ and CO breakthrough. The conversion in the bed was shown to be significantly higher for mixed metal ferrites before breakthrough than for Fe₂O₃, offering the advantage of a smaller reactor for the same syngas throughput and conversion with these mixed metal materials. Higher solid conversion, combined with the ability of CoFe₂O₄ and NiFe₂O₄ to fully re-oxidize with H₂O, lead to more than three times greater H₂ production from the mixed metal ferrites than from Fe₂O₃. When the reaction energetics are considered, full recovery of H₂ from mixed metal ferrites is not favorable; however, the materials offer increased flexibility over the Fe₂O₃ materials in the ratio of H₂/electricity generation possible due to the low recovery of H₂ using Fe₂O₃. Thus, the greatest advantage in using the mixed metal ferrites is observed at the lower conversions obtained at lower reduction temperatures and from reduction with weaker syngas, making them an ideal material choice for syngas from various biomass materials like wood products. At higher temperatures, the CoFe₂O₄ still offers slightly greater H₂ recovery than Fe₂O₃, but the advantage is less due to higher H₂ recovery from the Fe-based materials at these temperatures. Under all conditions, the mixed metal ferrites still consume significantly more syngas per cycle than Fe₂O₃.

6.7 References

- [1] Bohn CD, Muller CR, Cleeton JP, Hayhurst AN, Davidson JF, Scott SA, et al. Production of Very Pure Hydrogen with Simultaneous Capture of Carbon Dioxide using the Redox Reactions of Iron Oxides in Packed Beds. *Ind Eng Chem Res* 2008;47:7623-30.
- [2] Gupta P, Velazquez-Vargas L, Fan L. Syngas Redox (SGR) Process to Produce Hydrogen from Coal Derived Syngas. *Energy Fuels*. 2007;21:2900-8.
- [3] Fan L. *Chemical Looping Systems for Fossil Energy Conversion*. Hoboken, NJ: John Wiley & Sons, Inc.; 2010.
- [4] Jerndal E, Mattisson T, Lyngfelt A. Thermal Analysis of Chemical-Looping Combustion. *Chemical Engineering Research and Design*. 2006;84:795-806.
- [5] Mattisson T, García-Labiano F, Kronberger B, Lyngfelt A, Adánez J, Hofbauer H. Chemical-looping combustion using syngas as fuel. *International Journal of Greenhouse Gas Control*. 2007;1:158-69.
- [6] Fan L, Li F, Ramkumar S. Utilization of chemical looping strategy in coal gasification processes. *Particuology*. 2008;6:131-42.
- [7] Solunke R, Vesper G. Hydrogen Production via Chemical Looping Steam Reforming in a Periodically Operated Fixed-Bed Reactor. *Ind Eng Chem Res*. 2010;49:11037-44.
- [8] Li F, Zeng L, Velazquez-Vargas L, Yoscovitis Z, Fan L. Syngas Chemical Looping Gasification Process: Bench-scale Studies and Reactor Simulations. *AIChE J*. 2010;56:2186-99.
- [9] Fraser SD, Monsberger M, Hacker V. A thermodynamic analysis of the reformer sponge iron cycle. *Journal of Power Sources*. 2006;161:420-31.
- [10] Allendorf M, Diver R, Siegel N, Miller J. Two-Step Water Splitting Using Mixed-Metal Ferrites: Thermodynamic Analysis and Characterization of Synthesized Materials. *Energy Fuels*. 2008;4115-24.
- [11] Scheffe J, Li J, Weimer A. A spinel/hercynite water-splitting redox cycle. *Int J Hydrogen Energy*. 2010:3333-40.

[12] DECTEROV SA, JUNG I-H, JAK E, KANG Y-B, HAYES P, PELTON AD. Thermodynamic modelling of the $\text{Al}_2\text{O}_3\text{-CaO-CoO-CrO-Cr}_2\text{O}_3\text{-FeO-Fe}_2\text{O}_3\text{-MgO-MnO-NiO-SiO}_2\text{-S}$ system and applications in ferrous process metallurgy. VII International Conference on Molten Slags Fluxes and Salts 2004.

[13] Frisk K, Selleby M. The compound energy formalism: applications. *Journal of Alloys and Compounds*. 2001;320:177-88.

[14] Jung IH, Decterov SA, Pelton AD, Kim H, Kang Y. Thermodynamic evaluation and modeling of the Fe–Co–O system. *Acta Materialia*. 2004;52:507-19.

[15] Bale CW, Chartrand P, Decterov SA, Eriksson G, Hack K, R. Ben Mahfoud R, et al. FactSage Thermochemical Software and Databases. *Calphad*. 2002;26:189–228.

[16] Young D. *High Temperature Oxidation and Corrosion of Metals*. Amsterdam, The Netherlands: Elsevier; 2008.

[17] Muller C, Bohn C, Song Q, Scott S, Dennis J. The production of separate streams of pure hydrogen and carbon dioxide from coal via an iron-oxide redox cycle. *Chem Eng J* 2011;166:1052-60.

[18] Smith B, Loganathan M, Shantha M. A Review of the Water Gas Shift Reaction Kinetics. *Int J Chem React Eng*. 2010;8.

[19] Mattison T, Jardnas A, Lyngfelt A. Reactivity of Some Metal Oxides Supported on Alumina with Alternating Methane and Oxygens: Application for Chemical-Looping Combustion. *Energy Fuels*. 2003;17:643-51.

[20] Hossain MM, Sedor KE, de Lasa HI. Co-Ni/ Al_2O_3 oxygen carrier for fluidized bed chemical-looping combustion: Desorption kinetics and metal-support interactions. *Chem Eng Sci*. 2007;62:5464-72.

[21] Ciferno JP, Marano JJ. *Benchmarking Biomass Gasification Technologies for Fuels, Chemicals and Hydrogen Production*. U.S. Department of Energy National Energy Technology Laboratory; 2002.

Chapter 7: Conclusions and Future Work

7.1 Conclusions

The purpose of this thesis was to investigate the materials CoFe_2O_4 and NiFe_2O_4 for use in the CLH system. These materials have been proposed as alternatives to Fe_2O_3 as metal oxides for the CLH process and the limited experimental data in literature regarding their use looks promising; however, no comprehensive investigation involving cyclability with phase analysis or their performance meeting the criteria for CLH materials in a packed bed reactor has been published.

Both CoFe_2O_4 and NiFe_2O_4 cycled under CLH conditions, and both reduced materials were highly reactive with steam in the CLH temperature range. Raman spectroscopy showed the mixed metal spinel phase was regenerated during H_2O oxidation, an important finding due to the concerns of metal segregation during H_2O oxidation. The use of a high surface area inert m-ZrO_2 support substrate resulted in materials that were stable in chemical redox at temperature below 873 K. Interactions between the metal oxide and support were not detected with Raman spectroscopy or XRD analysis. The oxidation rates of CoFe_2O_4 and NiFe_2O_4 were shown to be sensitive to both temperature and H_2O concentration.

To justify the use of NiFe_2O_4 and CoFe_2O_4 in a CLH system, the conversion of H_2 to H_2O and CO to CO_2 during the CLH reduction step must be high to both limit the amount of chemical energy lost, and limit the amount of impurities in the CO_2 for sequestration. The FactSageTM thermodynamic software and associated databases were used to investigate the predicted equilibrium conditions between the metal oxides and the $\text{H}_2/\text{H}_2\text{O}$ and CO/CO_2 systems. Calculations predicted high conversions during the reduction step for each material, and showed

the formation of a Fe-rich spinel and metallic Co or Ni phase during the initial stage of spinel reduction. Experiments with NiFe_2O_4 and CoFe_2O_4 confirmed the high conversion of CO and H_2 during the reduction step, and XRD and Raman analysis of the material showed formation of a Fe-rich spinel and a metallic phase during reduction. Additionally, the H_2 produced during full H_2O oxidation was over 90% of the quantity of H_2/CO used to reduce the material when the reduction step was stopped at breakthrough. In contrast, the H_2 produced from the Fe_2O_3 material was only 20% of the H_2/CO used in the reduction step, a consequence of the inability of Fe_2O_3 to be regenerated with just H_2O oxidation. The H_2O oxidation was observed to be slower for the mixed metal ferrites than for the Fe-only material, prompting a kinetic investigation into the oxidation mechanism for the mixed metal spinels.

A kinetic investigation of the H_2O oxidation of Fe-only materials and mixed metal spinels, conducted in a stagnation flow reactor, showed the oxidation of reduced Fe_3O_4 to be limited by an order of reaction model that is believed to represent a surface reaction limitation. The mixed metal materials also showed order of reaction behavior during the first 100-200 seconds of reaction, followed by a slower H_2 production tail modeled as a diffusion limitation. This limitation was hypothesized to be in the spinel phase, since cation migration in Fe_3O_4 has been shown to slow as a secondary cation is incorporated into the lattice. Reaction models were fit with an error minimization technique that took into account all data points from all temperatures and H_2O concentrations for each material, resulting in a globally optimized fit over all the data.

The full H_2O re-oxidation of the mixed metal ferrites in a packed bed reactor required excess steam generation for hours, requiring significant energy for steam production while generating small amounts of H_2 . Since the CoFe_2O_4 and NiFe_2O_4 must be fully regenerated for

the subsequent reduction cycle, a secondary O_2 oxidation is proposed to fully oxidize the metal oxide and generate heat. The reduction reaction in a packed bed was shown to have rapid enough kinetics to be approximated with an equilibrium model, which predicted the conversion of solid material in the bed prior to H_2O oxidation. The mixed metal ferrites have higher material conversions than Fe_2O_3 under all reduction conditions due to the reduction of the Co^{2+} and Ni^{2+} to their metallic states. When the H_2O oxidation is also approximated as an equilibrium-limited reaction, as a “best-case” scenario, complete steam oxidation of $CoFe_2O_4$ and $NiFe_2O_4$ is not a feasible option. However, when H_2O oxidation is followed by O_2 oxidation, the mixed metal ferrites are equally as efficient as Fe_2O_3 materials, and offer superior and efficient H_2 production after lower temperature reductions and when reduced with lower quality syngas.

7.2 Future Work

Ultimately, these metal oxides are for use in large, industrial scale CLH reactors. Since these mixed metal ferrites have proven successful in a laboratory scale reactor, the next step is to test them in a larger system with more realistic operating conditions. New synthesis techniques would need to be investigated and tested for $CoFe_2O_4$ and $NiFe_2O_4$, as typical metal oxide mass loadings for industrial scale CLH reactors are in excess of 60%. [1] Since most large-scale CLH reactors include physical movement of particles from one reactor to the next, particle attrition would also need to be studied.

The initial stage of H_2O oxidation of reduced $CoFe_2O_4$ and $NiFe_2O_4$ appears to be limited by a surface reaction, modeled in this study by an order of reaction model. If a surface reaction is indeed limiting, then the rates of oxidation may be improved by the incorporation of a catalyst that is active for the rate-limiting step. Samples prepared using ALD are ideal for this test, as a

catalyst deposited over the total area of the film could provide superior metal oxide –catalyst contact. Additionally, use of DFT to examine the H₂O surface reaction could help to identify the exact mechanism of limitation.

This study focused on CoFe₂O₄ and NiFe₂O₄, but preliminary studies show Cu/Fe, Zn/Fe, and Mn/Fe materials to be capable of redox cycling with syngas.[2, 3] A more comprehensive study of these ferrite materials may identify them as potential CLH materials as well.

Investigations would need to include packed bed reactor studies to determine the H₂ and CO conversion during syngas reduction and the H₂ production capacity of the material in comparison to other CLH materials.

The chemical looping process with the highest projected H₂ production efficiency is the Coal-Direct Chemical Looping (CDCL) scheme. [1] This process directly contacts coal or biomass with metal oxides at high temperatures, significantly decreasing the complexity of the overall system. The oxygen from the metal oxide that is used to produce CO₂ and H₂O from the solid material decreases the O₂ necessary from an air separation unit during gasification, thereby decreasing the expense of the gasification process. The CDCL process is receiving an increased level of interest from researchers worldwide, and an investigation of CoFe₂O₄ or NiFe₂O₄ for use in this system would directly contribute to this growing field.

7.3 References

[1] Fan L. Chemical Looping Systems for Fossil Energy Conversion. Hoboken, NJ: John Wiley & Sons, Inc.; 2010.

[2] Go KS, Son SR, Kim SD. Reaction kinetics of reduction and oxidation of metal oxides for hydrogen production. Int J Hydrogen Energy. 2008;33:5986-95.

[3] Chiron F-X, Patience GS. Kinetics of mixed copper–iron based oxygen carriers for hydrogen production by chemical looping water splitting. *International Journal of Hydrogen Energy*. 2012;37:10526-38.

Bibliography

- [1] (EIA) EIA. Annual Energy Outlook 2007. Washington, D.C.: U.S. Department of Energy; 2007.
- [2] Abad A, Garcia-Labiano F, Diego LFd, Gayan P, Adanez J. Reduction Kinetics of Cu-, Ni-, and Fe-Based Oxygen Carriers Using Syngas (CO + H₂) for Chemical-Looping Combustion. *Energy & Fuels*. 2007;21:1843-53.
- [3] Abad A, Mattisson T, Lyngfelt A, Johansson M. The use of iron oxide as oxygen carrier in a chemical-looping reactor. *Fuel*. 2007;86:1021-35.
- [4] Aggarwal S, Topfer J, Tsai T, Dieckmann R. Point Defects and transport in binary and ternary, non-stoichiometric oxides. *Solid State Ionics*. 1997:321-31.
- [5] Allendorf M, Diver R, Siegel N, Miller J. Two-Step Water Splitting Using Mixed-Metal Ferrites: Thermodynamic Analysis and Characterization of Synthesized Materials. *Energy Fuels*. 2008:4115-24.
- [6] Anjum S, Jaffari GH, Rumaiz AK, Rafique MS, Shah SI. Role of vacancies in transport and magnetic properties of nickel ferrite thin films. *Journal of Physics D: Applied Physics*. 2010;43.
- [7] Asato M, Hoshino T, Asada T, Zeller R, Dederichs PH. Vacancy formation energies in FCC metals: non-local effect beyond the LSDA. *Journal of Magnetism and Magnetic Materials*. 1998;177–181, Part 2:1403-4.
- [8] Atkinson A. Transport processes during the growth of oxide films at elevated temperature. *Reviews of Modern Physics*. 1985;57:437-70.
- [9] Atkinson A, O'Dwyer ML, Taylor RI. 55Fe diffusion in magnetite crystals at 500C and its relevance to oxidation of iron. *Journal of Materials Science*. 1983;18:2371-9.
- [10] Ayyappan S, Mahadevan S, Chandramohan P, Srinivasan MP, Philip J, Raj B. Influence of Co²⁺ Ion Concentration on the Size, Magnetic Properties, and Purity of CoFe₂O₄ Spinel Ferrite Nanoparticles. *The Journal of Physical Chemistry C*. 2010;114:6334-41.
- [11] Bahlawane N, Ngamou PHT, Vannier V, Kottke T, Heberle J, Kohse-Hoinghaus K. Tailoring the properties and the reactivity of the spinel cobalt oxide. *Physical Chemistry Chemical Physics*. 2009;11:9224-32.
- [12] Bajorek C, Nicolet, M., Wilts, C. Preferential Oxidation of Fe in Permalloy Films. *Applied Physics Letters*. 1971;82:82-4.
- [13] Bajorek C, Nicolet M, Wilts C. Preferential Oxidation of Fe in Permalloy Films. *Appl Phys Lett*. 1971;82:82-4.

- [14] Bale CW, Chartrand P, Degterov SA, Eriksson G, Hack K, R. Ben Mahfoud R, et al. FactSage Thermochemical Software and Databases. *Calphad*. 2002;26:189–228.
- [15] Bamford CH, Tipper, C.F.H. *Comprehensive Chemical Kinetics: Volume 22 Reactions in the Solid State* Elsevier Scientific Publishing Company; 1980.
- [16] Beck HP, Kaliba C. On the solubility of Fe, Cr and Nb in ZrO₂ and its effect on thermal dilatation and polymorphic transition. *Materials Research Bulletin*. 1990;25:1161-8.
- [17] Birks N, Meier, G., Pettit, F. *Introduction to the High-Temperature Oxidation of Metals*. Cambridge, UK: Cambridge University Press; 2006.
- [18] Bleeker MF, Veringa HJ, Kersten SRA. Deactivation of iron oxide used in the steam-iron process to produce hydrogen. *Appl Catal, A*. 2009;357:5-17.
- [19] Bleeker MF, Veringa HJ, Kersten SRA. Pure Hydrogen Production from Pyrolysis Oil Using the Steam-Iron Process: Effects of Temperature and Iron Oxide Conversion in the Reduction. *Ind Eng Chem Res*. 2010;49:53-64.
- [20] Bockris JOM. The origin of ideas on a hydrogen economy and its solution to the decay of the environment. *International Journal of Hydrogen Energy*. 2002;27:731-40.
- [21] Bogdanov SS, Aleksic, B.D. Comparative study of the reduction kinetics of magnetites and derived ammonia synthesis catalysts. *Thermochimica Acta*. 1990;173:71-9.
- [22] Bohn CD, Muller CR, Cleeton JP, Hayhurst AN, Davidson JF, Scott SA, et al. Production of Very Pure Hydrogen with Simultaneous Capture of Carbon Dioxide using the Redox Reactions of Iron Oxides in Packed Beds. *Ind Eng Chem Res* 2008;47:7623-30.
- [23] Bruckner W, Baunack, S., Hecker, M. et al. Oxidation of NiFe(20 wt.%) thin films. *Materials Science and Engineering B*. 2001;B86:272-5.
- [24] Bruckner W, Baunack S, Hecker M, Thomas J, Groudeva-Zotova S, Schneider CM. Oxidation of NiFe(20 wt.%) thin films. *Mater Sci Eng B*. 2001;B86:272-5.
- [25] Campo Ld, Perez-Saez RB, Tello MJ. Iron oxidation kinetics study by using infrared spectral emissivity measurements below 570 C. *Corrosion Science*. 2008;50:194 -9.
- [26] Castleton CWM, Höglund A, Mirbt S. Density functional theory calculations of defect energies using supercells. *Modelling and Simulation in Materials Science and Engineering*. 2009;17.
- [27] Chamritski I, Burns G. Infrared- and Raman-Active Phonons of Magnetite, Maghemite, and Hematite: A Computer Simulation and Spectroscopic Study. *The Journal of Physical Chemistry B*. 2005;109:4965-8.

- [28] Chandramohan P, Srinivasan MP, Velmurugan S, Narasimhan SV. Cation distribution and particle size effect on Raman spectrum of CoFe_2O_4 . *Journal of Solid State Chemistry*. 2011;184:89-96.
- [29] Chen S, Shi Q, Xue Z, Sun X, Xiang W. Experimental investigation of chemical-looping hydrogen generation using Al_2O_3 or TiO_2 -supported iron oxides in a batch fluidized bed. *International Journal of Hydrogen Energy*. 2011;36:8915-26.
- [30] Chen W, Downing, H. Cation Self-Diffusion in CoFe_2O_4 . *Phys Stat Sol*. 1976;37:515-20.
- [31] Chiron F-X, Patience GS. Kinetics of mixed copper-iron based oxygen carriers for hydrogen production by chemical looping water splitting. *International Journal of Hydrogen Energy*. 2012;37:10526-38.
- [32] Chiron F-X, Patience GS, Riffart S. Hydrogen production through chemical looping using $\text{NiO/NiAl}_2\text{O}_4$ as oxygen carrier. *Chemical Engineering Science*. 2011;66:6324-30.
- [33] Cho P, Mattisson T, Lyngfelt A. Comparison of iron-, nickel-, copper- and manganese-based oxygen carriers for chemical-looping combustion. *Fuel*. 2004;83:1215.
- [34] Ciferno JP, Marano JJ. Benchmarking Biomass Gasification Technologies for Fuels, Chemicals and Hydrogen Production. U.S. Department of Energy National Energy Technology Laboratory; 2002.
- [35] Cramer CJ, Truhlar, Donald G. . Density functional theory for transition metals and transition metal chemistry. *Phys Chem Chem Phys*. 2009;11:10757-816.
- [36] da Cunha Belo M, Walls M, Hakiki NE, Corset J, Picquenard E, Sagon G, et al. Composition, structure and properties of the oxide films formed on the stainless steel 316L in a primary type PWR environment. *Corrosion Science*. 1998;40:447-63.
- [37] Damen K, Troost Mv, Faaij A, Turkenburg W. A comparison of electricity and hydrogen production systems with CO_2 capture and storage. Part A: Review and selection of promising conversion and capture technologies. *Progress in Energy and Combustion Science*. 2006;32:215-45.
- [38] Davison S, Kershaw R, Dwight K, Wold A. Preparation and characterization of cubic ZrO_2 stabilized by Fe(III) and Fe(II). *Journal of Solid State Chemistry*. 1988;73:47-51.
- [39] DECTEROV SA, JUNG I-H, JAK E, KANG Y-B, HAYES P, PELTON AD. Thermodynamic modelling of the $\text{Al}_2\text{O}_3\text{-CaO-CoO-CrO-Cr}_2\text{O}_3\text{-FeO-Fe}_2\text{O}_3\text{-MgO-MnO-NiO-SiO}_2\text{-S}$ system and applications in ferrous process metallurgy. VII International Conference on Molten Slags Fluxes and Salts 2004.

- [40] Dieckmann R. Point Defects and Transport Properties of Binary and Ternary Oxides. *Solid State Ionics*. 1984;12:1-22.
- [41] Dieckmann R, Mason T, Hodge J, Schmalzried H. Defects and Cation Diffusion in Magnetite (III). Tracer diffusion of Foreign Cations as a Function of Temperature and Oxygen Potential *Ber Bunsenges Phys Chem*. 1978;82.
- [42] Division UNDoEaSAP. World Population to 2300. New York United Nations; 2004.
- [43] Drittler B, Weinert M, Zeller R, Dederichs PH. Vacancy formation energies of fcc transition metals calculated by a full potential green's function method. *Solid State Communications*. 1991;79:31-5.
- [44] EIA. Annual Energy Review 2008. United States Department of Energy; 2008.
- [45] Elkins P, Hughes N. The prospects for a hydrogen economy (1): hydrogen futures. *Technology Analysis & Strategic Management*. 2009;21:781.
- [46] Fan L. *Chemical Looping Systems for Fossil Energy Conversion*. Hoboken, NJ: John Wiley & Sons, Inc.; 2010.
- [47] Fan L, Li F, Ramkumar S. Utilization of a chemical looping strategy in coal gasification processes. *Particuology*. 2008;6:131-42.
- [48] Fan L, Li F, Ramkumar S. Utilization of chemical looping strategy in coal gasification processes. *Particuology*. 2008;6:131-42.
- [49] Fang H, Halbin L, Zengli Z. Advancements in Development of Chemical-Looping COmbustion: A Review. *International Journal of Chemical Engineering*. 2009:710515.
- [50] Faria DLAd, Silva SV, Oliveira MTd. Raman Microspectroscopy of Some Iron Oxides and Oxyhydroxides. *Journal of Raman Spectroscopy*. 1997;28:873-8.
- [51] Farmer R. 2009 DOE Hydrogen Program & Vehicle Technologies Program. 2009. p. http://www.hydrogen.energy.gov/pdfs/review09/pd_0_farmer.pdf.
- [52] Fraser SD, Monsberger M, Hacker V. A thermodynamic analysis of the reformer sponge iron cycle. *Journal of Power Sources*. 2006;161:420-31.
- [53] Frisk K, Selleby M. The compound energy formalism: applications. *Journal of Alloys and Compounds*. 2001;320:177-88.
- [54] Frohlich G, Sachtler, M.H. Reduction enhancement of Fe₂O₃ in physical mixtures with Pt/mordenite via Pt migration or 'hydrogen spillover'. *Journal of the Chemical Society, Faraday Transactions*. 1998;94:1339-46.

- [55] G.V.Lewis, Catlow CRA, Corma AN. Defect Structure and Migration in Fe₃O₄. *J PhysChem Solids* 1985;46:1227-33.
- [56] Galwey AK. Is the science of thermal analysis kinetics based on solid foundations?: A literature appraisal. *Thermochimica Acta*. 2004;413:139-83.
- [57] Gasparov LV, Tanner DB, Romero DB, Berger H, Margaritondo G, Forró L. Infrared and Raman studies of the Verwey transition in magnetite. *Physical Review B*.62: 7939-44.
- [58] Geva S, Farren M, John DHS, Hayes PC. The effects of impurity elements on the reduction of wustite and magnetite to iron in CO/CO₂ and H₂/H₂O gas mixtures. *Metallurgical Transactions B*. 1990;21B:743-51.
- [59] Go K, Son, S., Kim, S. Reaction kinetics of reduction and oxidation of metal oxides for hydrogen production. *International Journal of Hydrogen Energy*. 2008;33:5986-95.
- [60] Go KS, Son SR, Kim SD. Reaction kinetics of reduction and oxidation of metal oxides for hydrogen production. *Int J Hydrogen Energy*. 2008;33:5986-95.
- [61] Graves P, Johnston C, Campaniello J. Raman Scattering in Spinel Structure Ferrites. *Mater Res Bull*. 1988;23.
- [62] Graves PR, Johnston C, Campaniello JJ. Raman scattering in spinel structure ferrites. *Materials Research Bulletin*. 1988;23:1651-60.
- [63] Grol E. Integration of H₂ Separation Membranes with CO₂ Capture and Compression. Department of Energy, National Energy Technology Laboratory; 2009.
- [64] Gupta P, Velazquez-Vargas L, Fan L. Syngas Redox (SGR) Process to Produce Hydrogen from Coal Derived Syngas. *Energy Fuels*. 2007;21:2900-8.
- [65] Hafner J. Ab-Initio Simulations of Materials Using VASP: Density-Functional Theory and Beyond. *J Comput Chem*. 2008;29:2044-78.
- [66] Hendy S, Walker, B., Laycock, N., Ryan, M. Ab initio studies of the passive film formed on iron. *Physical Review B*.67:085407.
- [67] Hendy S, Walker B, Laycock N, Ryan M. Ab initio studies of the passive film formed on iron. *Physical Review B*. 2003;67:085407.
- [68] Herzog H. An introduction to CO₂ separation and capture technologies. Cambridge: Massachusetts Institute of Technology Energy Laboratory; 1999.
- [69] Hossain M, Sedor K, de Lasa H. Co-Ni/Al₂O₃ oxygen carrier for fluidized bed chemical-looping combustion: Desorption kinetics and metal-support interactions. *Chem Eng Sci*. 2007;62:5464-72.

- [70] Hosterman BD. Raman Spectroscopic Study of Solid Solution Spinel Oxides. Las Vegas: University of Nevada; 2011.
- [71] Inc. JEC. Integration of H₂ Separation Membranes with CO₂ Capture and Compression. National Energy Technology Laboratory; 2009.
- [72] Ishida M, Jin H, Okamoto T. Kintic Behavior of Solid Particle in Chemical-Looping COmbustion: Suppressing Carbon Deposition in Reduction. *Energy & Fuels*. 1998;12:223-9.
- [73] Ishida M, Takeshita K, Suzuki K, Ohba T. Application of Fe₂O₃-Al₂O₃ Composite Particles as Solid Looping Material of the Chemical-Loop Combustor. *Energy & Fuels*. 2005;19:2514-8.
- [74] Ivanov VG, Abrashev MV, Iliev MN, Gospodinov MM, Meen J, Aroyo MI. Short-range B-site ordering in the inverse spinel ferrite NiFe₂O₄. *Physical Review B*. 2010;82:024104.
- [75] Janak JF. Itinerant ferromagnetism in fcc cobalt. *Solid State Communications*. 1978;25:53-5.
- [76] Jarlborg T, Freeman AJ. Self-consistent semi-relativistic energy band structure of fcc and tetragonal Ni metal. *Journal of Magnetism and Magnetic Materials*. 1980;22:6-14.
- [77] Jerndal E, Mattisson T, Lyngfelt A. Thermal Analysis of Chemical-Looping Combustion. *Chemical Engineering Research and Design*. 2006;84:795-806.
- [78] Jung IH, Deckerov SA, Pelton AD, Kim H, Kang Y. Thermodynamic evaluation and modeling of the Fe-Co-O system. *Acta Materialia*. 2004;52:507-19.
- [79] Khawam A, Flanagan, D. Solid State Kinetic Models: Basics and Mathematical Fundamentals. *Journal of Physical Chemistry B*. 2006;110:17315-28.
- [80] Kim JH, Hwang IS. Development of an in situ Raman spectroscopic system for surface oxide films on metals and alloys in high temperature water. *Nuclear Engineering and Design*. 2005;235:1029-40.
- [81] King DM, Spencer II JA, Liang X, Hakim LF, Weimer AW. Atomic layer deposition on particles using a fluidized bed reactor with in situ mass spectrometry. *Surface and Coatings Technology*. 2007;201:9163-71.
- [82] Kodama T, Gokon N, Yamanmoto R. Thermochemical two-step water splitting by ZrO₂-supported Ni_xFe_{3-x}O₄ for solar hydrogen production. *Solar Energy*. 2008;82:73.
- [83] Kodama T, Kondoh Y, Yamamoto R, Andou H, Satou N. Thermochemical hydrogen production by a redox system of ZrO₂-supported Co(II)-ferrite. *Solar Energy*. 2005;78:623.

- [84] Kodama T, Nakamuro Y, Mizuno T. A two-step thermochemical water splitting by iron-oxide on stabilized zirconia. *Journal of Solar Energy Engineering-Transactions of the Asme*. 2006;128:3.
- [85] Kofstad P. *High-temperature Oxidation of Metals*: John Wiley & Sons; 1966.
- [86] LaBrosse MR, Chen L, Johnson JK. First principles study of vacancy and tungsten diffusion in fcc cobalt. *Modeling and Simulations in Materials Science and Engineering*. 2010;18.
- [87] Laguna-Bercero MA, Sanjuán ML, Merino RI. Raman spectroscopic study of cation disorder in poly- and single crystals of the nickel aluminate spinel *Journal of Physics: Condensed Matter*. 2007;19:186217.
- [88] Lee J-B, Park C-S, Choi S-I, Song Y-W, Kim Y-H, Yang H-S. Redox Characteristics of Various Kinds of Oxygen Carriers for Hydrogen Fueled Chemical-Looping Combustion. *Journal of Industrial and Engineering Chemistry*. 2005;11:96-102.
- [89] Lei Y, Cant, N., Trimm, D. The origin of rhodium promotion of Fe₃O₄-Cr₂O₃ catalysts for the high-temperature water-gas shift reaction. *Journal of Catalysis*. 2006;239:227-36.
- [90] Leskelä M, Ritala M. Atomic layer deposition (ALD): from precursors to thin film structures. *Thin Solid Films*. 2002;409:138-46.
- [91] Li F, Kim H, Wang D, Zeng L, Chen J, Fan L. Syngas Chemical Looping Gasification Process: Oxygen Carrier Particle Selection and Performance. *Energy Fuels*. 2009;23:4182-9.
- [92] Li F, Sun Z, Luo S, Fan L-S. Ionic diffusion in the oxidation of iron-effect of support and its implications to chemical looping applications. *Energy & Environmental Science*. 2011;4:876-80.
- [93] Li F, Zeng L, Velazquez-Vargas L, Yoscovitis Z, Fan L. Syngas Chemical Looping Gasification Process: Bench-scale Studies and Reactor Simulations. *AIChE J*. 2010;56:2186-99.
- [94] Li Z, Little R, Dervishi E, Saini V, Xu Y, Biris AR, et al. Micro-Raman spectroscopy analysis of catalyst morphology for carbon nanotubes synthesis. *Chemical Physics*. 2008;353:25-31.
- [95] Liao YY, Li YW, Hu XG, Chu JH. Temperature dependent phonon Raman scattering of highly a-axis oriented CoFe₂O₄ inverse spinel ferromagnetic films grown by pulsed laser deposition *Applied Physics Letters*. 2012;100:071905.
- [96] Lien HO, El-Mehairy AE, Ross HU. A Two-zone Theory of Iron-oxide Reduction. *Journal of the Iron and Steel Institute*. 1971:541-5.
- [97] Lorente E, Pena JA, Herguido J. Kinetic study of the redox process for separation and storing hydrogen: Oxidation stage and ageing of solid. *Int J Hydrogen Energy*. 2008;33:615-26.

- [98] Loutzenhiser P, Galvez, M., et al. CO₂ Splitting via Two-Step Solar Thermochemical Cycles with Zn/ZnO and FeO/Fe₃O₄ Redox Reactions II: Kinetic Analysis. *Energy and Fuels*. 2009;23:2832-9.
- [99] Loutzenhiser PG, Gálvez ME, Hischier I, Stamatiou A, Frei A, Steinfeld A. CO₂ Splitting via Two-Step Solar Thermochemical Cycles with Zn/ZnO and FeO/Fe₃O₄ Redox Reactions II: Kinetic Analysis. *Energy & Fuels*. 2009;23:2832-9.
- [100] Lu F, Tinkler, S., Dieckmann, R. Point defects and cation tracer diffusion in (Co_xFe_{1-x})₃-dO₄ spinels. *Solid State Ionics*. 1993;62:39-52.
- [101] Lu F-H, Tinkler S, Dieckmann R. Point defects and cation tracer diffusion in (Co_xFe_{1-x})₃-dO₄ spinels. *Solid State Ionics*. 1993;62:39-52.
- [102] Lyngfelt A, Johansson M, Mattisson T. Chemical Looping Combustion - Status of Development. 9th International Conference on Circulating Fluidized Beds. Hamburg, Germany 2008.
- [103] Mattisson T, Jardnas A, Lyngfelt A. Reactivity of Some Metal Oxides Supported on Alumina with Alternating Methane and Oxygens Application for Chemical-Looping Combustion. *Energy Fuels*. 2003; 17:643-51.
- [104] Mattisson T, García-Labiano F, Kronberger B, Lyngfelt A, Adánez J, Hofbauer H. Chemical-looping combustion using syngas as fuel. *International Journal of Greenhouse Gas Control*. 2007;1:158-69.
- [105] Mattisson T, Johansson M, Lyngfelt A. Multicycle Reduction and Oxidation of Different Types of Iron Oxide Particles - Application to Chemical-Looping Combustion. *Energy & Fuels*. 2004;18.
- [106] Mendeleev MI, Mishin Y. Molecular dynamics study of self-diffusion in bcc Fe. *Physical Review B*. 2009;80:144111.
- [107] Menzies I, Lubkiewicz, J. Oxidation of an Fe-12% Ni Alloy in Oxygen at 700C-1000C. *Oxidation of Metals*. 1971;3:41-58.
- [108] Menzies I, Lubkiewicz J. Oxidation of an Fe-12% Ni Alloy in Oxygen at 700C-1000C. *Oxid Met*. 1971;3:41-58.
- [109] Mizuno T, Asato M, Hoshino T, Kawakami K. First-principles calculations for vacancy formation energies in Ni and Fe: non-local effect beyond the LSDA and magnetism. *Journal of Magnetism and Magnetic Materials*. 2001;226–230, Part 1:386-7.
- [110] Moran M, Shapiro H. *Fundamentals of Engineering Thermodynamics - 5th Edition*: John Wiley & Sons; 2004.

- [111] Moran VJ, Jenkins AE. The influence of three foreign cations on the reduction of magnetite. *Journal of the Iron and Steel Institute*. 1961;199:26-33.
- [112] Muller C, Bohn C, Song Q, Scott S, Dennis J. The production of separate streams of pure hydrogen and carbon dioxide from coal via an iron-oxide redox cycle. *Chem Eng J* 2011;166:1052-60.
- [113] Nkosi SS, Yalisi B, Motaung DE, Keartland J, Sideras-Haddad E, Forbes A, et al. Antiferromagnetic-paramagnetic state transition of NiO synthesized by pulsed laser deposition. *Applied Surface Science*. 2013;265:860-4.
- [114] O'Neil HSC, Navrotsky A. Simple Spinel: crystallographic parameters, cation radii, lattice energies, and cation distribution. *American Mineralogist*. 1983;68:181-94.
- [115] O'Shea VADIP, Moreira IdPR, Roldan A, Illas F. Electronic and magnetic structure of bulk cobalt: The alpha, beta, and epsilon-phases from density functional theory calculations. *The Journal of Chemical Physics*. 2010;133:024701.
- [116] Padro CEG, Putsche V. Survey of the Economics of Hydrogen Technologies. NREL/TP-570-27079. Golden, CO: National Renewable Energy Laboratory; 1999.
- [117] Perron H, Mellier T, Domain C, Roques J, Simoni E, Drot R, et al. Structural investigation and electronic properties of the nickel ferrite NiFe₂O₄: a periodic density functional theory approach. *Journal of Physics: Condensed Matter*. 2007;19.
- [118] Peterson NL, Chen WK, Wolk D. Correlation and Isotope Effects for Cation Diffusion in Magnetite. *J Phys Chem Solids*. 1980;41:709-19.
- [119] Pineau A, Kanari, N., Gaballah, I. Kinetics of reduction of iron oxides by H₂ Part II: Low temperature reduction of magnetite. *Thermochimica Acta* 2007;456:75-88.
- [120] Roiter BD, Paladino AE. Phase Equilibria in the Ferrite Region of the System Fe-Co-O. *Journal of the American Ceramic Society*. 1962;45:128-33.
- [121] Ryu J-C, Lee D-H, Kang K-S, Park C-S, Kim J-W, Kim Y-H. Effect of additives on redox behavior of iron oxide for chemical hydrogen storage. *Journal of Industrial and Engineering Chemistry*. 2008;14:252-60.
- [122] Sastri MVC, Viswanath RP, Viswanathan B. Studies on the reduction of iron oxide with hydrogen. *International Journal of Hydrogen Energy*. 1982;7:951-5.
- [123] Scheffe J, Li J, Weimer A. A spinel/hercynite water-splitting redox cycle. *Int J Hydrogen Energy*. 2010;35:3333-40.

- [124] Scheffe JR, Allendorf MD, Coker EN, Jacobs BW, McDaniel AH, Weimer AW. Hydrogen Production via Chemical Looping Redox Cycles Using Atomic Layer Deposition-Synthesized Iron Oxide and Cobalt Ferrites. *Chem Mater* 2011;23:2030-8.
- [125] Scheffe JR, Francés A, King DM, Liang X, Branch BA, Cavanagh AS, et al. Atomic layer deposition of iron (III) oxide on zirconia nanoparticles in a fluidized bed reactor using ferrocene and oxygen. *Thin Solid Films*. 2009;517:1874-9.
- [126] Scheffe JR, McDaniel AH, Allendorf MD, Weimer AW. Kinetics and mechanism of solar-thermochemical H₂ production by oxidation of a cobalt ferrite–zirconia composite. *Energy & Environmental Science*. 2013.
- [127] Shebanova ON, Lazor P. Raman spectroscopic study of magnetite (FeFe₂O₄): a new assignment for the vibrational spectrum. *Journal of Solid State Chemistry*. 2003;174:424-30.
- [128] Shoko E, McLellan B, Dicks AL, Diniz da Costa JC. Hydrogen from coal: Production and utilisation technologies. *International Journal of Coal Geology*. 2006;65:213-22.
- [129] Sholl D. Using density functional theory to study hydrogen diffusion in metals: A brief overview. *Journal of Alloys and Compounds*. 2007:462-8.
- [130] Sholl DS, Steckel JA. *Density Functional Theory: A practical Introduction*. Hoboken: John Wiley & Sons, Inc.; 2009.
- [131] Sickafus KE, Wills JM, Grimes NW. Structure of Spinel. *Journal of the American Ceramic Society*. 1999;82:3279-92.
- [132] Sircar S, Golden TC. Purification of Hydrogen by Pressure Swing Adsorption. 2000;35:667-87.
- [133] Sircar S, Golden TC. Purification of Hydrogen by Pressure Swing Adsorption. *Separation Science and Technology*. 2006;35:667-87.
- [134] Sloczynski J, Ziolkowski J, Grzybowska B, Grabowski R, Jachewicz D, Wcislo K, et al. Oxidative Dehydrogenation of Propane on Ni_xMg_{1-x}Al₂O₄ and NiCr₂O₄ Spinel. *Journal of Catalysis*. 1999;187:410-8.
- [135] Smith B, Loganathan M, Shantha M. A Review of the Water Gas Shift Reaction Kinetics. *Int J Chem React Eng*. 2010;8.
- [136] Smith RJ, Loganathan M, Shantha MS. A Review of the Water Gas Shift Reaction Kinetics. *International Journal of Chemical Reactor Engineering*. 2010;8:R4.
- [137] Solunke R, Veser G. Hydrogen Production via Chemical Looping Steam Reforming in a Periodically Operated Fixed-Bed Reactor. *Ind Eng Chem Res*. 2010;49:11037-44.

- [138] Spycher N, Reed M. Fugacity coefficients of H₂, CO₂, CH₄, H₂O and of H₂O- CO₂-CH₄ mixtures: A virial equation treatment for moderate pressures and temperatures applicable to calculations of hydrothermal boiling. *Geochim Cosmochim Acta*. 1988;52:739-49.
- [139] Stark JP. *Solid State Diffusion*: John Wiley & Sons, Inc. ; 1976.
- [140] Stefanic G, Music S, Popovic S, Nomurac K. A study of the ZrO₂-Fe₂O₃ system by XRD, ⁵⁷Fe Mossbauer and vibrational spectroscopies. *Journal of Molecular Structure*. 1999;480-481:627-31.
- [141] Stehle RC, Bobek MM, Hooper R, Hahn DW. Oxidation reaction kinetics for the steam-iron process in support of hydrogen production. *Int J Hydrogen Energy*. 2011;36:15125-35.
- [142] Stiegel GJ, Ramezan M. Hydrogen from coal gasification: An economical pathway to a sustainable energy future. *International Journal of Coal Geology*. 2006;65:173-90.
- [143] Sundar S, Deevi S. Isothermal oxidation behavior of FeCo-2V intermetallic alloy. *Intermetallics*. 2004;12:1311-6.
- [144] Svoboda K, Siewiorek A, Baxter D, Rogut J, Pohorely M. Thermodynamic possibilities and constraints for pure hydrogen production by a nickel and cobalt-based chemical looping process at lower temperatures. *Energy Convers Manage*. 2008;49:221-31.
- [145] Svoboda K, Slowinski G, Rogut J, Baxter D. Thermodynamic possibilities and constraints for pure hydrogen production by iron based chemical looping process at lower temperatures. *Energy Convers Manage*. 2007;48:3063-73.
- [146] Tamaura Y, Stienfeld A, Kuhn P, Ehrensberger K. PRODUCTION OF SOLAR HYDROGEN BY A NOVEL, 2-STEP, WATER-SPLITTING THERMOCHEMICAL CYCLE. *Energy*. 1995;20:325.
- [147] Thang PD, Rijnders G, Blank DHA. Spinel cobalt ferrite by complexometric synthesis. *Journal of Magnetism and Magnetic Materials*. 2005;295:251-6.
- [148] Thang PD, Rijnders G, Blank DHA. Stress-induced magnetic anisotropy of CoFe₂O₄ thin films using pulsed laser deposition. *J Magn Magn Mater*. 2007;310:2621-3.
- [149] Tihay F, Pourroy G, Richard-Plouet M, Roger AC, Kiennemann A. Effect of Fischer-Tropsch synthesis on the microstructure of Fe-Co-based metal/spinel composite materials. *Applied Catalysis A: General*. 2001;206:29-42.
- [150] Tiwari S, Prakash R, Choudhary R, Phase D. Oriented growth of Fe₃O₄ thin film on crystalline and amorphous substrates by pulsed laser deposition. *J Phys D: Appl Phys*. 2007;40:4943-7.

- [151] Tucker JD, Najafabadi, R., Allen, T.R., Morgan, D. Ab Initio-based diffusion theory and tracer diffusion in Ni-Cr and Ni-Fe alloys. *Journal of Nuclear Materials*. 2010;405:216-34.
- [152] Tucker JD, Najafabadi R, Allen TR, Morgan D. Ab initio-based diffusion theory and tracer diffusion in Ni-Cr and Ni-Fe alloys. *Journal of Nuclear Materials*. 2010;405:216-34.
- [153] Turkdogan ET, McKewan WM, Zwell L. Rate of Oxidation of Iron to Wustite in Water-Hydrogen Gas Mixtures. *The Journal of Physical Chemistry*. 1965;69:327-34.
- [154] Unmuth EE, Schwartz LH, Butt JB. Iron Alloy Fischer-Tropsch Catalysts I. Oxidation-Reduction Studies of the Fe-Ni System. *Journal of Catalysis*. 1980;61:242-55.
- [155] Visser Ed, Hendriks C, Barrio M, Mølnvik MJ, Koeijer Gd, Liljemark S, et al. Dynamic CO₂ quality recommendations. *Greenhouse Gas Control*. 2008;2:478-84.
- [156] Wallwork G. The oxidation of alloys. *Rep Progr Phys*. 1976; 5.
- [157] Wang J, Ryan D, Anthony EJ, Wigston A. Effects of Impurities on Geological Storage of CO₂. IEAGHG; 2011.
- [158] William D. Callister J. *Material Science and Engineering: An Introduction - 5th Edition*: John Wiley & Sons, Inc.; 2000.
- [159] Wu P, Kershaw R, Dwight K, Wold A. PREPARATION AND CHARACTERIZATION OF Co(II)/ZrO₂ SOLID SOLUTION. *Mat Res Bull*. 198;23:475-80.
- [160] Xiang, Chen. Hydrogen and Electricity from Coal with Carbon Dioxide Separation Using Chemical Looping Reactors. *Energy & Fuels*. 2007;21:2272-7.
- [161] Xiang W, Chen S, Xue Z, Sun X. Investigation of coal gasification hydrogen and electricity co-production plant with three-reactors chemical looping process. *International Journal of Hydrogen Energy*. 2010;35:8580-91.
- [162] Yang J, Cai N, Li Z. Hydrogen Production from the Steam-Iron Process with Direct Reduction of Iron Oxide by Chemical Looping Combustion of Coal Char. *Energy Fuels*. 2008;22:2570-9.
- [163] Young D. *High Temperature Oxidation and Corrosion of Metals*. Amsterdam, The Netherlands: Elsevier; 2008.
- [164] Ziolkowski J, Dziembaj L. Empirical Relationship between Individual Cation-Oxygen Bond Length and Bond Energy in Crystals and in Molecules. *Journal of Solid State Chemistry*. 1985;57:291-9.

Appendix A: Diffusion in Metals and Spinels

A.1 Diffusion in metal and spinel lattices

Rates of solid state diffusion processes are controlled by the migration of atoms through the lattice and are dependent upon the energy it takes to move the atom, as well as the number of adjacent sites into which the atom can move. [1] Atoms may move to a neighboring unoccupied site, or vacancy, or may move to occupy an interstitial site located between normally occupied sites. A vacancy site or an atom occupying an interstitial site are called point defects and exist in pairs to preserve electrical neutrality. The combination of an anion vacancy with a cation vacancy is called a Schottky defect, and a cation interstitial paired with a cation vacancy is called a Frenkel defect. [2] Unpaired defects do occur and exist in non-stoichiometric materials. Perfect crystal lattices at 0 K contain no point defects; however, as the temperature increases atoms in the lattice gain vibrational energy and defects form. Point defects increase both the internal energy and entropy of the crystal, thus an equilibrium defect concentration exists when the free energy is minimized. [2] The equilibrium concentration of defects at a given temperature can be calculated using statistical thermodynamics with a knowledge of the energies required to form the defects.

Similarly, in a perfect crystal lattice at 0 K, atoms do not migrate. As atoms gain vibrational energy, they can translate into a defect, either forming an interstitial (called an interstitial diffusion mechanism) or hopping to a vacancy where the atom and vacancy move in opposite directions through the lattice (called a vacancy diffusion mechanism). [2] This movement requires passing through a higher energy intermediate site, where adjacent atoms are pushed from their lattice positions into higher energy states. [3] The critical point on the energy

surface during atomic migration is called the transition state, and is the highest energy state between the initial and final location of the migrating atom. [3] Enthalpy change between the material with a defect, and the material with a defect in the transition state, is called the migration barrier, or migration enthalpy (ΔH_m). In the ideal limit, the temperature dependent diffusion coefficient can be calculated from knowing both the enthalpy of vacancy formation and the enthalpy of the transition state:

$$D = D_0 \exp\left(\frac{-Q}{RT}\right) \quad \text{Eq. A.1}$$

where $Q = \Delta H_{\text{vacancy formation}} + \Delta H_m$, and D_0 is a function of the neighboring atom distance and concentration, and the frequency with which the atoms are vibrating. [2] The vibration frequency of the atoms in the lattice, which is the Debye frequency for pure metals, is the jump attempt frequency, and the probability of an atom successfully completing a jump along with the attempt frequency determine the atomic jump rate. [1]

A.2 Diffusion in Fe, Co and Ni Metals

The metals examined in this study are arranged in the face-centered cubic (FCC) or body centered cubic (BCC) structures. [4, 5] The FCC structure is the most tightly packed structure, with each atom touching its neighboring atom on all sides. [6] In metals with an FCC structure, the energy of an interstitial defect formation is much greater than the energy for a vacancy formation due to this close packing. The dominating diffusion in these materials is most often found to be through vacancies. In a BCC lattice, more space exists between atoms and the energies of vacancy formation and interstitial formation are similar.

Iron arranges into a BCC structure at temperatures below 1173 K. [4] Diffusion studies indicate that Fe self-diffusion occurs through a vacancy mediated process rather than an interstitial mechanism due to the higher concentration of vacancies in the lattice at all temperatures. [7] Cobalt and Ni exist in the FCC structure in the CLH temperature range and in accord with the defect formation energies the diffusion mechanism is vacancy mediated for each of these metals. [4]

A.3. Diffusion in Spinel

The spinel structure is a close packed FCC arrangement of oxygen anions with cations on the interstitial sites in two types of positions. The tetrahedral site is coordinated with four oxygen anions and the octahedral site is coordinated with six oxygen anions. [8] Each oxygen anion is tetrahedrally coordinated with one tetrahedral and three octahedral cations. [9] The terms “octahedral sublattice” and “tetrahedral sublattice” refer to the cations on the octahedral and tetrahedral sites, respectively. The distances between atoms in the lattice depend on the cation valency and cation ionic radius. Cations are able to migrate from tetrahedral sites to tetrahedral vacancies, from octahedral sites to octahedral vacancies, or between the two types of cation sites. [8]

Oxygen activity dependence of the rate limiting cation migration mechanism has been observed in Fe_3O_4 between the temperatures of 773 K and 1473 K in several studies. [10-12] The dominant defect at low O_2 activity is cation interstitials, while at high O_2 activities cation vacancies become dominant; however, the mechanism of cation vacancy diffusion remains ambiguous. [12] Computer simulations of the defect formation and migration energies in Fe_3O_4 identified the energies associated with vacancy formation and migration on the tetrahedral

sublattice as having higher energies and concluded that vacancy migration must take place through the octahedral sublattice. [10]

Studies of vacancy formation and migration in CoFe_2O_4 at high temperatures similarly show that cation migration through cation vacancies is the dominant diffusion mechanism at high oxygen activities, and cation migration through cation interstitials is the dominant diffusion mechanism at low oxygen activities. [13] Additionally, as the Co content of the spinel increases (as the spinel becomes less Fe-rich) at the same O_2 activity, the overall defect concentration decreases. The measured tracer diffusion decreases two orders of magnitude as the spinel composition is changed from Fe_3O_4 to CoFe_2O_4 at 1473 K.

Little information is available in the literature detailing migration barriers and vacancy formation enthalpies for spinel materials, and existing data is summarized in Table A.1. The migration enthalpies in NiFe_2O_4 are unavailable, along with vacancy formation enthalpies for CoFe_2O_4 . The values that are not readily available in the literature must be measured experimentally or calculated using ab-initio methods. Our goal is to investigate the migration barriers and vacancy formation enthalpies in Fe_3O_4 , CoFe_2O_4 , NiFe_2O_4 , and in the Fe, Co, and Ni metallic states using ab-initio methods to identify the phase in which the diffusion process is likely to limit the oxidation kinetics.

Fe ₃ O ₄	Octahedral vacancy formation (kJ/mol (eV))	Tetrahedral vacancy formation (kJ/mol (eV))	Octahedral-octahedral migration barrier (kJ/mol (eV))	Tetrahedral-tetrahedral migration barrier (kJ/mol (eV))	[14]
	126 (1.3)	238 (2.5)	126 (1.3)	85 (0.88)	
NiFe ₂ O ₄	Octahedral vacancy formation for Ni (kJ/mol (eV))	Tetrahedral vacancy formation for Fe (kJ/mol (eV))	Octahedral vacancy formation for Fe (kJ/mol (eV))		[15]
	109 (1.1)	368 (3.8)	262 (2.7)		
CoFe ₂ O ₄	Cation vacancy migration barrier (Fe) (kJ/mol (eV))	Cation vacancy migration barrier (Co) (kJ/mol (eV))			[13]
	139 (1.4)	145 (1.5)			

Table A.1: Defect migration and formation enthalpies found in the literature

A.4 Diffusion Studies by Atomistic Computer Simulations

Diffusion coefficients are difficult to accurately determine experimentally and involve precise measurement of tracer concentrations in the lattice at discrete timesteps. The measurements are expensive and difficult to complete without error. [7] An alternative method for determining diffusion coefficients is through ab-initio computer simulations which have the benefit of providing insight into the mechanism of specific diffusion and the rate limiting steps through calculations of the vacancy formation enthalpy and migration barriers. Density functional theory (DFT) is a technique used to calculate the ground state electron density of a many-body system by minimizing electron density functionals through iteratively solving the Kohn-Sham Equations. [3] Accurate ground state properties can be calculated for solid state materials using DFT, from which temperature dependent vacancy formation enthalpy and migration barriers can be calculated.

A.5 Computational Details

Vacancy formation enthalpies, lattice constants, and migration barriers in metallic and spinel systems were calculated using Periodic Boundary Condition (PBC) DFT as implemented in the Vienna *Ab initio* Simulation Program (VASP). [16, 17] DFT computations were performed using the Perdew-Burke-Ernzerhof (PBE) Generalized Gradient Approximation (GGA) exchange-correlation functional coupled with Projector Augmented Wave (PAW) pseudopotentials. [18] [19, 20] PAWs treated Fe's $4s^23d^6$ electrons, Co's $4s^23d^7$ electrons, Ni's $4s^23d^8$ electrons, and O's $2s^22p^4$ electrons explicitly with a plane wave expansion.

The calculations for metallic systems were performed with a 125(-1) atom periodic simulation supercell. After geometric relaxation, the cell volume was fixed while relaxations were allowed within the cell. An examination of the effect of cut off energies on the metallic cells found less than a 0.001 eV/atom difference in total cell energy for plane wave expansions with 500 and 600 eV cut off energies; therefore, we utilized the less computationally expensive 500 eV cut off energy. Vacancy formation enthalpies were calculated with a 64(-1), a 125(-1) and a 216(-1) periodic supercell to ensure adequate defect spacing. [21] The vacancy formation enthalpy difference was less than 0.05 eV between the 125 atom, 6x6x6 Γ -point centered Monkhorst-Pack k point mesh calculations and the 216 atom 2x2x2 Γ -point centered Monkhorst-Pack k point mesh calculations. The less computationally expensive 125 cell and 6x6x6 kpoint mesh was used. Calculations were spin polarized to account for magnetic ordering.

The calculations for spinel systems were performed with a 140(-1) atom periodic simulation cell. Studies regarding k-point mesh and cutoff energy showed an optimized 2x2x2 Γ -point centered Monkhorst-Pack k point mesh and 500 eV cutoff energy. A DFT+U correction term

was used for each transition metal in the spinel calculation to account for non-cancelling overbinding errors, and the calculations were spin polarized to account for magnetic ordering. (Citation here)

The Nudged Elastic Band (NEB) method was utilized to calculate migration barriers for the diffusion of a single cation atom through each type of cell and calculations were converged to forces under at least 0.03 eV/Å unless otherwise noted. [22] Vacancy formation energies were calculated from

$$E_f(\text{defect}) = E_c(\text{defect}) + E_{\text{atom}} - E_c(\text{no defect}) \quad \text{Eq. A.2}$$

where $E_f(\text{defect})$ is the defect formation energy, $E_c(\text{no defect})$ is the total energy of the complete cell, $E_c(\text{defect})$ is the total energy of the cell with a defect, and E_{atom} is the cohesive energy per atom.

A.6. Calculation Results

Based on literature reports indicating that the vacancy mechanism dominates diffusion in BCC and FCC metals, only the vacancy migration was investigated for the metals. [1, 7, 23] The process under investigation is oxidation, which takes place under high oxygen activity conditions; therefore, only the cation vacancy diffusion mechanism is considered in the spinel material. Calculations were performed in this dilute limit, such that only one defect and one foreign atom are introduced into the lattice. Due to the small size of DFT calculations, and the periodic boundary conditions, this minimizes the interaction between vacancies and tracer atoms. [3]

Results from the calculations with metallic supercells are shown in Table A.3, along with values from literature. Calculated values are in accord with the accepted literature values.

Ni (FCC)	This Study	Literature	
Lattice parameter (Å)	3.52	3.52	[24]
H_{vf} (kJ/mol(eV))	137 (1.63)	150-157 (1.55-1.63)	[25]
Co (FCC)			
Lattice parameter (Å)	3.52	3.42-3.55	[5]
H_{vf} (kJ/mol(eV))	175 (1.81)	178- 184 (1.84-1.91)	[5, 26]
Fe (BCC)			
Lattice parameter (Å)	2.83	2.83-2.87	[27]
H_{vf} (kJ/mol(eV))	211 (2.18)	208-236 (2.15-2.44)	[27]

Table A.2: Lattice structures and vacancy formation in metals

The self-migration enthalpies and tracer atom migration enthalpies calculated using the NEB method are shown in Table A.3.

	This Study	Literature	
ΔH_{mig} (Fe bulk) kJ/mole (eV)			
Fe in Fe	-	57.9 (0.60)	[7]
Co in Fe	68.4 (0.71)		
Ni in Fe	58.7 (0.61)	65.6 (0.68)	(?)
ΔH_{mig} (Co bulk) kJ/mol (eV)			
Co in Co	98.7 (1.02)		
Fe in Co	68.4 (0.71)		
ΔH_{mig} (Ni bulk) kJ/mol (eV)			
Ni in Ni	-	100.4 (1.1)	[28]
Fe in Ni	90.9 (0.94)	93.6 (0.97)	[28]

Table A.3: Migration enthalpies in metals calculated in this study and from literature

Due to a lack of proper convergence, the values for Fe self-migration and for Ni self migration were not determined. Values from literature correlate well with the calculated values in this study.

As shown with previous spinel studies, the values calculated for octahedral vacancy formation enthalpy in the spinels were at least 50 kJ/mole (0.5 eV) less than those calculated for tetrahedral vacancy formation, making tetrahedral - to - tetrahedral and octahedral - to - tetrahedral site jumps unlikely pathways for cation migration. [13-15] In this study, only octahedral – to - octahedral site migration barriers were investigated. Calculated migration barriers are shown in Table A.4. The Fe through CoFe_2O_4 migration barrier was not reported due to lack of proper convergence.

		Migrating atom		
		Fe	Co	Ni
Bulk	ΔH_{mig}(kJ/mol (eV))			
	Fe_3O_4	68.3 (0.71)	74.1 (0.77)	121 (1.25)
	CoFe_2O_4	-	82.4 (82.4)	
	NiFe_2O_4	95.8 (0.99)		193 (2.0)

Table A.4: Migration barriers for octahedral-octahedral migration in Fe_3O_4 , CoFe_2O_4 and NiFe_2O_4 .

The lowest barrier in the spinels is for Fe migration through Fe_3O_4 . A previous study calculated this barrier to be 125.5 kJ/mol (1.3 eV), but the calculations for migration barrier were conducted using fixed points in a direct line between octahedral sites, a method that often overestimates the migration barrier because it does not account for perpendicular motion of the atom to reach the transition state. [14] For all mixed metal oxide systems, the migration barrier

is greater through the spinel phase than through the metallic phase. The most important diffusion processes in the metallic material are migration of Fe through Ni and migration of Fe through Co, as these could inhibit the migration of Fe to the alloy/Fe₃O₄ interface. In both cases, these values are smaller than the migration barriers for each cation in the spinel. This investigation identifies diffusion in the spinel as the likely limiting mechanism during oxidation of CoFe₂O₄ and NiFe₂O₄.

A.7 References

- [1] Stark JP. Solid State Diffusion: John Wley & Sons, Inc. ; 1976.
- [2] Kofstad P. High-temperature Oxidation of Metals: John Wiley & Sons; 1966.
- [3] Sholl DS, Steckel JA. Density Functional Theory: A practical Introduction. Hoboken: John Wiley & Sons, Inc.; 2009.
- [4] Tucker JD, Najafabadi R, Allen TR, Morgan D. Ab initio-based diffusion theory and tracer diffusion in Ni-Cr and Ni-Fe alloys. Journal of Nuclear Materials. 2010;405:216-34.
- [5] O'Shea VADIP, Moreira IdPR, Roldan A, Illas F. Electronic and magnetic structure of bulk cobalt: The alpha, beta, and epsilon-phases from density functional theory calculations. The Journal of Chemical Physics. 2010;133:024701.
- [6] William D. Callister J. Material Science and Engineering: An Introduction - 5th Edition: John Wiley & Sons, Inc.; 2000.
- [7] Mendeleev MI, Mishin Y. Molecular dynamics study of self-diffusion in bcc Fe. Physical Review B. 2009;80:144111.
- [8] Sickafus KE, Wills JM, Grimes NW. Structure of Spinel. Journal of the American Ceramic Society. 1999;82:3279-92.
- [9] O'Neil HSC, Navrotsky A. Simple Spinels: crystallographic parameters, cation radii, lattice energies, and cation distribution. American Mineralogist. 1983;68:181-94.

- [10] G.V.Lewis, Catlow CRA, Corma AN. Defect Structure and Migration in Fe_3O_4 . *J PhysChem Solids* 1985;46:1227-33.
- [11] Atkinson A, O'Dwyer ML, Taylor RI. ^{55}Fe diffusion in magnetite crystals at 500C and its relevance to oxidation of iron. *Journal of Materials Science*. 1983;18:2371-9.
- [12] Peterson NL, Chen WK, Wolk D. Correlation and Isotope Effects for Cation Diffusion in Magnetite. *J Phys Chem Solids*. 1980;41:709-19.
- [13] Lu F-H, Tinkler S, Dieckmann R. Point defects and cation tracer diffusion in $(\text{Co}_x\text{Fe}_{1-x})_{3-d}\text{O}_4$ spinels. *Solid State Ionics*. 1993;62:39-52.
- [14] Hendy S, Walker B, Laycock N, Ryan M. Ab initio studies of the passive film formed on iron. *Physical Review B*. 2003;67:085407.
- [15] Perron H, Mellier T, Domain C, Roques J, Simoni E, Drot R, et al. Structural investigation and electronic properties of the nickel ferrite NiFe_2O_4 : a periodic density functional theory approach. *Journal of Physics: Condensed Matter*. 2007;19.
- [16] Kresse G, Furthmüller J. Efficient iterative schemes for ab initio total-energy calculations using a plane-wave basis set. *Phys Rev B*. 1996;54:11169.
- [17] Kresse G, Furthmüller J. Efficiency of ab-initio total energy calculations for metals and semiconductors using a plane-wave basis set. *Computational Materials Science*. 1996;6:15-50.
- [18] Perdew JP, Burke K, Ernzerhof M. Generalized Gradient Approximation Made Simple. *Phys Rev Lett*. 1996;77:3865.
- [19] Blöchl PE. Projector augmented-wave method. *Phys Rev B*. 1994;50:17953.
- [20] Kresse G, Joubert D. From ultrasoft pseudopotentials to the projector augmented-wave method. *Phys Rev B*. 1999;59:1758-75.
- [21] Castleton CWM, Höglund A, Mirbt S. Density functional theory calculations of defect energies using supercells. *Modelling and Simulation in Materials Science and Engineering*. 2009;17.

- [22] Mills G, Jónsson H, Schenter GK. Reversible work transition state theory: application to dissociative adsorption of hydrogen. *Surf Sci.* 1995;324:305-37.
- [23] Young D. *High Temperature Oxidation and Corrosion of Metals*. Amsterdam, The Netherlands: Elsevier; 2008.
- [24] Jarlborg T, Freeman AJ. Self-consistent semi-relativistic energy band structure of fcc and tetragonal Ni metal. *Journal of Magnetism and Magnetic Materials.* 1980;22:6-14.
- [25] Asato M, Hoshino T, Asada T, Zeller R, Dederichs PH. Vacancy formation energies in FCC metals: non-local effect beyond the LSDA. *Journal of Magnetism and Magnetic Materials.* 1998;177–181, Part 2:1403-4.
- [26] Drittler B, Weinert M, Zeller R, Dederichs PH. Vacancy formation energies of fcc transition metals calculated by a full potential green's function method. *Solid State Communications.* 1991;79:31-5.
- [27] Mizuno T, Asato M, Hoshino T, Kawakami K. First-principles calculations for vacancy formation energies in Ni and Fe: non-local effect beyond the LSDA and magnetism. *Journal of Magnetism and Magnetic Materials.* 2001;226–230, Part 1:386-7.
- [28] Tucker JD, Najafabadi, R., Allen, T.R., Morgan, D. Ab Initio-based diffusion theory and tracer diffusion in Ni-Cr and Ni-Fe alloys. *Journal of Nuclear Materials.* 2010;405:216-34.